PLASTIC LIMIT ANALYSIS OF OFFSHORE FOUNDATION AND ANCHOR

A Dissertation

by

CHAO-MING CHI

Submitted to the Office of Graduate Studies of
Texas A&M University
in partial fulfillment of the requirements for the degree of

DOCTOR OF PHILOSOPHY

August 2010

Major Subject: Civil Engineering

PLASTIC LIMIT ANALYSIS OF OFFSHORE FOUNDATION AND ANCHOR

A Dissertation

by

CHAO-MING CHI

Submitted to the Office of Graduate Studies of
Texas A&M University
in partial fulfillment of the requirements for the degree of

DOCTOR OF PHILOSOPHY

Approved by:

Chair of Committee,	Charles P. Aubeny
Committee Members,	Jose M. Roesset
	James D. Murff
	Jun Zhang
	Jerome J. Schubert
Head of Department,	John Niedzwecki

August 2010

Major Subject: Civil Engineering

ABSTRACT

Plastic Limit Analysis of Offshore Foundation and Anchor. (August 2010)

Chao-Ming Chi, B.S., Feng Chia University, Taiwan;

M.S., National Cheng Kung University, Taiwan

Chair of Committee: Dr. Charles Aubeny

This study presents the applications of plastic limit analysis to offshore foundations and anchors, including the drag embedment anchors (DEAs) for mobile offshore drilling units (MODU's) and spudcan foundations for jack-up platforms. In deep waters, drag embedment anchors are an attractive option for mooring of semisubmersible platforms due to low installation cost and high holding capacity; on the other hand, jack-up platforms are more stable than semisubmersible platforms but only can be placed in shallow waters.

The analyses of anchor capacities are developed for an idealized anchor comprising a rectangular fluke, a cylindrical shank, and a metal chain connected to the shank at the padeye. The anchor trajectory prediction during drag embedment is also developed by considering anchor behavior in conjunction with the mechanics of the anchor line. The results of simulations show that anchors approach at equilibrium condition rapidly during the embedment and both the normalized holding capacity and the anchor line uplift angle remain constants in this stage. Besides the geometry of the fluke, the

properties of the shank and soil are also crucial factors in the anchor-soil interaction behavior.

Partial failure of mooring systems for floating structures will subject drag anchors to loads having an appreciable component outside of the intended plane of loading. Partial failure of mooring systems during hurricanes in recent years have generated an interest in understanding drag anchor performance under these conditions. The analysis presents the simulations of three dimensional trajectories of an anchor system subjected to an out-of-plane load component. For the conditions simulated in the example analyses, the anchor experienced a modest amount of continued embedment following partial failure of the mooring system; however, the ultimate embedment and capacity of the anchor is much less than what would have developed if the anchor had continued in its original trajectory within the plane of intended loading.

The analyses of the spudcan foundation of jack-up units include preloading, bearing capacity, and the displacement assessment. When the contribution of the soil moment resistance is considered, a three-stage assessment procedure is recommended: superposing environmental forces on the plot of yield surface, determining the value of yield function corresponding to the external forces, and computing the factor of safety of the spudcan. The results of the assessment may be ambiguous while the different yield functions are employed to analyze the spudcan in soft clay.

ACKNOWLEDGEMENTS

I would first like to thank my committee chair, Dr. Charles Aubeny, for his direction and support throughout the course of this research. Dr. Aubeny has been a great advisor and mentor, providing me with valuable opportunities to broaden my knowledge and further myself in the plasticity theory and offshore foundations field. In academic research, I learned the way to approach and solve problems under his instruction; in philosophy of life, his humility and enthusiasm show me the right way to get along with people from different cultures.

Dr. Jose Roesset, my academic grandfather, is another important person during my Ph.D. career. Without his help, I may be still swamped in deriving some closed form solutions or dynamic soil-structure interaction problems. His intelligence and academic sense inspire me to absorb more knowledge and explore further research issues. In addition, he is always patient with listening to my problems and then solving them with a smile.

Appreciations and thanks are also reserved for Dr. James Murff who instructed me on the concepts of geomechanics and plasticity theory. His course offered me a good tool to investigate my research and I also enjoyed in discussing academic issues with him. My other committee members, Dr. Jerome Schubert and Dr. Jun Zhang also deserve thanks for their guidance and support. Thanks also go to my friends and officemates; they always gave me substantial help, especially from Dr. Xingnian Chen and Selcuk Dincal.

I also want to extend my gratitude to Dr. Giovanna Biscontin who enhanced my soil mechanics and soil dynamics knowledge to a higher level. Under her excellent teaching and explanations, any difficult theorem can be digested easily for everyone. Furthermore, she also shows great leadership in organizing the Geo-Institute which arranges several fantastic lectures and activities, enriching my Aggie life wonderfully.

I am also thankful to Evan Zimmerman, the manager of Delmar Systems, for providing a good opportunity to touch more issues and people in the offshore field.

Finally, big thanks to my family and persons who love and encourage me. I share my achievements with you all.

TABLE OF CONTENTS

Page

CHAPTER Page

CHAPTER Page

LIST OF FIGURES

FIGURE Page

FIGURE Page

FIGURE Page

FIGURE Page

FIGURE Page

LIST OF TABLES

CHAPTER I

INTRODUCTION

1.1 General

During the past decades, the range of exploration in offshore hydrocarbon fields was extended to deep or ultra-deep waters, the technologies of mooring systems and foundations of mobile offshore drilling units (MODUs) have great progress. “MODUs” is a generic term for several categories of floating drilling or self-contained floatable machines, from shallow-water steel jackets and jack-up units, to floating semisubmersibles and drill-ships able to operate in very deep waters. Nowadays, there are a number of such unit operating in the Gulf of Mexico, the North Sea, Newfoundland and Nova Scotia, the Campos and Santos Basins off the coasts of Brazil, west of Nigeria and Angola, and South East Asia.

The jack-up unit, as shown in Figure 1.1, is towed to the location with its legs up. The barge section then is raised above the water to create an air gap. In very soft clay deposit, mat foundation (Figure 1.2) is an appropriate option to avoid the large settlement and provide buoyancy, which may serve to increase carrying load capacity.

This dissertation follows the style and format of *Journal of Geotechnical and Geoenvironmental Engineering.*

Figure 1.1 Mobile jack-up unit (courtesy of LeTourneau Inc.)

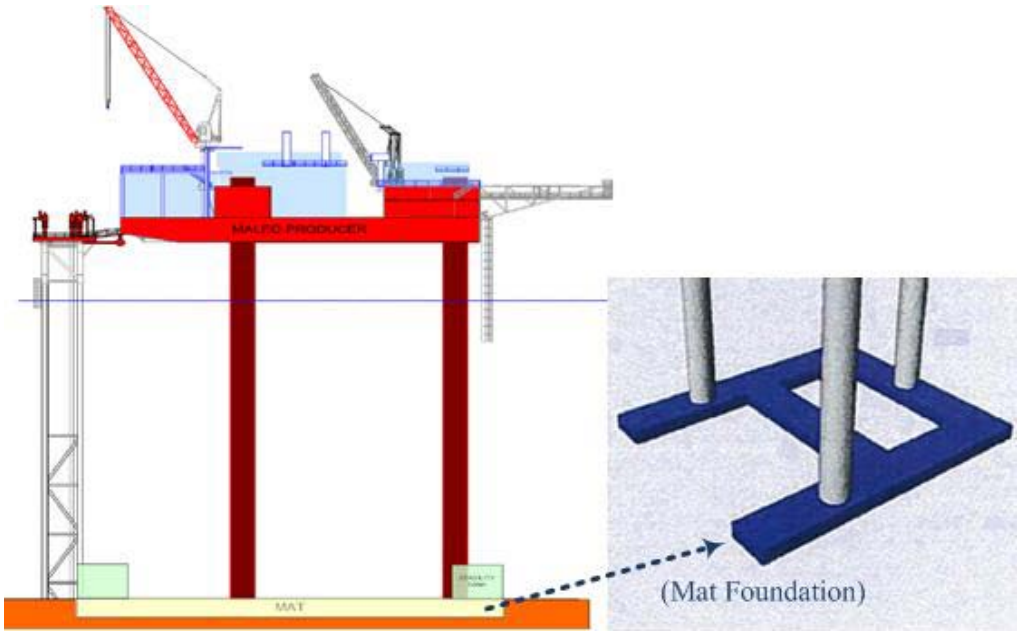

Figure 1.2 Mat supported jack-up platform (courtesy of Stewart, 2007)

Nevertheless, a mat is not suitable for uneven seabeds or those with sharp slopes because large bending moments may occur on mat or legs. An alternative foundation, spudacan footing illustrated in figure 1.3, is typically a conical structure with sloping top and bottom which helps to penetrate in stiff clay or dense sand deposit.

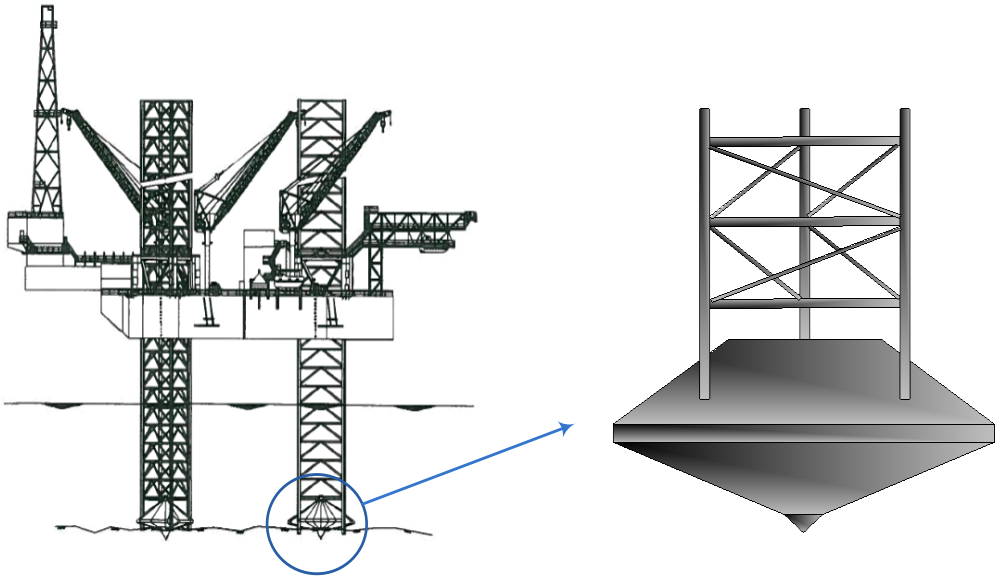

Figure 1.3 Jack-up unit (courtesy of LeTourneau Inc.) and spudcan foundation

The most dominant advantage is that it could be utilized on a very variety of seabed condition, such as on hard and soft soil, a sloping seabed, and areas existing pipelines or structures which be avoided. In addition, the installation cost is less than the mat foundation. Unlike the semisubmersible or drill-ship, it is limited to operate in shallow waters, generally less than 400 ft. In order to avoid large additional settlements due to environmental or drilling loadings, the “preloading” procedure is required prior to operation. Preloading is a process where the weight of the hull and additional ballast

water compel penetrate the foundation to further depth, a concept similar to preloading of soft clays in geotechnical engineering. After preloading, the additional ballast water is released and the jack system is used to raise the entire barge to create an “air gap” above the sea surface to prevent lateral loads from waves and currents, from acting on the barge.

Jack-up units are not feasible in deep waters. Semi-submersibles, partially submerged floating structures (Figure 1.4) moored by anchor systems, such as drag anchors, gravity anchors, or suction caissons.

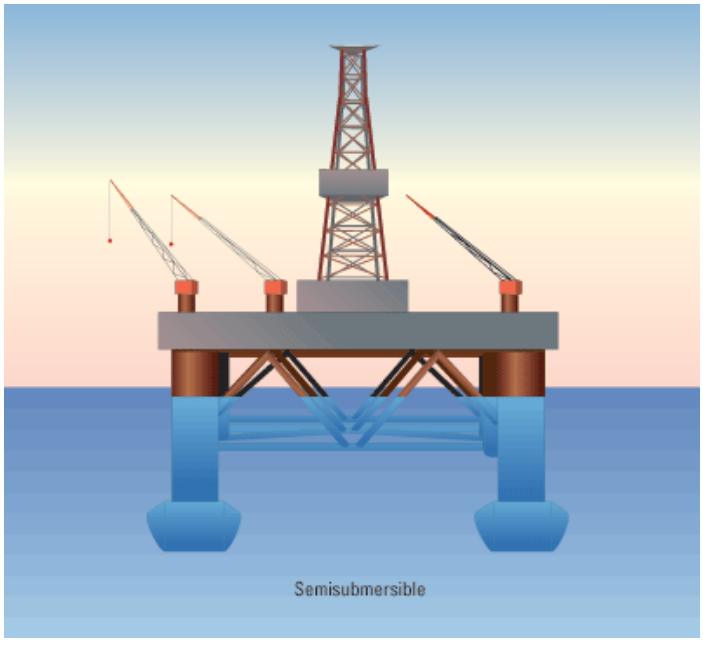

Figure 1.4 Scehmatic of semisubmersible drilling rig (courtesy of Schlumberger)

They are typically composed of large pontoons below the sea level with several columns supporting the hull at a certain distance above the sea level. The water depth

capacity ranges from 200 to thousands of feet, for example, the “Atlantis PQ” is operating in the Atlantic Oilfield of the Gulf of Mexico at a water depth of 2150 m (7050 ft). Safety vessels, offshore drilling rigs, and production platforms are major applications of semisubmersibles in offshore engineering. Drill-ships (Figure 1.5) are another type of MODU’s used for scientific drilling or natural gas or petroleum exploitation in deep or ultra-deep waters, sometimes even deeper than 10,000 feet.

Figure 1.5 Seadrill West Polaris drill-ship (courtesy of Seadrill)

In contrast to jack-up units and semisubmersibles, drill-ships can independently propel themselves from location to location without outside transport vessels. The susceptibility to being agitated by currents, waves, or winds is their drawback and it is even more troublesome while the vessel is actually drilling. Therefore, a proper mooring system is compulsory for drill-ships during the drilling. As with most of floating

platforms, the anchor systems are used for mooring to resist external loadings. In shallow waters, drill-ships are moored to seabed with six to twelve anchors, while in ultra-deep waters, dynamic positioning systems (DPS) are used to maintain station-keeping.

1.2 Concept of Anchor and Mooring Systems

1.2.1 General Description of Mooring Systems

For floating platforms in deep waters, environmental loads acting on the structures pass through the mooring system and are resisted by the anchors. Generally speaking, the mooring systems can be divided into three categories: taut leg moorings, catenary moorings and synthetic rope moorings shown in Figure 1.6.

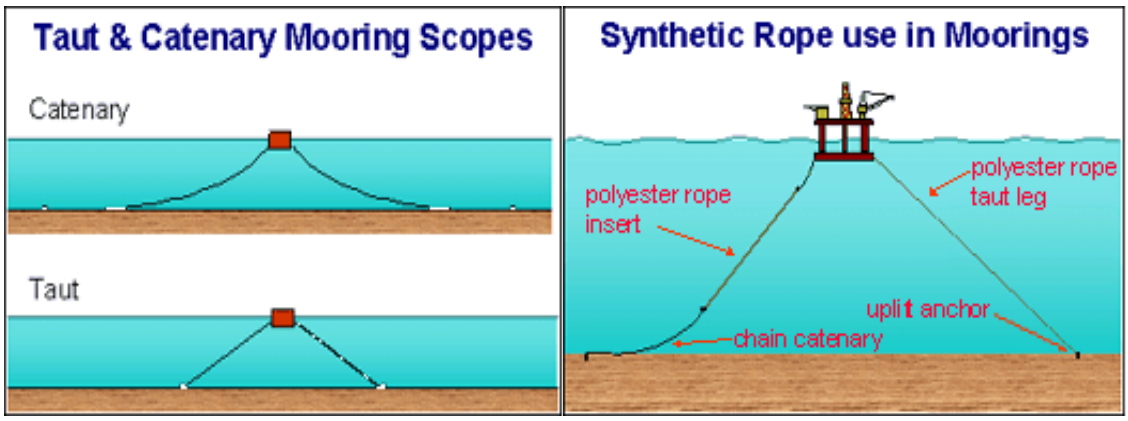

Figure 1.6 Sechmatic of three different type of mooring systems (courtesy of Tention Technology International)

The catenary mooring, consisting of relatively heavy chain and steel cable, is the most common mooring system used in shallow to deep waters. In general, there exit a notable length of mooring line resting on the seabed, and a concave curve shape in the

waters (Aubeny and Chi, 2010a) and inverse catenary curve shape in the soils (Neubecker and Randolph, 1995). With increasing water depth, the required length of chain increases, as does the weight. Therefore, the weight of chain could constrain the design of floating platforms in deep to ultra-deep waters (Ruinen, 2000). The seabed area, from Figure 1.6, encompassed by taut leg moorings is obviously less than that by the catenary moorings, with a typical taut mooring leg usually inclined at an angle of 30 to 45 degrees from horizontal. In contrast to catenary mooring line, taut mooring derives its compliance from elastic strength of the line and it is better in load sharing between adjacent lines, improving the overall efficiency of the line system. In addition, the taut mooring also overcomes the limitation of catenary mooring system in ultra-deep water by having shorter lines and offering a more compact seabed footprint. It is also less likely to interfere with neighboring mooring lines or subsea facilities (Ruinen and Degenkamp, 1999).

Synthetic rope offers another option for mooring system in deep to ultra-deep waters by using very low weight material in water. There are a large number of synthetic fiber materials used in ropes, such as nylon, polyester, aramid, or High Modulus Polyethylene. In practice, the synthetic ropes may be inserted as part of mooring line to connect with catenaries or wires. Among these several materials, polyester is the currently favored one because of its cost and fatigue endurance. Moreover, polyester rope is also suitable for taut mooring of vessel because of its elastic properties.

1.2.2 General Description of Drag Anchors

The mooring systems are the media for transmitting the environmental forces applied on the platform to the anchors. The number, type, and arrangement of them are the main factors affecting the survival of MODU's. In the past few decades, gravity anchors, suction caissons, anchor piles, drag anchors, and suction plate embedded anchors (SEPLA) have been used for anchorage. Gravity anchors provide anchorage from self-weight, which tends to be very inefficient relative to other anchors that rely on soil shearing resistance. Suction caissons provide substantial pullout capacities in soft clay (Andersen et.al, 2005) but they are technically difficult and expensive to install in deep water. The drag anchor is an attractive option because of several advantages: cost-effectiveness, high holding capacity, and its feasibility in deep water. However, they are not typically allowable for permanent platforms due to the uncertainties in predicted holding capacity and embedment position. To reduce the uncertainty, suction embedded plate anchors (SEPLAs) were developed based on a combination of the merits of suction caissons and plate anchors (Dove et al., 1998). SEPLA installation, as shown in Figure 1.7, entails the use of a suction caisson to penetrate the plate anchor to the design depth. The caisson is then retrieved, leaving the plate anchor in place. Although suction embedded plate anchors permit accurate positioning of the anchor, they are typically less cost-effective than drag anchors, especially for temporary mooring systems. Nowadays, the appearance and geometries of drag anchors vary greatly and are quite sophisticated compared with conventional ship anchors. In enhancing higher holding capacity for a mooring system, achieving a greater penetration depth is a key consideration. Anchor

types embedded by drag installation include drag embedded anchors (DEA's) and vertically loaded anchors (VLA's).

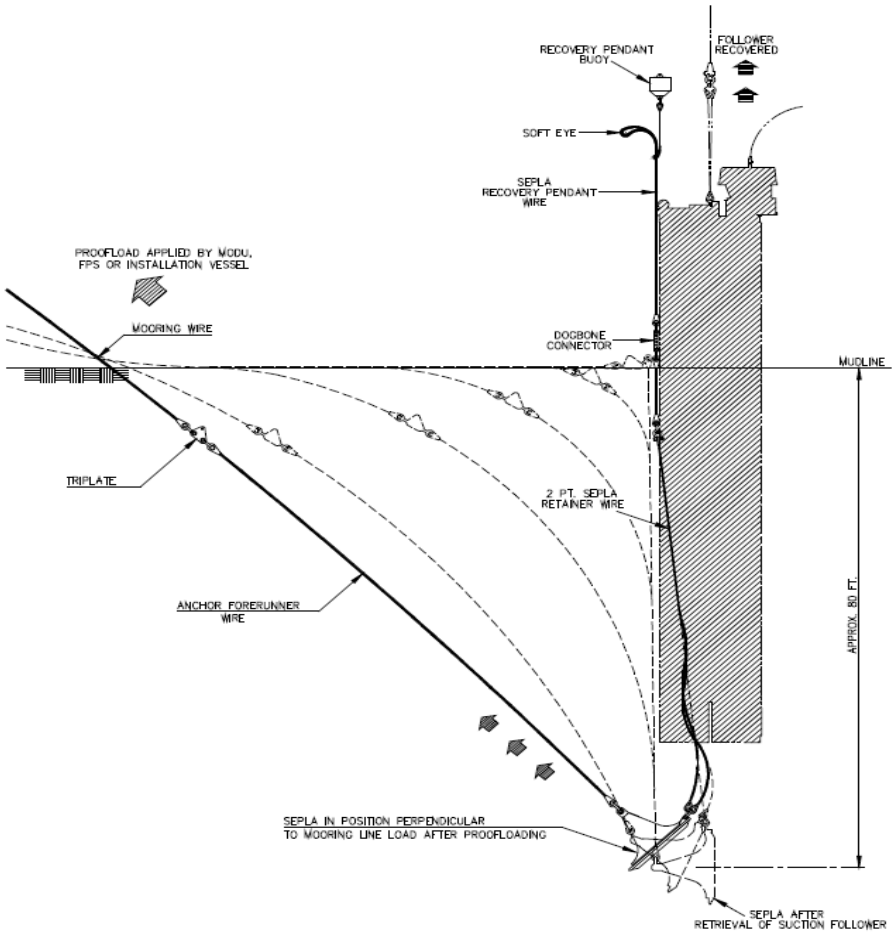

Figure 1.7 Sechmatic of installation of SEPLA (Dove et al., 1998)

1.2.2.1 Drag Embedment Anchors (DEA's)

Generally, a drag embedded anchor is composed of a wide fluke and thick shank connected with a mooring line at the shackle. To facilitate penetration, the geometry of

the fluke is not usually rectangular plate but a plate with two symmetric sharp triangular wedges in the direction of penetration (Fig 1.8).

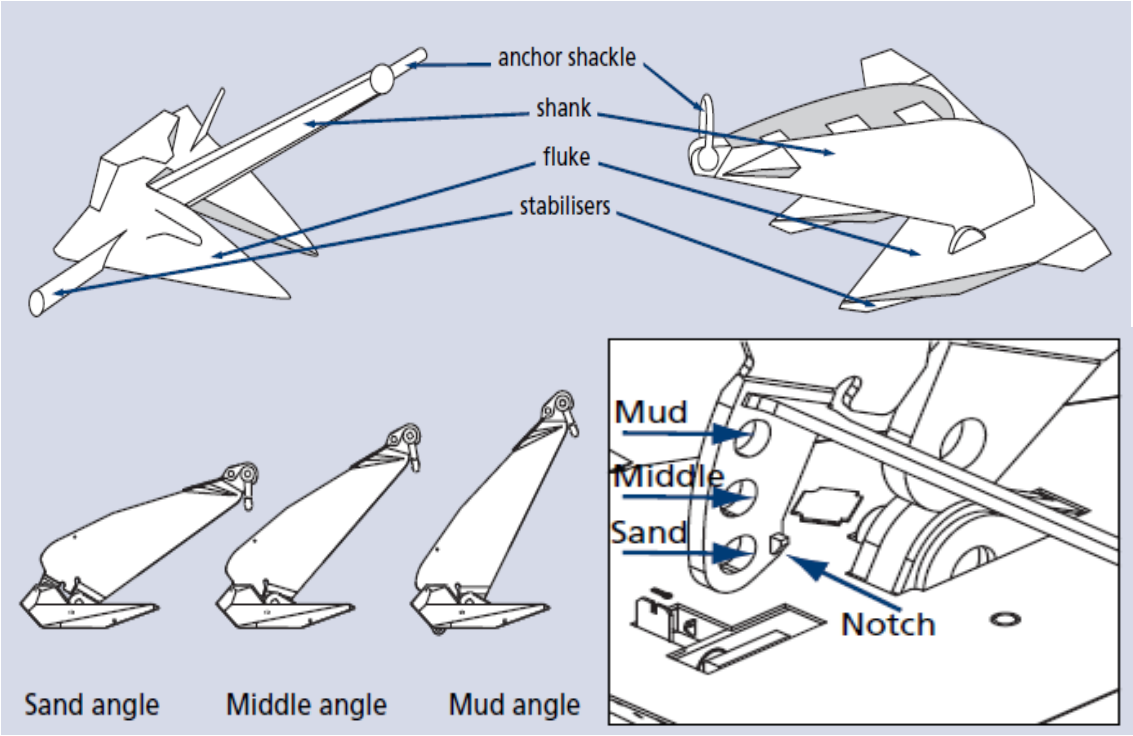

Figure 1.8 Sechmatic of Vryhof drag embedded anchor (Vryhof Anchor Manual, 2010)

Drag embedded anchors are usually employed as temporary anchorage with catenary mooring system in deepwater. Basically, DEA's are not designed for resisting a large vertical load component; therefore, they are not typically suitable for a taut leg mooring system. One distinct feature of DEA's is that the angle between the fluke and shank is fixed during the installation. However, there are different fluke-shank angle settings for different soil conditions. As shown in Figure 1.8, the larger angle is used for DEA's installation in soft mud or clay, while smaller angle are used in sands. The suggested

fluke-shank angle for mud or cohesive soil is about 50 degrees and 30 degrees for sand (Bruce FFTS MK4 anchors). Both the notch and pins serve for adjust the angle in the apparatus.

1.2.2.2 Vertically Loaded Anchors (VLA's)

In order to subjecting large vertical component loads in taut leg mooring systems, vertically loaded anchors are developed to mobilize the maximum bearing capacity of a plate anchor. Unlike drag embedded anchors, the fluke-shank angles of VLA's are opened after initial installation such that the anchor line becomes almost perpendicular with the fluke. Figure 1.9 demonstrates the two common used VLA's: Bruce Dennla anchors and Vryhof Stevmanta anchors. It is obvious that the shape of the shank is another difference between VLA's and DEA's. The shank of Bruce Dennla, a single rigid bar which rotation is allowable at the conjunction, is much thinner than DEA's two large shanks. On the other hand, the bridle type of shank is employed to transfer the loadings from mooring line to the fluke plate and the definition of fluke-shank angle becomes ambiguous in this case. Even though the installations of VLA's and DEA's are similar, the penetration depths of VLA's are typically greater since increasing of the fluke-shank angle increases both penetration depth and load capacity of the anchor.

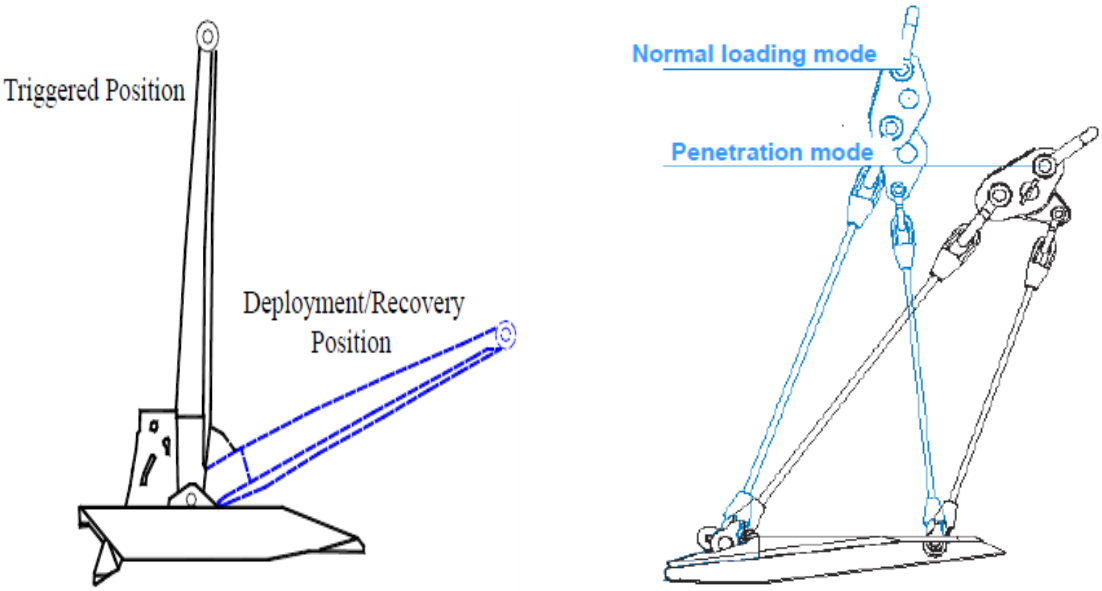

(a) BruceDennla MK3 (Kim, 2005) (b) Stevmanta VLA (Vryhof anchor)

Figure 1.9 Sechmatic of vertically loaded anchor

1.2.2.3 Installation of Drag Anchors

Typical methods for installation or retrieval of drag anchors are employed by means of anchor handling vessel (AHV). According to Vryhof anchor manual (2010), the general procedures composed of the following steps:

(1) Prepare to deploy the anchor and mooring line from the stern of the AHV.

(2) The anchor is deployed over the stern roller and the AHV pays out the mooring chain and lowers the anchor.

(3) The AHV moves to the location and continuous to pay out the mooring components or work wire to achieve the scope for the anchor.

(4) The anchor is then fluke set using the AHV bollard pull.

(5) The AHV moves a distance which is less than the water depth from the rig.

(6) The anchor penetrates into soil due to the dragging of the AHV.

(7) Measure the anchor line tension and line uplift angle at mudline during the dragging.

(8) The AHV keeps dragging until the line tension achieves the designed capacity.

With increasing the drag distance, both the anchor penetrating depth and line holding capacity increase. Figure 1.10 shows the profile of anchor system in soil and water column. The performance of cable line in air is governed by its self-weight and the mechanism was well-established by Meriam (1975); Aubeny and Chi (2010a) modified the model suitable for anchor line in water. On the other hand, Vivatrat et al. (1982) derived the governing differential equations for a perfectly flexible cable embedded in the soil by invoking equilibrium on a differential line segment; while the body weight of the chain is relatively small comparing with soil resistance and may be neglected, the closed-form solutions were proposed by Neubecker and Randolph (1995). Unlike the chain in water, the geometric shape of the anchor line in the soil deforms like a concave curve demonstrated in figure 1.10.

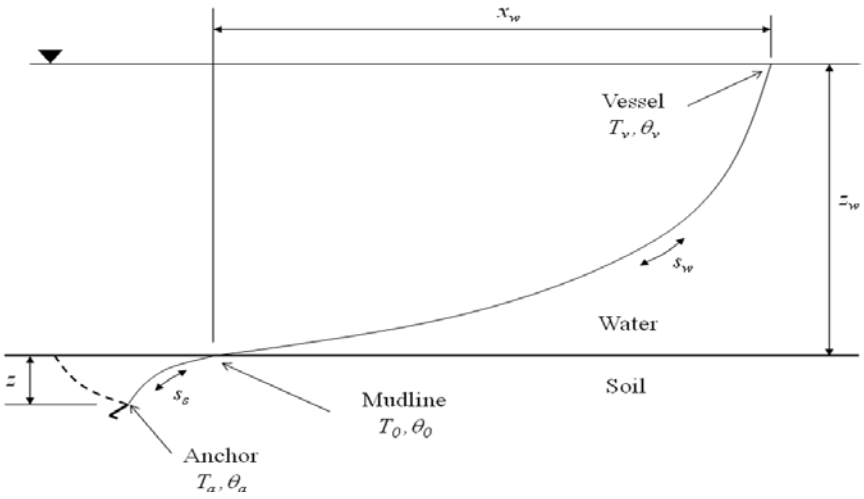

Figure 1.10 Anchor line system definition sketch

1.3 Outline and Objective of Research

1.3.1 Problem Statement

Among the anchor systems, drag embedment anchors (DEAs) are prominent for their economy and convenience of installation in deep waters. Historically they have had been used extensively for temporary moorings for offshore hydrocarbon exploration or mobile offshore drilling units. However, the difficulties of estimating the holding capacity and predicting the installation location are the two main intractable issues in application. For in-situ execution, the tension and orientation of the anchor chain at the mudline are measured data, but it may not be available to predict the whole anchor behavior based on these data and current simulation methods.

Under the circumstances of the effect of hurricanes, partial failure of a mooring system may occur. If one or more anchor lines fail, loads become re-distributed such that

the anchor line force no longer acts within the plane of intended loading for the anchor. The consequences of out-of-plane loading are not well understood at present.

Compared to mat foundations, the spudcan footing is an attractive option for jack-up platform for low cost and less impediment from the foundation while drilling. In the assessment of bearing capacity, the factor of safety may not be easy to estimate because the footing is subjected the combined loading (moment, vertical and horizontal forces). Although the evaluation of the stability of the foundation is based on load and resistance factor design (LRFD), the problem of the occurrence of additional large plastic displacement for the footing on which the environmental loadings apply could be serious. The difference of settlements among the individual legs is one of the possible factors that cause the failure of the whole structure.

1.3.2 Outline

To investigate and solve the problems presents above, the main criterion of this dissertation is to employ plasticity theory, such as plastic limit analysis, to analyze the performance of the anchor, chain, and spudcan foundation under the seabed. The issues of the research could be simply divided into three parts: mechanism of drag embedded anchors in a soft seabed, performance of drag embedded anchors under out of plane loadings, and stability assessment of spudcan foundation of Jack-up platforms.

The complexity and variety of the geometry of the anchor is the most intractable factor in the analysis; hence, a regular shape for the fluke and shank is necessary. In general, rectangular plate and cylindrical bar are commonly used for simulating the fluke and shank in the modeling (Yang et al., 2008, Aubeny and Chi, 2010a). Fluke length,

fluke thickness, shank length, angle between fluke and shank, and shank thickness are the considerable parameters in the analysis. The holding capacity and trajectory of the anchor are two primary purposes of the first stage study. Besides the fluke and shank properties, the direction of penetration and the rotation of the fluke are affected by the mooring chain. Although Neubecker and Randolph (1995) derived the closed-form solutions for chain geometry in soil, they focus on two special soil conditions: uniform soil and soil with bearing resistance proportional to depth but zero resistance at seabed surface. The undrained shear strength of typical cohesive soil could be presented as following equation:

$$S_u = S_{u0} + kz \tag{1.1}$$

where S_{u0} = undrained shear strength at mudline

k = Shear strength gradient

z = Depth below the mudline

Most of marine soils have nonzero shear strength at mudline and it also increases with depth, so does the soil resistance applied on the chain. Different bearing resistance profiles may affect the behavior and length of chain in the soils. In addition, the predictions of holding capacity and trajectory are required and important after the installation. Naval Civil Engineering Laboratory (NCEL, 1987), Vryhof Anchor (1999), and Bruce Anchor suggested the empirical chats and equations for estimating the anchor holding capacity; Stewart (1992), Neubecker and Randolph (1996), Dahlberg (1998), and Thorne (1998) recommended the prediction methods for both holding capacity and

trajectory based on limit equilibrium. In this research, a prediction method based on field measured data (tension and chain angle at mudline) is proposed.

During the hurricanes Ivan, Katrina, and Rita in 2005, there were about seventeen offshore mobile drilling units drifting due to the failure of the mooring system. Partial failure of mooring systems for floating structure will subject drag anchor to loads having an appreciable component outside of the intended plane of loading. Under this circumstance, the anchor may travel out of the installation plane direction. Similar to in-plane (installation plane) motion, both the holding capacity and trajectory of the anchor are main concern issues in out of plane motion. The analysis shows that, if the self-weight of the anchor chain is neglected, the anchor chain configuration will lie always within a plane, although for general conditions of out-of-plane loading, the anchor chain will lie in an oblique plane defined by the direction of the anchor chain at the pad-eye and the mudline (Aubeny and Chi 2010b).

Based on Guidelines for Site Specific Assessment of Mobile Jack-Up Units proposed by The Society of Naval Architects and Marine Engineering (SNAME), the typical analysis of the spudcan foundation of jack-up units include preloading, bearing capacity, and the displacement assessment. During the stage of preloading, the settlement of a spudcan in soft clay may be five time as deep as that in sand. The magnitude of sliding capacity, for a pinned condition footing, is mainly affected by the penetration depth. When the contribution of the soil moment resistance is considered, a three-stage assessment procedure is recommended: plotting of the configuration of yield surface and environmental forces, computing the value of yield function with external forces

substituted, and computing the factor of safety of the spudcan. In addition, the results of the assessment may be ambiguous while the different yield functions are employed to analyze the spudcan in soft clay. It should be noted that the additional settlement (plastic displacement) of the footing may occur if the jack-up unit experiences environmental forces beyond its site-specific design.

CHAPTER II

OVERVIEW OF CURRENT ANALYSIS METHODS

2.1 Analysis of Anchors

The current methods employed in analyzing drag anchors include empirical methods, limit equilibrium methods, plastic limit analysis method, and upper bound collapse load analysis.

2.1.1 Empirical Methods

Design charts of holding capacity or drag and penetration are the typical form for empirical methods. Each type of anchor has separate design charts or empirical equations based on regression of test data.

2.1.1.1 Vryhof Anchor Method

Vryrof Anchor (2010) proposed empirical charts, equations, and tables for predicting holding capacity, drag distance, and penetrating depth of drag anchors. Since the method is experimental, each type anchor has a separate formula or chart for prediction. For example, from Figure 2.1 to 2.4 are the design charts for Stevin MK3 and Stevpris MK5 anchor. The ultimate holding capacity (UHC) is taken to be proportional to the size (weight) of the anchor and the UHC for Stevpris MK5 is relatively greater than that of Stevin MK3 in the same soil; on the other hand, the penetration depth increases with drag distance and the later is probably seven to ten times of the former. Table 2.1 presents the relationships among ultimate holding capacity, drag distance, and penetration depth for both Stevpris MK5 and Stevin MK3. The first column of data

means while anchor loading is 70% of UHC, the corresponding percentage of drag and penetration to their maximum value are 48% and 80%. The anchor load as percentage of UHC (1st column) is comparable to penetration depth as percentage of maximum depth. This phenomenon also implies that holding capacity of anchor is closely related to penetration depth. It should be noted that the UHC lines are applicable in soil with undrained shear strength of 4 kPa at the mudline with a strength gradient of 1.5 kPa per meter depth. In very soft clay, the optimum fluke-shank angle is 50 degrees and 32 degrees in sand or hard clay.

Table 2.1 Percentage of mobilization for anchor capacity, drag, and penetration (Vryhof)

Anchor load as percentage of UHC	Drag as of percentage maximum drag distance	Penetration as percentage of maximum penetration depth
70	48	80
60	37	68
50	27	55
40	18	42
30	9	23

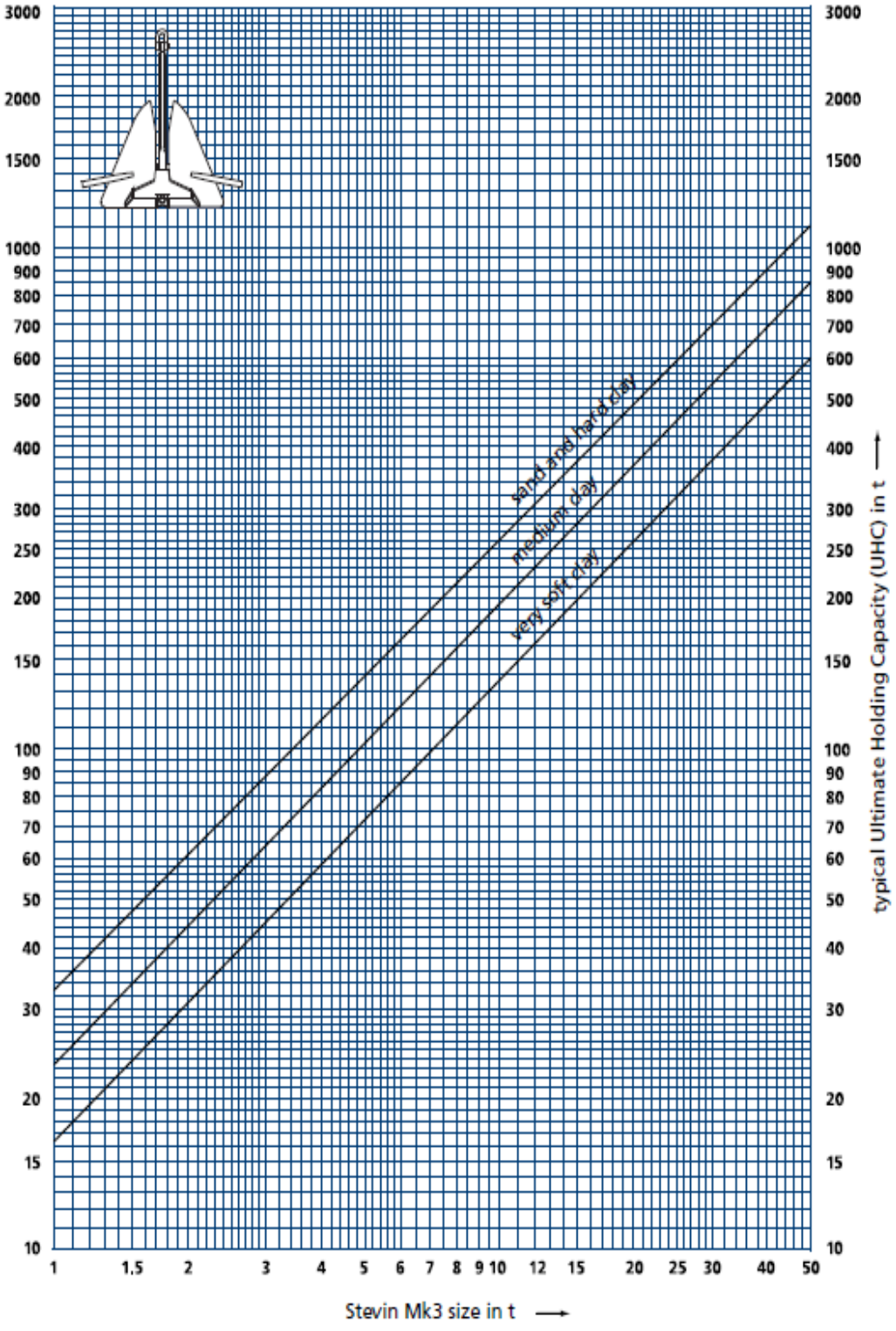

Figure 2.1 UHC chart for Stevin MK3 anchor (Vryhof, 2010)

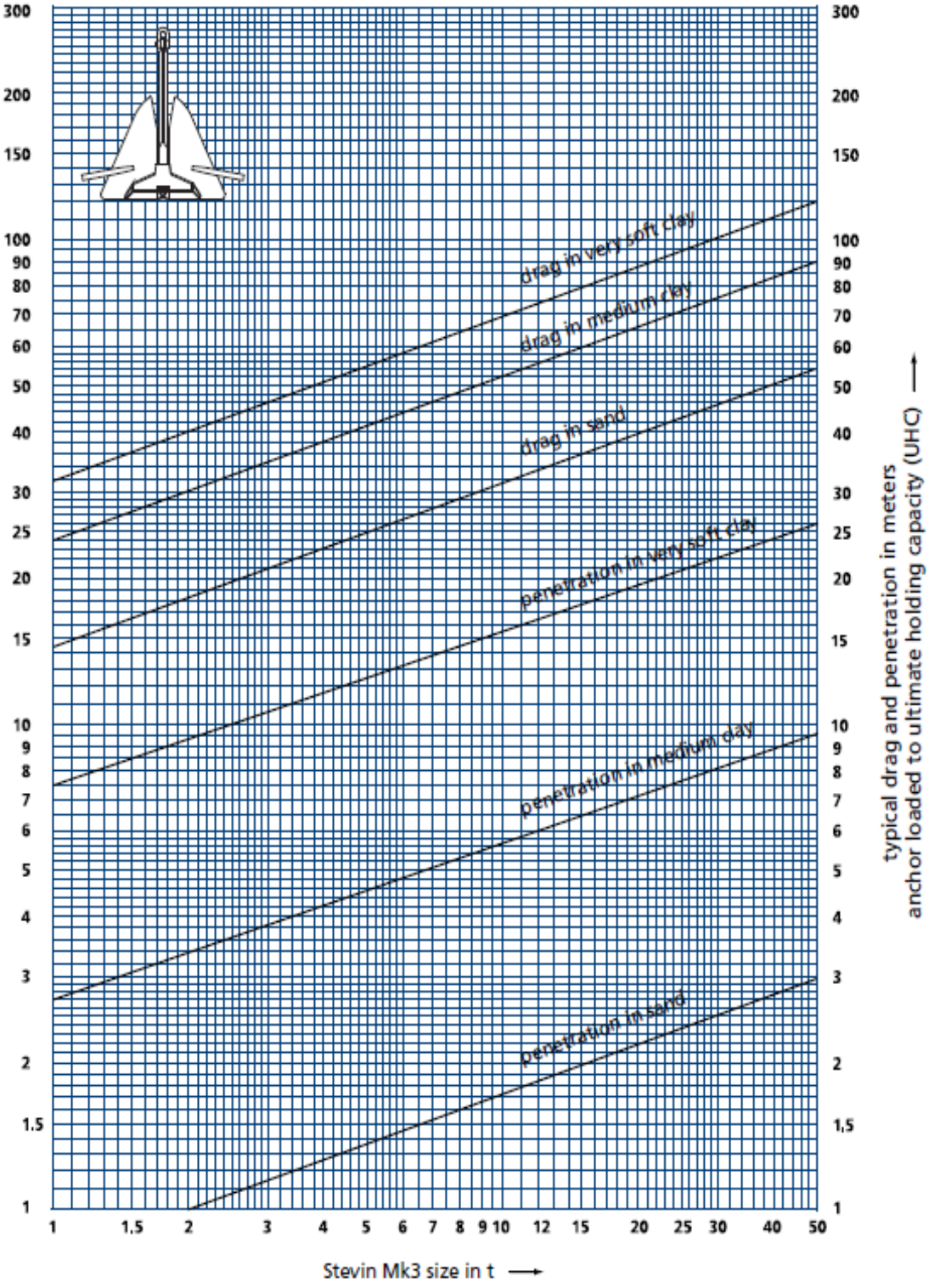

Figure 2.2 Drag and penetration design chart for Stevin MK3 anchor (Vryhof, 2010)

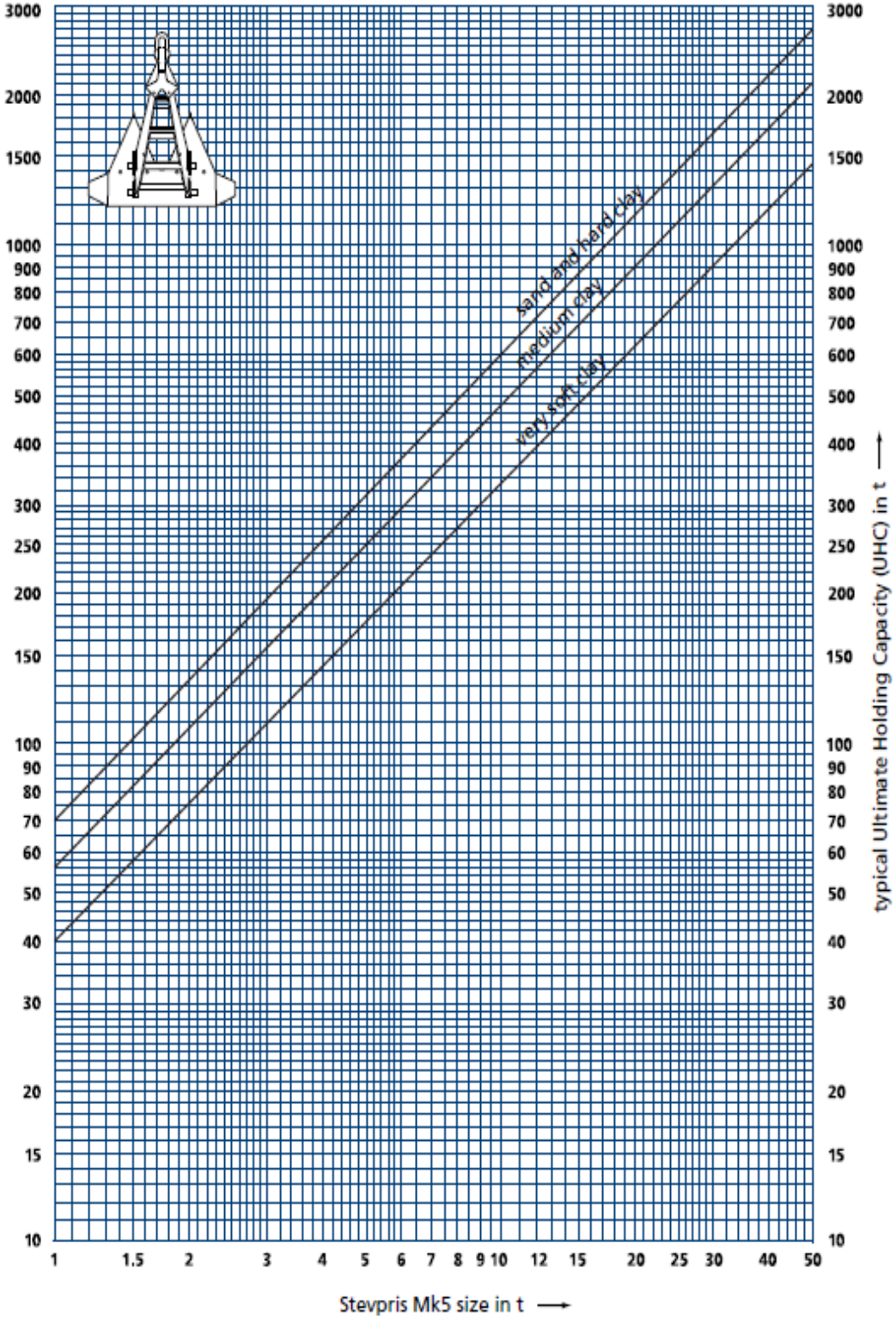

Figure 2.3 UHC chart for Stevin MK5 anchor (Vryhof, 2010)

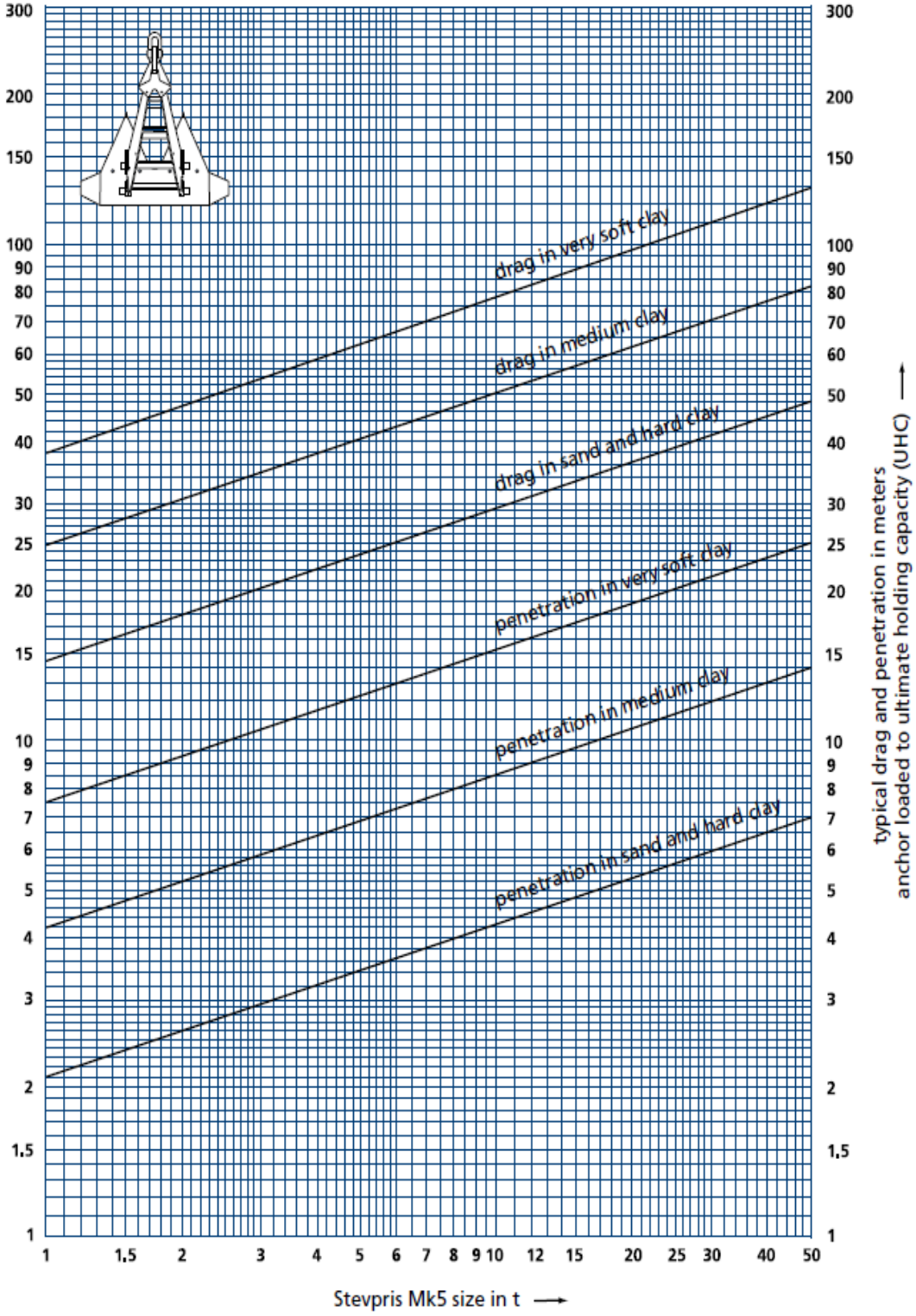

Figure 2.4 Drag and penetration design chart for Stevpris MK5 anchor (Vryhof, 2010)

The design chart of Vryhof Stevmanta, a typical vertically loaded anchor, shows the ultimate pull capacity (UPC) increases with diameter of the mooring line (Figure 2.5). The UPC also could be estimated by the following equation:

$$UPC = N_c \cdot S_u \cdot A \tag{2.1}$$

where N_c = Dimensionless pull-out bearing capacity factor

S_u = kD, Undrained shear strength

k = Soil strength gradient

D = embedded depth

A = Fluke area

The concept of this empirical equation is similar to the assessment of bearing capacity of a shallow foundation. The value of dimensionless pull-out bearing factor N_c is suggested as 10 in this equation. The undrained shear strength S_u is proportional to the embedded depth D which could be determined by Equation 2.2:

$$D = 1.5k^{0.6} \cdot d^{0.7} \cdot A^{0.3} \cdot \tan^{1.7}(\alpha) \tag{2.2}$$

where d = Mooring line diameter

k = Soil strength gradient

α = Fluke-shank angle

A = Fluke area

The default values for fluke-shank angle α and soil strength gradient k in the design chart are 50 (degrees) and 2 (kPa/m) respectively.

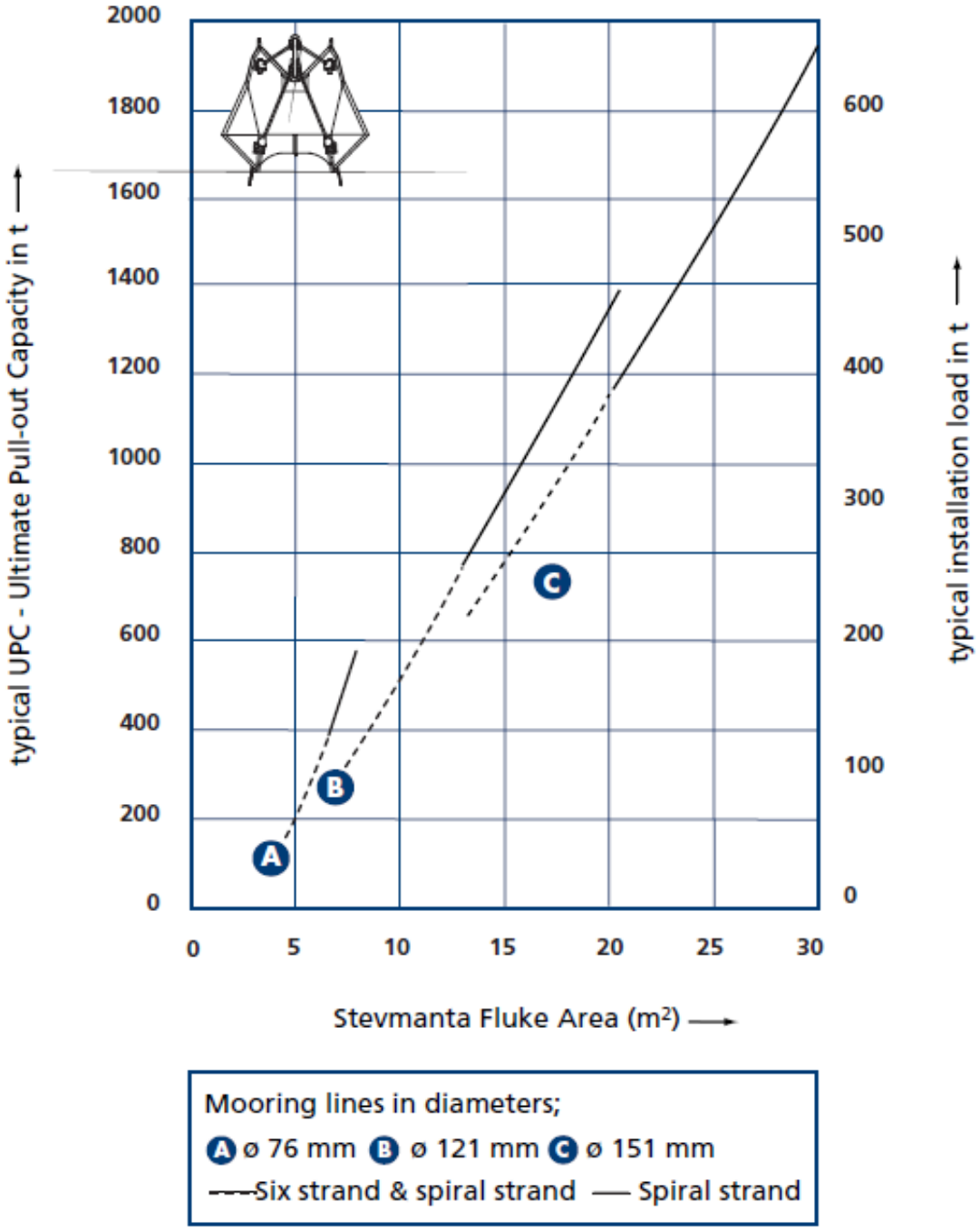

Figure 2.5 Design chart for Stevmanta VLA (Vryhof, 2010)

2.1.1.2 Bruce Anchor Method

Bruce Anchor proposed the empirical design charts and corresponding equations for estimating holding capacity of the anchor. In the same soil (mud), from Figure 2.6 and 2.7, the holding capacity of wire mooring line is higher than that of chain mooring line and the difference between two values increases with the size of the anchor. In general, the holding capacities of anchors or the bearing capacities of footings in cohesive soils are relatively lower than those in sands; therefore, wires may be an attractive option for low strength mud. The corresponding holding capacity regression equations are also available for both types of anchors:

$$\left.\begin{aligned} HC_{(chain/sand)} &= 60.92 \cdot W^{0.94} \\ HC_{(chain/mud)} &= 45.94 \cdot W^{0.92} \\ HC_{(wire/mud)} &= 57.11 \cdot W^{0.92} \end{aligned}\right\} \quad \text{Bruce PM Anchor} \tag{2.3}$$

$$\left.\begin{aligned} HC_{(chain/sand)} &= 46.86 \cdot W^{0.94} \\ HC_{(chain/mud)} &= 39.95 \cdot W^{0.92} \\ HC_{(wire/mud)} &= 49.66 \cdot W^{0.92} \end{aligned}\right\} \quad \text{Bruce FFTS MK4 Anchor} \tag{2.4}$$

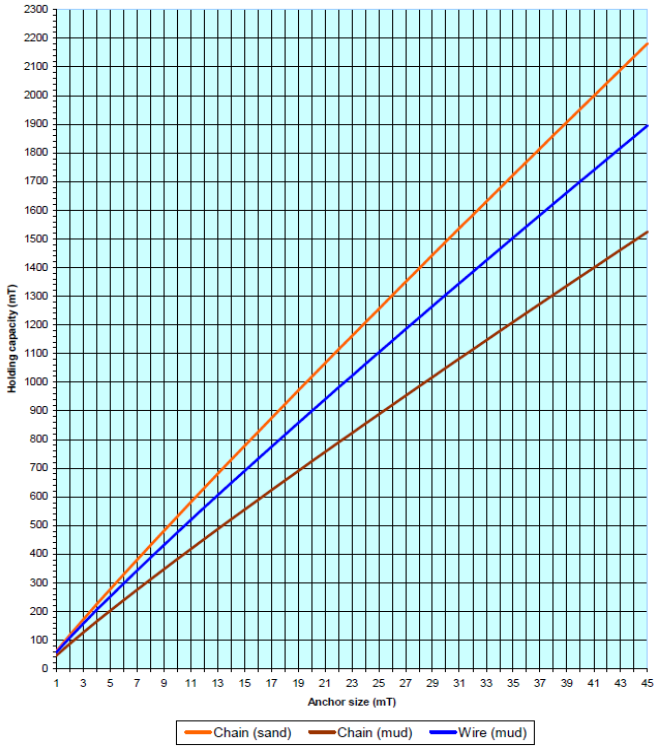

Figure 2.6 Design chart for Bruce PM Anchor (courtesy of Bruce Anchor)

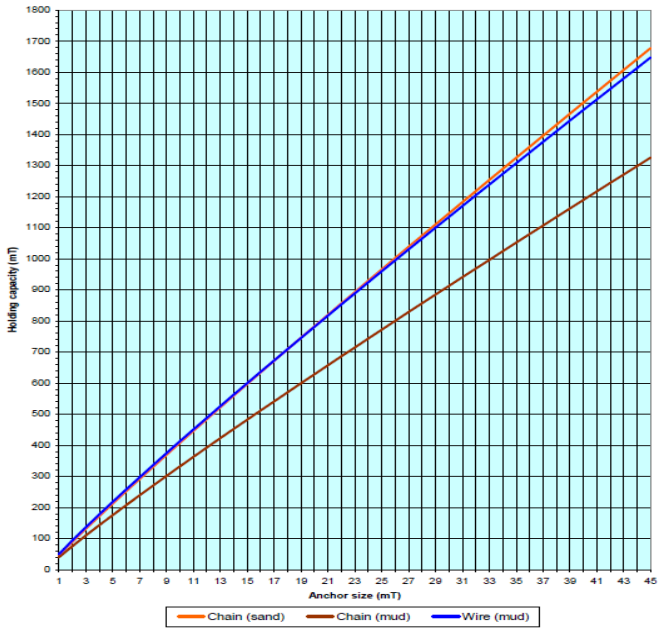

Figure 2.7 Design chart for Bruce FFTS MK4 Anchor (courtesy of Bruce Anchor)

2.1.2 Limit Equilibrium Method

Based on the methods for analyzing static and kinematic performances of drag anchors in cohesive soil proposed by Stewart (1992) and the embedded chain solutions for anchor pile (1995), Neubecker and Randolph (1996) published a numerical method to assess the anchor trajectory and tension at the padeye. Lelievre and Tabatabaee (1979, 1981) developed a limit equilibrium method for drag analysis in sand which was further developed by Neubecker and Randolph (1996). O'Neill, Randolph, and House (1999) employed the method to predict the anchor performance in layered soils (a clay layer overlying sand).

Figure 2.8 presents the forces system for the approach of Neubecker and Randolph of the anchor in cohesive soil. The geotechnical resistance force T_p is parallel to the penetrating direction of the fluke and could be expressed by the following equation:

$$T_p = fA_p N_c S_u \tag{2.3}$$

where f = Form factor

A_p = Frontal projected anchor area in a plane perpendicular to the fluke

N_c = Bearing capacity

S_u = Undrained average shear strength

However, there also exists a normal soil resistance acting on the anchor and the resultant resistance force T_w is calculated by equation 2.4:

$$T_w = \frac{T_p}{\cos\theta_w} \tag{2.4}$$

where θ_w = Geometric characteristic parameter

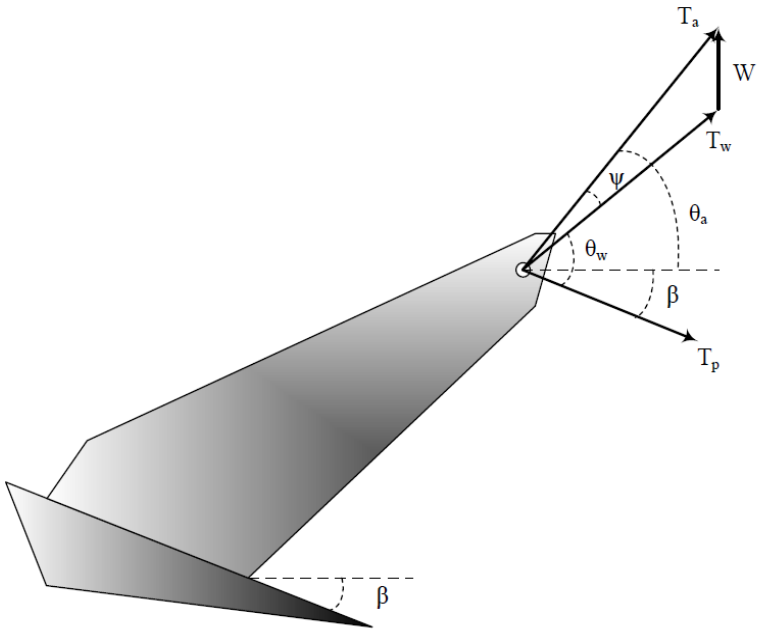

Figure 2.8 Sketch of anchor force system of Neubecker and Randolph approach

Both f and θ_w are anchor resistance parameters and can be determined by field tests or centrifuge tests. The padeye force T_a is estimated by taking into account the weight of anchor W and is supposed to be at angle of θ_a and ψ corresponding to the horizontal and resultant resistance force respectively. The orientation of the fluke has an angle β to the horizontal and it follows that:

$$\beta = \theta_w + \psi - \theta_a \tag{2.5}$$

where the chain angle θ_a obeys the anchor line tension equation:

$$\frac{T_a \theta_a^2}{2} = D\bar{Q} \tag{2.6}$$

where $\bar{Q}$ is the average resistance acting on the chain. The trajectory of the anchor can be simulated as following steps:

1. The fluke has an initial angle β to the horizontal and travel with an incremental horizontal distance Δx
2. With the direction of the penetration parallel to the previous fluke orientation, calculate the embedded depth D.
3. Estimate soil resistance forces T_p and T_w from equations 2.3 and 2.4 and then calculate padeye tension T_a by using force triangle composed of resultant resistance T_w and anchor weight W.
4. Calculate chain angle θ_a by equation 2.6.
5. Compute the new fluke orientation angle β by equation 2.5.
6. Advance the anchor a further horizontal distance Δx and loop to step 2.

2.1.3 Plastic Limit Method

O'Neill et al. (2003) employed the concept of plastic yield functions (loci) and associated flow rule in plasticity theory and combined them with chain solutions developed by Neubecker and Randolph (1995) to construct a model for predicting the trajectory and shackle tension of rectangular and wedge-shaped anchors. In the model (Figure 2.9), the chain load T_a applied on the padeye and can be expressed in terms of normal force (V) and parallel force (H) to the top of the fluke and a negative moment (M) to the fluke reference point. The offset form of yield loci proposed by Murff (1994) was utilized:

$$f = \left(\frac{V - V_1}{V_{max} - V_1} \right)^q + \left[\left(\frac{M - M_1}{M_{max} - M_1} \right)^m + \left(\frac{H - H_1}{H_{max} - H_1} \right)^n \right]^{\frac{1}{p}} - 1 \qquad (2.7)$$

where f = Yield function

V_{max} = Maximum vertical load

H_{max} = Maximum horizontal load

M_{max} = Maximum moment load

V_1, H_1, and M_1 = Offset loads

m, n, p, and q = Exponents

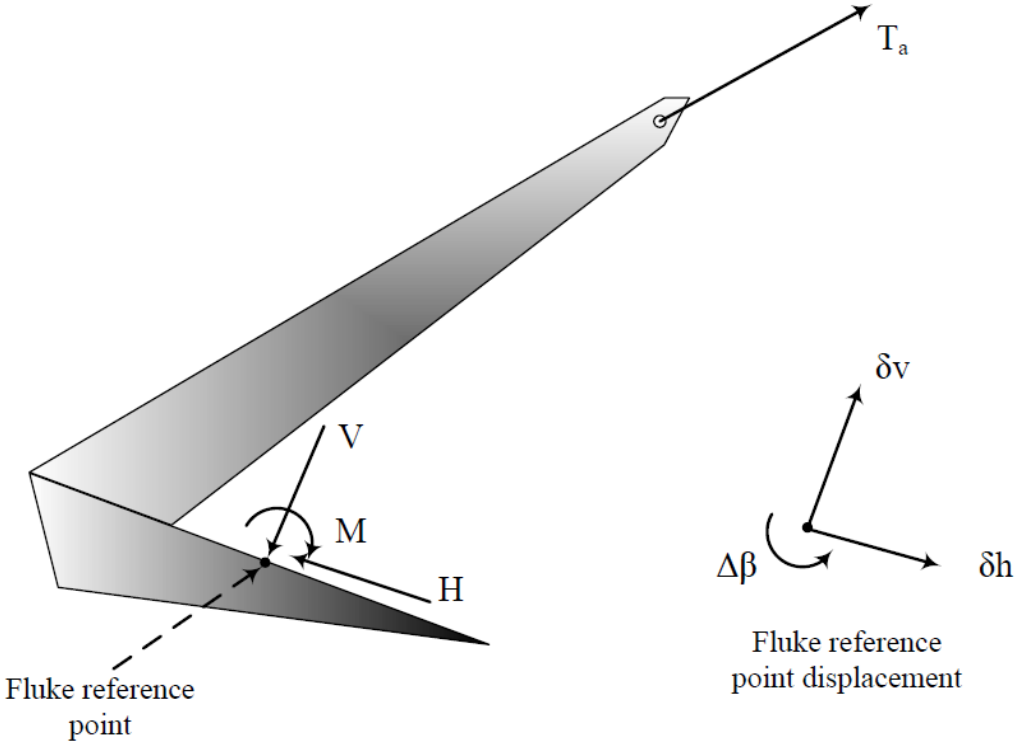

Figure 2.9 Sketch of anchor forces and displacements system in the method of O'Neill et al (2003).

The maximum vertical, horizontal, and moment loads can be estimated by means of upper bound methods (Bransby and O'Neill, 1999) and expressed as followings:

$$\frac{V_{\max}}{L_f S_u} = 4\left(\pi - \alpha + \frac{\tan\alpha}{2}\right) + 4\frac{t}{L_f}\left(\frac{1}{2} + \cos\alpha\right) \tag{2.8}$$

$$\frac{H_{\max}}{L_f S_u} = 4\frac{t}{L_f}\left(\pi - \alpha + \frac{\tan\alpha}{2}\right) + 4\left(\frac{1}{2} + \cos\alpha\right) \tag{2.9}$$

$$\frac{M_{\max}}{L_f^2 S_u} = \frac{\pi}{2}\left[1 + \left(\frac{t}{L_f}\right)^2\right] \tag{2.10}$$

where L_f = Length of the fluke

t = Thickness of the fluke

α = Angle of rigid wedge (defined in Figure 2.10 and 2.11)

Figures 2.10, 2.11, and 2.12 present the upper bound mechanisms of anchor subject pure vertical, horizontal, and moment loads. The derivations of these three equations will be discussed in next chapter—plasticity theory. In addition, Bransby and O'Neill (1999) also recommended the best-fit solutions for exponents and offset loads from finite element results shown in Table 2.2. Assuming an the associated flow rule, the relative displacement and rotation corresponding to the horizontal displacement increment are shown in the following equations:

$$\frac{\delta v}{\delta h} = \frac{\delta f}{\delta V} \Big/ \frac{\delta f}{\delta H} \tag{2.11}$$

$$\frac{\delta \beta}{\delta h / L_f} = \frac{\delta f}{\delta (M / L_f)} \Big/ \frac{\delta f}{\delta H} \tag{2.12}$$

Once the incremental distance Δh parallel to the fluke top surface is chosen, the incremental distance Δv perpendicular to the fluke and rotation of the fluke reference point could be computed by the following:

$$\Delta v = \left(\frac{\delta f}{\delta V} \Big/ \frac{\delta f}{\delta H} \right) \Delta h \tag{2.11}$$

$$\Delta \beta = \left(\frac{\delta f}{\delta (M / L_f)} \Big/ \frac{\delta f}{\delta H} \right) \frac{\Delta h}{L_f} \tag{2.12}$$

Table 2.2 Yield locus curve-fitting parameters (Bransby and O'Neill, 1999)

Parameter	Rectangular fluke	Wedge fluke
$H_{max}/ (L_f S_u)$	4.29	3.34
$V_{max}/ (L_f S_u)$	11.87	11.53
$M_{max}/ (L_f^2 S_u)$	1.49	1.60
$H_1/ (L_f S_u)$	0	0
$V_1/ (L_f S_u)$	0	-1.25
$M_1/ (L_f^2 S_u)$	0	-0.57
m	1.26	2.37
n	3.72	2.14
p	1.09	0.93
q	3.16	3.41

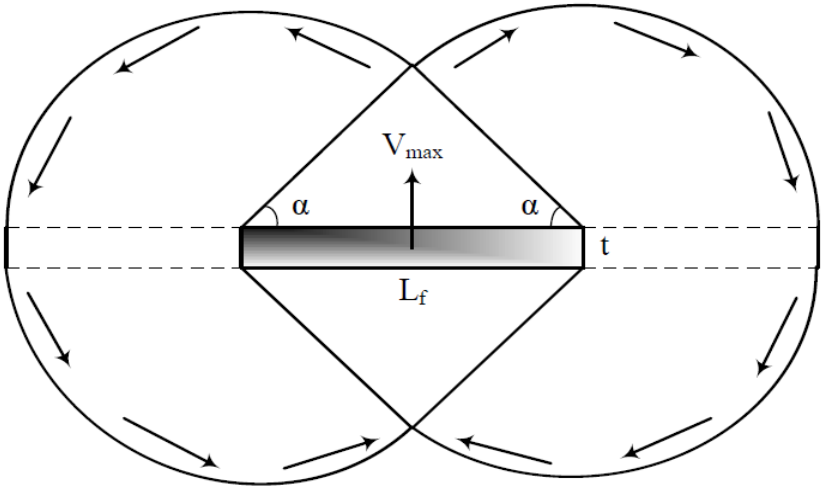

Figure 2.10 Upper bound mechanism of the anchor subjecting pure normal load

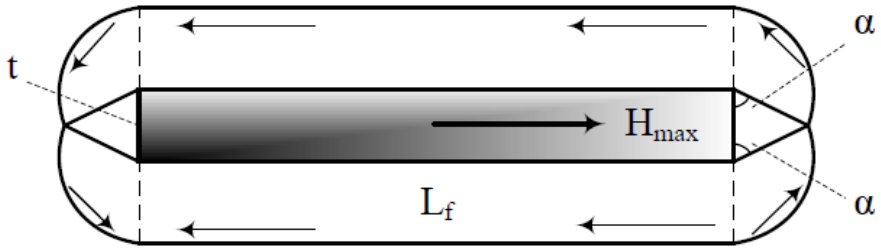

Figure 2.11 Upper bound mechanism of the anchor subjecting pure tangential load

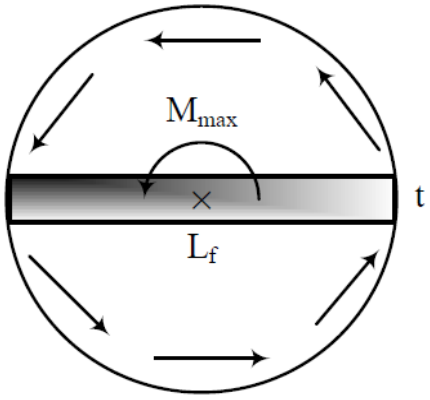

Figure 2.12 Upper bound mechanism of the anchor subjecting pure moment

2.1.4 Upper Bound Collapse Load Analysis

Aubeny et al. (2005, 2008) combined the chain solutions for calculating the rotation of line angle at the shackle and upper bound collapse load analysis for obtaining bearing factor of anchors to predict the trajectory and holding capacity of anchors. Equation 2.6 is the original form of the chain equation and it can be modified as following for the strength of the soil increasing with the depth:

$$\frac{T_a\left(\theta_a^2-\theta_0^2\right)}{2}=z\overline{Q}=zE_nN_cb(S_{u0}+kz/2) \tag{2.13}$$

where T_a = Anchor line tension at shackle point

θ_a = Anchor line angle from horizontal at shackle point

θ_0 = Anchor line angle from horizontal at mudline

E_n = Multiplier to be applied to chain bar diameter

N_c = Dimensionless bearing factor for wire anchor line

b = Chain bar or wire diameter

S_{u0} = undrained shear strength at mudline

k = Shear strength gradient

z = Depth below the mudline

Both the line angle θ_a and the orientation of fluke θ_f definitely vary during the penetration and the changing of the chain angle $\Delta\theta_a$ is assumed to match the changing of the fluke $\Delta\theta_f$ in the analysis. The changing of the anchor line angle evolves from the equation 2.14 and shown as follows:

$$\frac{d\theta_a}{d\hat{z}} = \frac{1}{\theta_a}\left[\frac{E_n N_c}{T_a^*} - \frac{\left(\theta_a^2 - \theta_0^2\right)}{2\left(1/\eta + \hat{z}\right)}\right] \tag{2.14}$$

where $\hat{z}$ = Normalized depth of shackle = z/b

η = Strength gradient parameter = bk/ S_{u0}

T_a^* = Normalized shackle tension = T_a/ $S_{u0}b^2$

According to the field test data in Gulf of Mexico (Joint Industry Project), the normalized shackle tension approaches to a constant after few embedded depth (Aubeny, 2008). If the shank effect can be neglected, the shackle tension should be definitely equal to the soil resistance force acting on the fluke. By means of upper bound load analysis, the soil resistance on fluke can be estimated by the equation:

$$F = N_e A_f S_u \tag{2.15}$$

Where A_f = Fluke area

N_e = Effective bearing factor of fluke

In general, the common value of N_e ranges from 3.5 to 7 for most of anchors. By introducing equation 2.15, the normalized shackle tension becomes:

$$T_a^* = \frac{N_e A_f}{b^2} \tag{2.16}$$

Combined with the equations stated above, the algorithm for computing the anchor trajectory can proceed as following steps:

1. Advance the anchor an incremental distance Δs in the direction parallel to the fluke with an angle θ_f to the horizontal.

2. Compute the corresponding incremental vertical penetration $\Delta z = \Delta s \sin \theta_f$ and horizontal drag distance $\Delta x = \Delta s \cos \theta_f$.
3. Calculate the changing rate of the line angle at shackle from equation 2.14 and it is equal to that of rotation of the fluke.
4. Estimate the incremental angle change by $\Delta\theta_a = \left(\frac{d\theta_a}{dz}\right)\Delta z$.
5. Update the next step fluke angle $\theta_{f,i+1} = \theta_{f,i} + \Delta\theta_a$ and the next step anchor line angle $\theta_{a,i+1} = \theta_{a,i} + \Delta\theta_a$.
6. Repeat steps 1 through 6 until the fluke approaches horizontal orientation.

2.2 Analysis of Spudcans

The guideline for the assessment of spudcan foundations in Technical & Research Bulletin 5-5A (2002) proposed by The Society of Naval Architects and Marine Engineers (SNAME) offer a good criterion for analyzing and design of spudcan footing. In general cases, preloading assessment, bearing capacity calculation, and settlement evaluation are three main issues; however, the situation becomes complicated when the footing is located in layered soils or in very soft clay.

In evaluating the bearing capacity of the footing, the vertical-horizontal bearing capacity interaction model is widely used but the results may be too conservative. A more realistic assessment of bearing capacity is possible by considering the contribution of the soil rotational resistances, the interaction yield functions of vertical-horizontal-rotational are developed (SNAME, 2002; Van Langen et al., 1993; Martin and Houlsby, 2000 & 2001). The yield functions suggested by Martin and Houlsby, verified by the

laboratory tests, illustrate the performance of the spudcan in cohesive soils well for both full penetration and partial penetration. Although SNAME recommended some criteria and yield function for sand, more field data or lab tests may be necessary for verification.

The problem of clay squeezing occurs when a soft clay layer overlies a significantly stronger layer (Figure 2.13). Under the assumption of no soil back-flow condition, the ultimate vertical bearing capacity of footing is suggested by Meyerhof (SNAME, 2002):

$$F_v = A\left\{\left(a + \frac{bB}{T} + \frac{1.2D}{B}\right)C_u + P_0'\right\} \geq A\left\{N_c s_c d_c C_u + P_0'\right\} \tag{2.17}$$

where a = Squeezing factor = 5.00 (recommended)

b = Squeezing factor = 0.33 (recommended)

A = Spudcan effective bearing area based on cross-section

B = Effective spudcan diameter

C_u = Undrained shear strength at D+B/4 below the mudline

P_0' = Effective overburden pressure at depth D

T = Thickness of the soft clay layer

d_c = Bearing capacity depth factor

s_c = Bearing capacity shape factor

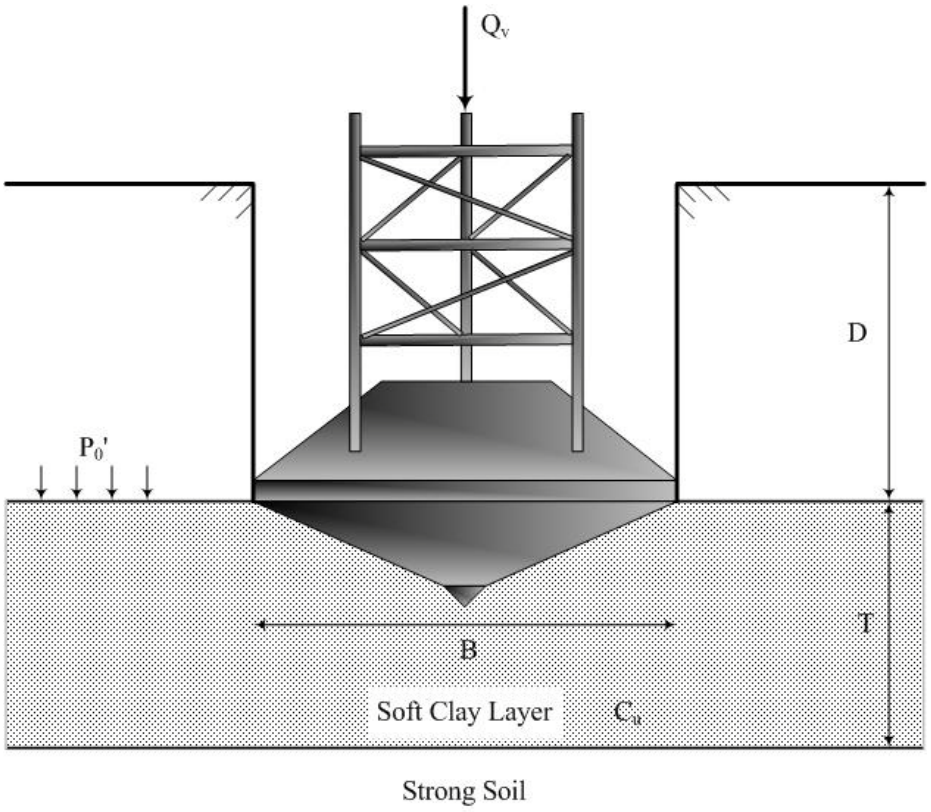

Figure 2.13 Problem of clay-squeezing of spudcan foundation

Another difficult problem (Figure 2.14) is the punching failure of the spudcan foundation while a strong soil (hard clay or sand) overlyies a weak, soft clay soil. Under the assumption of no soil back-flow condition, the ultimate vertical bearing capacity can be computed according to the following (SNAME):

$$F_v = A\left\{3\frac{H}{B}C_{u,t} + N_c s_c\left(1+0.2\frac{D+H}{B}\right)C_{u,b} + P_0'\right\} \le A\left\{N_c s_c d_c C_{u,t} + P_0'\right\} \qquad (2.18)$$

where $C_{u,b}$ = Undrained shear strength for the lower soil below the spudcan (weak layer)

$C_{u,t}$ = Undrained shear strength for the upper soil below the spudcan (strong layer)

H = Distance from spudcan maximum bearing area to the top of the weak layer

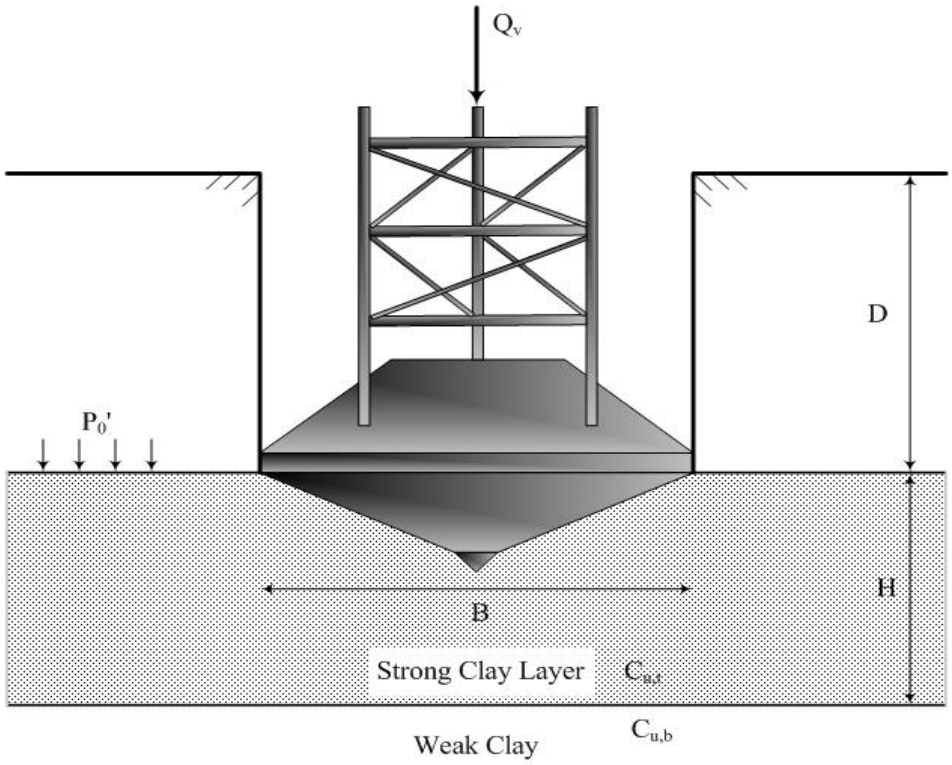

Figure 2.14 Problem of punching-through of spudcan foundation

CHAPTER III

SOIL PLASTICITY THEORY AND APPLICATIONS

3.1 Concepts of Soil Plasticity Theory

Plasticity theory has been widely employed in soil mechanics and its application can be traced back to the assessment of the stability of embankments proposed by Coulomb in 1770's. It was initially developed in connection with estimating the failure condition and then greatly expanded to the most sophisticated numerical analysis that is carried on in the field today (Murff, 2006). There are four main components in soil plasticity theory: yield criterion (yield surface), elastic behavior beneath yield, flow rule, and hardening law. The elastic stress-strain behavior is employed before the current stress state of soil element touches the yield criterion, i.e., it is insides the yield surface.

3.1.1 Yield Criterion

The core element in plasticity theory is yield criterion which presents a relationship among stress components at which incipient yield occurs (Murff, 2006). At the primary stage of investigating a new material, experimental data are required to determine the condition of yielding and then generalized them as the parameters we are interested. For example, the unconfined compression strength q_u is the datum measured from the laboratory test and it is generalized as the shear strength S_u shown in the following equation:

$$S_u = \frac{q_u}{2} \tag{3.1}$$

The yield criterion can be expressed in mathematical form as a function of the current stress state σ_{ij}:

$$F\left(\sigma_{ij}\right)=0 \tag{3.2}$$

The yield function F also can be presented as a surface in stress space (Figure 3.1). Actually, equation 3.2 shows the current stress state σ_{ij} is exactly on the yield surface. It is impossible for a stress state locates outside the yield surface; on the other hand, the soil is elastic when the value of yield function at the current stress substituted is less than zero.

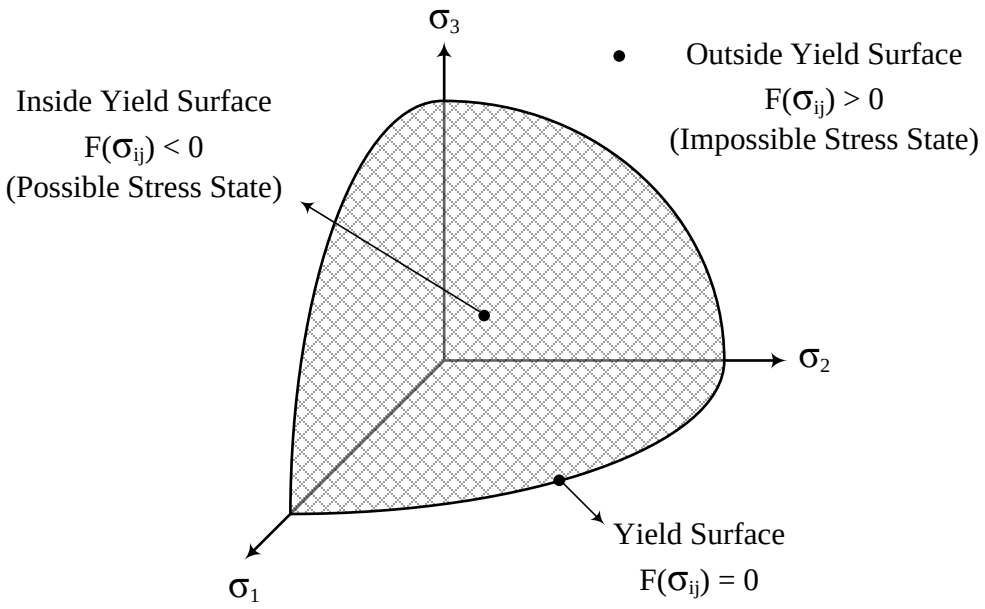

Figure 3.1 Yield surface and stress state in stress space

A common yield criterion for undrained analysis is Tresca assumption (maximum shear stress criterion) which is written as:

$$\tau_{\max} = \frac{\sigma_1 - \sigma_3}{2} = S_u \quad \text{or} \quad F(\sigma_{ij}) = \sigma_1 - \sigma_3 - 2S_u = 0 \tag{3.3}$$

where τ_{max} = Maximum shear stress

σ_1 = Maximum principle stress

σ_3 = Minimum principle stress

From the above equation, it is obvious that the allowable shear stress should be equal or less than the undrained shear strength in Tresca criterion. In application, it is widely used for such analysis such as slope stability analysis and bearing capacity assessment. Although this criterion describes the undrianed behavior of soil acceptably, the situation becomes complicated for analyzing a three dimensional problem. The effect of the intermediate principle stress plays no role in the method. The extended Tresca criterion, shown as following equation, improves the limitation of original form with considering the influence of intermediate principle stress σ_2:

$$\frac{\sigma_1 - \sigma_3}{\sigma_1 + \sigma_2 + \sigma_3} = \beta \tag{3.4}$$

where β = Constant

Another alternative yield criterion is the Von Mises criterion which involves the effects of shear in all direction:

$$J_2^{1/2} - k = 0 \quad \text{or} \quad \left\{\frac{1}{6}\left[(\sigma_1 - \sigma_2)^2 + (\sigma_2 - \sigma_3)^2 + (\sigma_3 - \sigma_1)^2\right]\right\}^{1/2} - k = 0 \tag{3.5}$$

Where J_2 = Second invariant of stress deviation tensor

k = Constant

Figure 3.2 showing two criteria in π-plane, Von Mises yield surface is the circumscribed circle of the hexagonal Tresca surface.

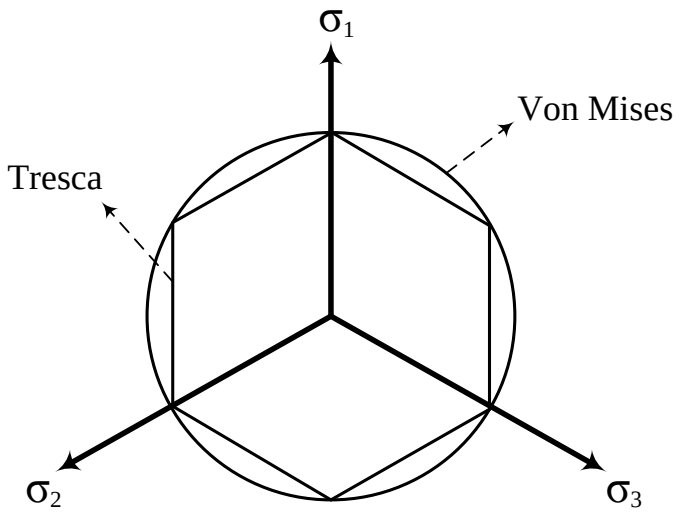

Figure 3.2 Tresca and Von Mises yield criteria in π-plane

3.1.2 Flow Rule and Hardening Law

While the current stress state is inside the yield surface, the elastic stress-strain relationship is employed for the soil. For isotropic material, it can be presented as following:

$$\sigma_{ij} = \lambda \delta_{ij} \varepsilon_{kk} + 2\mu \varepsilon_{ij} \tag{3.6}$$

where λ and μ = Lame constants

σ_{ij} = Elastic stress tensor

ε_{ij} = Elastic strain tensor

δ_{ij} = Kronecker Delta

ε_{kk} = Volume strain = $\varepsilon_{11} + \varepsilon_{22} + \varepsilon_{33}$

When the state of stress reaches the yield surface, the behavior of soil element changes from elastic to plastic. On the yield surface, the direction and magnitude of the plastic flow could be described by the plastic potential function (surface) G as the following equation:

$$\dot{\varepsilon}_{ij}^{p} = \dot{\Lambda}\frac{\partial G}{\partial \sigma_{ij}} \tag{3.7}$$

where $\dot{\Lambda}$ = Scalar multiplier

$\dot{\varepsilon}_{ij}^{p}$ = Plastic strain increment

Actually, the equation implies that the direction of the plastic strain rate is governed by the gradient of the plastic potential function $\frac{\partial G}{\partial \sigma_{ij}}$ and the magnitude is governed by the scalar multiplier $\dot{\Lambda}$. If the gradient of the yield function $\frac{\partial F}{\partial \sigma_{ij}}$ equals the gradient of plastic potential function (i.e., the soil obeys an associated flow law), the plastic strain increment could be determined from yield function:

$$\dot{\varepsilon}_{ij}^{p} = \dot{\Lambda}\frac{\partial F}{\partial \sigma_{ij}} \tag{3.8}$$

In this case, the direction of the plastic flow is perpendicular to the yield surface (Figure 3.3).

According to Drucker's stability postulate of non-softening materials, there are two type of plastic behavior: perfectly plastic and work hardening plastic. Once the soil element yields, for perfectly plastic materials (Figure 3.4 (a)), the plastic strain can

increase with no limit; whereas, a work hardening material continues to increase its stress level beyond yield.

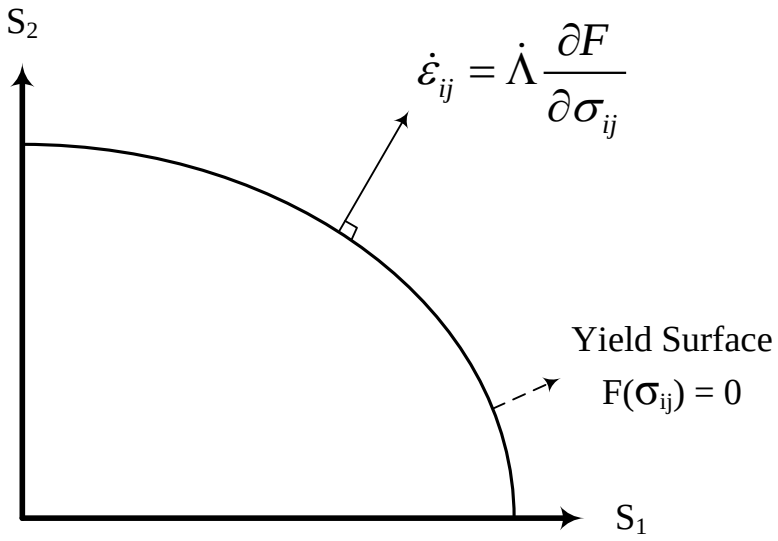

Figure 3.3 Direction of plastic flow under associated flow rule

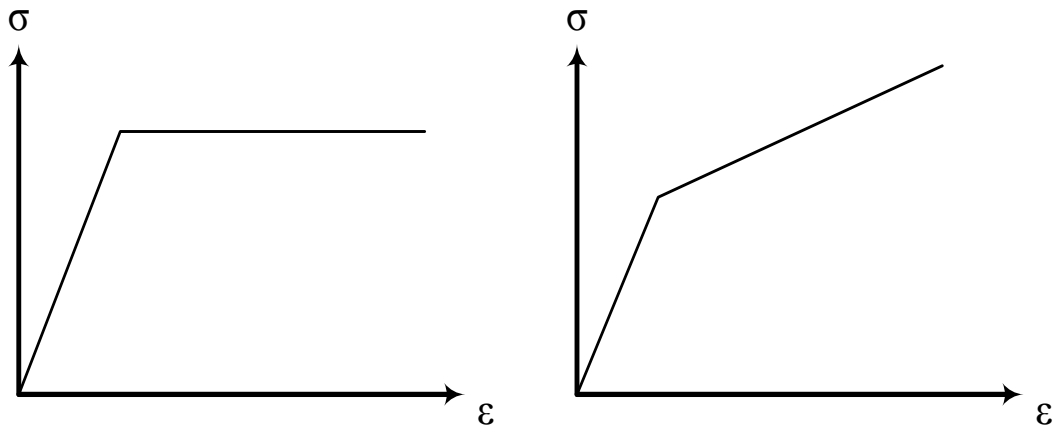

(a) Elastic Perfectly-Plastic Model (b) Work Hardening Plastic Model

Figure 3.4 Plastic models for stable materials

3.2 Lower Bound and Upper Bound Theorems

In plasticity, there are two important bound theorems to estimate the collapse load: lower bound and upper bound theorems. In lower bound theorem, a stress field satisfies equilibrium which leads to an estimate of the corresponding collapse load. In the upper bound analysis, the collapse load is calculated by the assumed velocity or displacement field.

3.2.1 Lower Bound Theorem

The concept of the lower bound theorem was illustrated by Calladine as: If any stress distribution throughout the structure can be found which is everywhere in equilibrium internally and balances certain external loads and at the same time does not violate the yield condition, those loads will be carried safely by the structure (Murff, 2006). In Figure 3.5(a), a structure system subjects a load w_i (one of the external forces) and u_i is the corresponding displacement. Considering a convex yield surface which plastic strain increment $\dot{\varepsilon}$ is always normal to (Figure 3.5(b)), the work done by corresponding (actual) stress field σ is definitely greater than or equal to that by any other postulated stress field σ^*:

$$E = \sum w_i u_i = \int_v \sigma \dot{\varepsilon} dv \geq E^* = \int_v \sigma^* \dot{\varepsilon} dv = \sum w_i^* u_i \tag{3.9}$$

where w_i^* = Corresponding force of the postulated stress field σ^*

It is obvious that, from equation 3.9, the actual load w_i is also greater than or equal to the load w_i^* estimated from the postulated stress field σ^*, i.e., the collapse load estimated

from lower bound theorem is a conservative solution because it is either lower or equal to the actual collapse load.

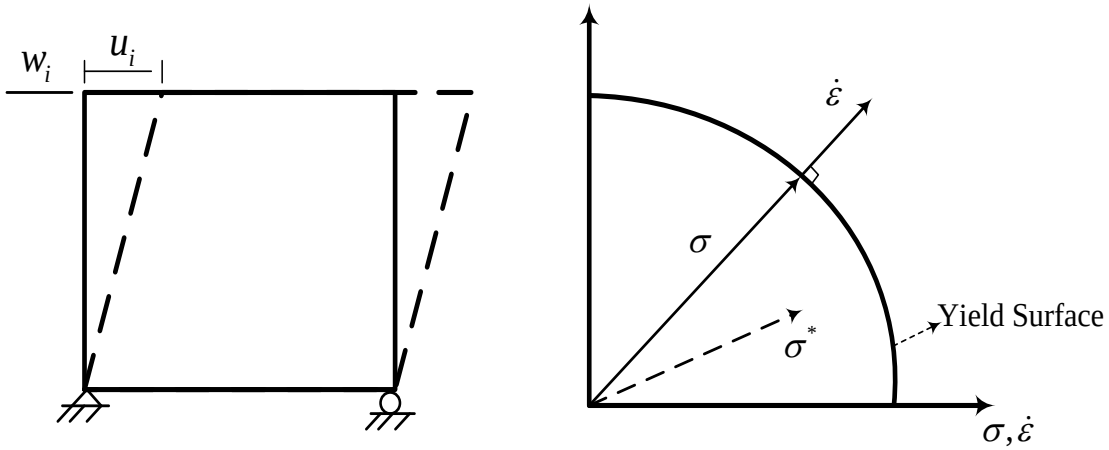

(a) Structure System (b) Stress Space System

Figure 3.5 Collapse load estimated by lower bound theorem

3.2.2 Upper Bound Theorem

The concept of the upper bound theorem was illustrated by Calladine as: If an estimated of the plastic collapse load of a body is made by equating internal rate of energy dissipation to the rate at which external forces do work in any postulated mechanism of deformation of the body, the estimated collapse load will be either high or correct (Murff, 2006). Let w_i^* are the loads estimated by equating external work to the internal energy dissipation $\dot{D}^*$ in the postulated velocity mechanism (Figure 3.6), by the principle of the virtual work:

$$\sum w_i^* u_i^* = \int_v \dot{D}^* dv = \int_v \sigma^* \dot{\varepsilon}^* dv \geq \int_v \sigma \dot{\varepsilon}^* dv = \sum w_i u_i^* \tag{3.10}$$

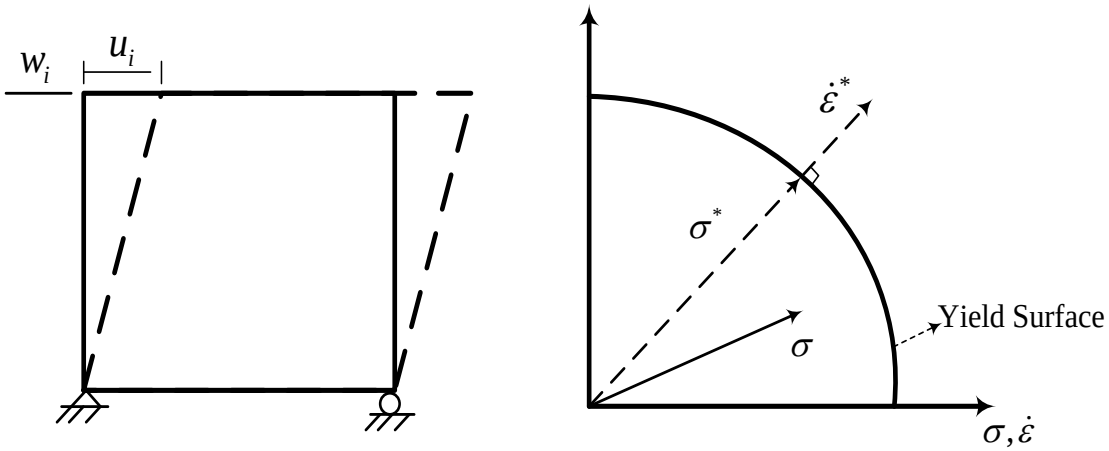

(a) Structure System (b) Stress Space System

Figure 3.6 Collapse load estimated by upper bound theorem

Equation 3.10 presents the plastic collapse load estimated from postulated velocity field w_i^* is either greater than or equal to actual load w_i. In application of upper bound theorem, the internal energy dissipation $\dot{D}^*$ could be estimated by the following with invoking Equation 3.8 to obtain the following equation:

$$\dot{D}^* = \underset{\sim}{\sigma}^* \dot{\underset{\sim}{\varepsilon}}^* = \sigma_{ij} \dot{\varepsilon}_{ij}^p = \sigma_{ij} \left[\dot{\Lambda} \frac{\partial F}{\partial \sigma_{ij}} \right] = \dot{\Lambda} \sigma_{ij} \frac{\partial F}{\partial \sigma_{ij}} \tag{3.11}$$

It is obvious that the internal energy dissipation $\dot{D}^*$ varies with different yield functions for which the associated flow rule is applicable. For example, consider a yield function for plane strain problem:

$$f = \left[\frac{\left(\sigma_x - \sigma_y\right)^2}{4} + \frac{1}{2}\left(\tau_{xy}^2 + \tau_{yx}^2\right) \right]^{1/2} - S_u = 0 \tag{3.12}$$

The above equation illustrates the soil element subjecting normal stress σ_x and σ_y and shear stress τ_{xy} and τ_{yx}; while the maximum shear stress equals the undrained shear strength S_u, the stress state is exactly on the yield surface. The dissipation of internal energy can be estimated by differentiating the yield function to each stress component and then substituted into Equation 3.11. For undrained analysis (no volume strain change), the energy dissipation function per unit volume is (Murff, 2006):

$$\dot{D}^* = 2S_u \left(\dot{\varepsilon}_x^2 + \dot{\varepsilon}_{xy}^2 \right) \tag{3.13}$$

where $\dot{\varepsilon}_x$ and $\dot{\varepsilon}_{xy}$ are the strain increments corresponding to σ_x and τ_{xy}.

For analyzing three dimensional problems, both Tresca (Equation 3.3) and Von Mises yield (Equation 3.5) functions are widely employed. The corresponding energy dissipation function for these two yield criterion are:

$$\dot{D}^* = 2S_u \left| \dot{\varepsilon}_{shear} \right|_{\max} = S_u \left| \dot{\gamma} \right|_{\max} \text{ ..... Tresca Yield Criteria} \tag{3.14}$$

$$\dot{D}^* = S_u \left(2\dot{\varepsilon}_{ij} \dot{\varepsilon}_{ij} \right)^{1/2} \text{ ..... Von Mises Yield Criteria} \tag{3.15}$$

It should be noted that only the maximum shear strain affects the internal energy dissipation in Tresca yield criteria. $\left| \dot{\gamma} \right|_{\max}$ is the maximum shear strain in engineering and twice of the strain tensor.

3.2.2.1 Energy Dissipation along Slip Surfaces

Consider a deformable region sandwiched between two rigid blocks (Figure 3.7), the lower rigid block is stationary but the upper one moves along x-direction with a central velocity v_0. The velocity fields of the deformable region are:

$$v_x = \frac{v_0}{t} y \qquad v_y = 0 \qquad v_z = 0 \tag{3.16}$$

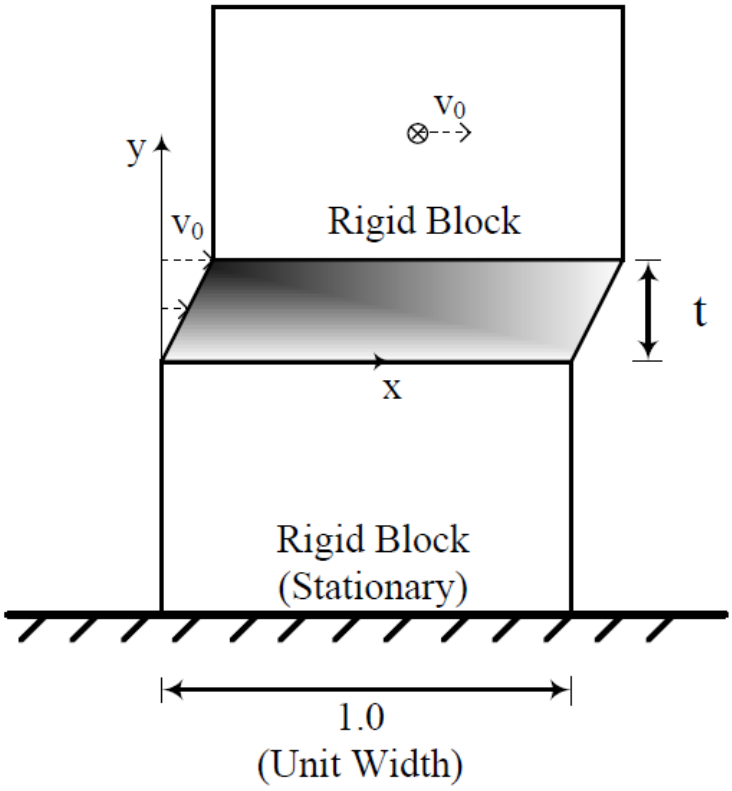

Figure 3.7 Energy dissipation of a deformable region (Murff, 2006)

The only non-zero strain components $\dot{\varepsilon}_{xy}$ and $\dot{\varepsilon}_{yx}$ can be calculated:

$$\dot{\varepsilon}_{xy} = \dot{\varepsilon}_{yx} = \frac{1}{2}\left(\frac{\partial v_x}{\partial y} + \frac{\partial v_y}{\partial x}\right) = \frac{v_0}{2t} \tag{3.17}$$

By applying the Tresca yield criteria, the internal energy dissipation $\dot{D}$ per volume is:

$$\dot{D} = 2S_u \left|\dot{\varepsilon}_{shear}\right|_{\max} = 2S_u \left|\dot{\varepsilon}_{xy}\right| = 2S_u \frac{v_0}{2t} = \frac{S_u v_0}{t} \tag{3.18}$$

Then the total energy dissipation per unit area of the deformable region is:

$$\dot{D}_{total} = \int_v \dot{D} dv = \left(\dot{D}\right)_{avg} \times volume = \frac{S_u v_0}{t} \times \left(t \times 1\right) = \frac{S_u v_0}{t} t \tag{3.19}$$

While the thickness of the deformable region approaches to zero, this region becomes a slip surface between two blocks. The corresponding internal energy dissipation of this slip surface can be calculated as:

$$\dot{D}_{Slip\ Surface/Length} = \lim_{t \to 0} \dot{D}_{total} = \lim_{t \to 0} \frac{S_u v_0}{t} t = S_u v_0 \tag{3.20}$$

It is notable that the above equation shows the energy dissipation of unit area slip surface; therefore, the internal energy dissipation of overall slip surface is:

$$\dot{D}_{Slip\ Surface} = \dot{D}_{Slip\ Surface/Length} \times Length = S_u v_0 L \tag{3.21}$$

where L = the length of the slip surface.

3.3 Application of Soil Plasticity Theory

The above two sections illustrate the basic concepts of the plasticity theory and the bound theorems. Comparing with lower bound theorem, upper bound theorem is relatively easy to employ although their results are either higher or equal to the exact solutions. In addition, Tresca yield criterion is widely used to describe the undrained behavior of marine soils. This section will discuss the applications of them on determining the ultimate bearing capacities of offshore foundations.

3.3.1 Ultimate Normal-direction Bearing Capacity of Flukes in Uniform Soils

Consider a fluke with length L_f and thickness t subjecting the maximum normal force F_n in uniform soils with undrained shear strength S_u, the corresponding upper bound mechanism shown in Figure 3.8. Since this problem is symmetric about two axes, the

total internal energy dissipation is the four times of that of right-upper quarter which includes two slip surfaces ((1) and (2)) and deformable regions ((3) and (4)). Given the velocity V_0 corresponding to normal force F_n, the normal and tangential velocities on the slip surface (1) are:

$$v_n = v_0 \cos\alpha \qquad v_p = v_0 \sin\alpha \tag{3.22}$$

where α = Angle of rigid wedge

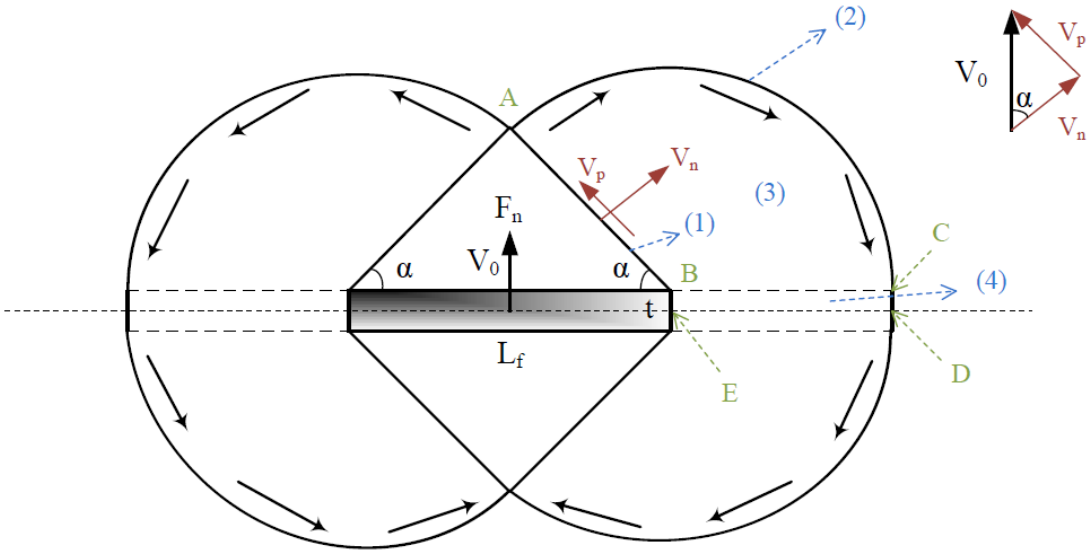

Figure 3.8 Upper bound mechanism of a fluke subjecting pure normal force

By means of Equation 3.21, the internal energy dissipation on slip surface (1) $\dot{D}_1$ can be computed:

$$\dot{D}_1 = S_u v_p L_1 = S_u v_0 \sin\alpha \frac{L_f/2}{\cos\alpha} = S_u v_0 L_f \left\{\frac{1}{2}\tan\alpha\right\} \tag{3.23}$$

Similarly, the internal energy dissipation on slip surface (2) $\dot{D}_2$ can be estimated:

$$\dot{D}_2 = S_u v_n L_2 = S_u v_0 \cos\alpha \left\{ \frac{L_f/2}{\cos\alpha} \times (\pi - \alpha) \right\} = S_u v_0 L_f \left\{ \frac{1}{2}(\pi - \alpha) \right\} \tag{3.24}$$

It should be noted that the length of slip surface (2) is the arc $\widehat{AC}$. According to Tresca yield criterion, the internal energy dissipation of deformable region (3) (fan-shaped zone ABC) could be computed by Equation 3.14:

$$\left|\dot{\gamma}\right|_{\max} = 2\left|\dot{\varepsilon}_{r\theta}\right| = 2\left|\frac{1}{2}\left(\frac{1}{r}\frac{\partial v_r}{\partial \theta} + \frac{\partial v_\theta}{\partial r} - \frac{v_\theta}{r}\right)\right| = \frac{v_n}{r} = \frac{v_0 \cos\alpha}{r} \tag{3.25}$$

$$\dot{D}_3 = \int_v S_u \left|\dot{\gamma}\right|_{\max} dv = \int_\alpha^\pi \int_0^{\frac{L_f}{2\cos\alpha}} S_u \frac{v_0 \cos\alpha}{r} r dr d\theta = S_u v_0 \cos\alpha \frac{L_f}{2\cos\alpha}(\pi - \alpha) = S_u v_0 L_f \left\{ \frac{1}{2}(\pi - \alpha) \right\} \tag{3.26}$$

From Figure 3.9, the relative velocity field of the rectangular region BCDE (region (4)) is:

$$v_x = 0 \qquad v_y = v_0 \cos\alpha \tag{3.27}$$

Since the whole region moves downward with a uniform velocity field, the energy dissipation only exists on slip surface $\overline{CD}$ and the interface $\overline{BE}$. One may assume the friction between the fluke and soil as follows:

$$f_s = a_d S_u = \frac{1}{s_t} S_u \tag{3.28}$$

where s_t = soil sensitivity

a_d = adhesion factor = reciprocal of the soil sensitivity

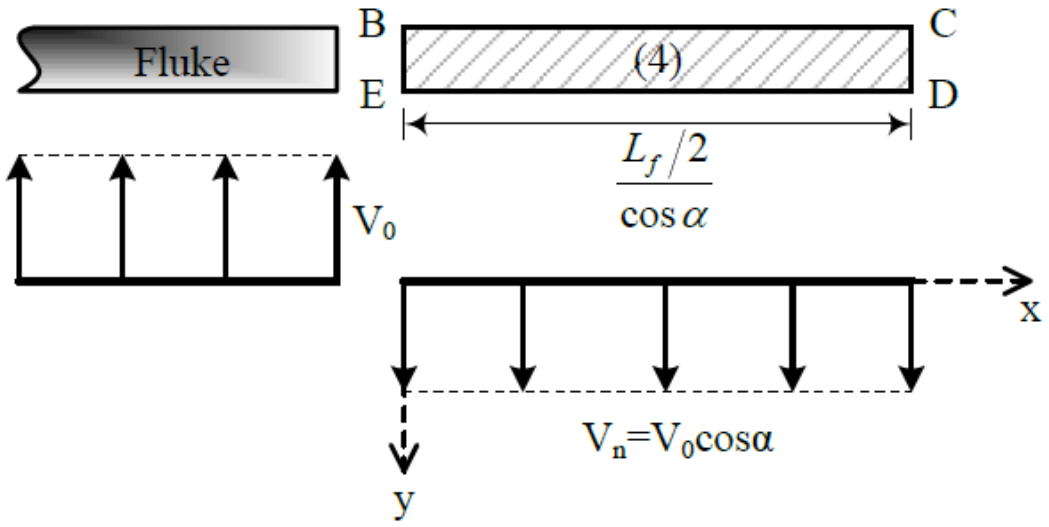

Figure 3.9 Velocity fields of the region BCDE and fluke

The energy dissipation on these two surfaces is:

$$\begin{aligned}\dot{D}_4 &= \dot{D}_{\overline{CD}} + \dot{D}_{\overline{BE}} = S_u v_n \frac{t}{2} + a_d S_u v_r \frac{t}{2} \\ &= S_u v_0 \cos\alpha \frac{t}{2} + a_d S_u v_0 (1+\cos\alpha)\frac{t}{2} \\ &= S_u v_0 L_f \left\{ \frac{t}{2L_f}\left[a_d + (1+a_d)\cos\alpha \right] \right\}\end{aligned} \tag{3.29}$$

It is notable that the relative velocity v_r on the interface $\overline{BE}$ is $v_0(1+\cos\alpha)$. The external work done by normal force F_n equates the total internal energy dissipation:

$$\begin{aligned}\dot{w}_E &= F_n v_0 = 4\left\{\dot{D}_1 + \dot{D}_2 + \dot{D}_3 + \dot{D}_4\right\} \\ &= 4S_u v_0 L_f \left\{ \frac{1}{2}\tan\alpha + \frac{1}{2}(\pi-\alpha) + \frac{1}{2}(\pi-\alpha) + \frac{t}{2L_f}\left[a_d + (1+a_d)\cos\alpha \right] \right\} \\ &= 4S_u v_0 L_f \left\{ \left[(\pi-\alpha) + \frac{\tan\alpha}{2} \right] + \frac{t}{2L_f}\left[a_d + (1+a_d)\cos\alpha \right] \right\}\end{aligned} \tag{3.30}$$

The normal force F_n can be estimated from above equation:

$$F_n = 4S_u L_f \left\{ \left[(\pi - \alpha) + \frac{\tan\alpha}{2} \right] + \frac{t}{2L_f} \left[a_d + (1 + a_d)\cos\alpha \right] \right\} \tag{3.31}$$

The normal dimensionless bearing factor N_{nmax} is defined as the normal force divided by the fluke length L_f and undrained shear strength S_u and presented in followings:

$$N_{n\max} = \frac{F_n}{S_u L_f} = 4\left\{ \left[(\pi - \alpha) + \frac{\tan\alpha}{2} \right] + \frac{t}{2L_f} \left[a_d + (1 + a_d)\cos\alpha \right] \right\} \tag{3.32}$$

While the interface between the fluke and soils is perfectly rough (a_d = 1), above equation is identical with the formula suggested by Bransby and O'Neill (2003). In addition, it matches the close form solution recommended by Andersen et al. (2003) while the wedge angle α equals to π/4. It is notable that the bearing factor is the function of the wedge angle so the critical value of the bearing factor occurs at the condition:

$$\begin{aligned} &\frac{dN_{n\max}}{d\alpha} = -4 + 2\sec^2\alpha_{cri} - \frac{2L_f}{t}(1 + a_d)\sin\alpha_{cri} = 0 \\ &\Rightarrow \sin^3\alpha_{cri} + \frac{2L_f}{t(1 + a_d)}\sin^2\alpha_{cri} - \sin\alpha_{cri} - \frac{L_f}{t(1 + a_d)} = 0 \end{aligned} \tag{3.33}$$

Figure 3.10 shows the normal direction bearing factor changing with the ratio R (for most of flukes, $7 \le R = \frac{L_f}{t} \le 20$) for different adhesion soils. The solid curves are the solutions which the critical wedge angle is determined from Equation 3.33 and then substituted into Equation 3.32; whereas, the dash curves are the results from Andersen's equation. Although the more rigorous solutions ($\alpha = \alpha_{cri}$) are more accurate and lower than the simplified solutions ($\alpha = 45^0$), it seems the difference between two solutions is

small. Figure 3.11 shows how the wedge angle changes with the aspect ratio and adhesion factor.

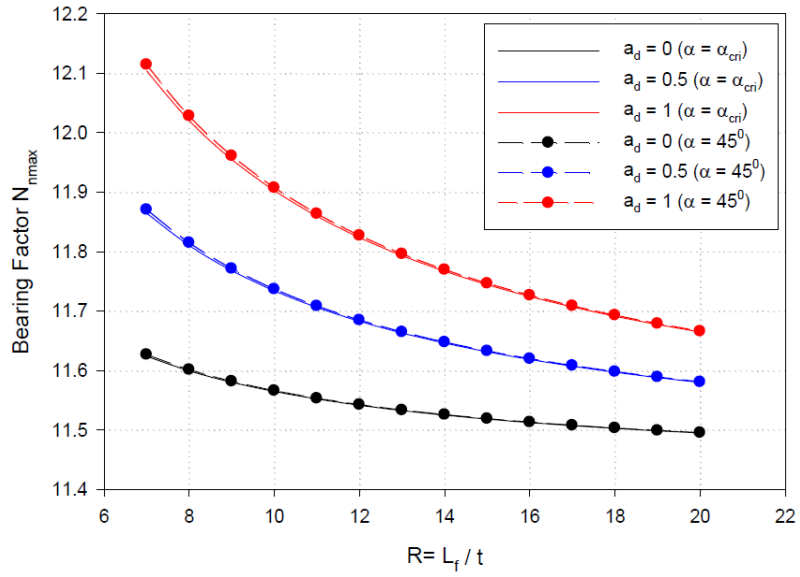

Figure 3.10 Normal direction bearing factor N_{nmax} for different adhesion cohesive soils

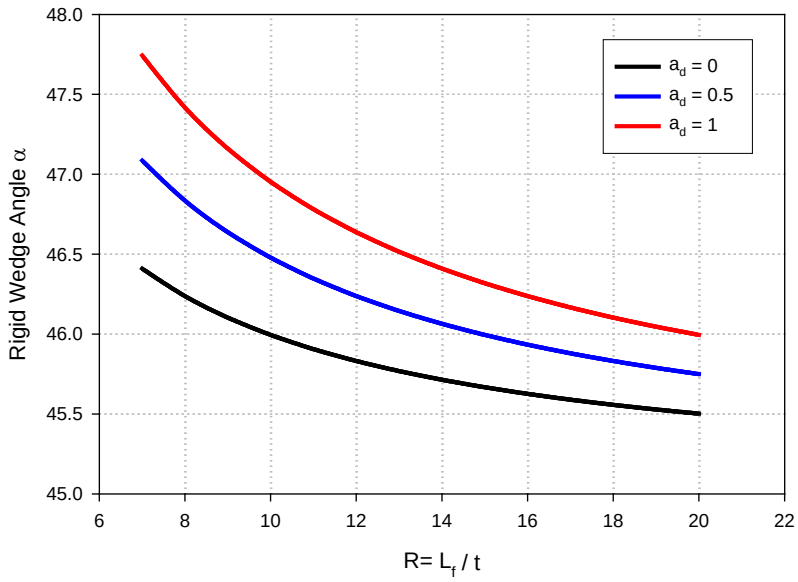

Figure 3.11 Rigid wedge angle change for different adhesion cohesive soils

3.3.2 Ultimate Tangential-direction Bearing Capacity of Flukes in Uniform Soils

The upper bound mechanism for subjecting pure tangential loading, shown in Figure 3.12, is similar to the normal load mechanism but in different directions. From Equation 3.31, the tangential force F_h can be estimated as following:

$$F_h = 4S_u t\left\{\left[\left(\pi-\alpha\right)+\frac{\tan\alpha}{2}\right]+\frac{L_f}{2t}\left[a_d+\left(1+a_d\right)\cos\alpha\right]\right\} \tag{3.34}$$

The tangential dimensionless bearing factor N_{smax} is defined as the tangential force divided by the fluke length L_f and undrained shear strength S_u and presented in followings:

$$N_{s\max}=\frac{F_h}{S_u L_f}=4\left\{\frac{t}{L_f}\left[\left(\pi-\alpha\right)+\frac{\tan\alpha}{2}\right]+\frac{1}{2}\left[a_d+\left(1+a_d\right)\cos\alpha\right]\right\} \tag{3.35}$$

Similarly, while the interface between the fluke and soils is perfectly rough (a_d = 1), above equation is identical with the formula suggested by Bransby and O'Neill (2003). Although this upper bound mechanism offers a theoretical way to approach the problem, the finite element analysis or laboratory test results show this upper bound mechanism may overestimate the ultimate capacity.

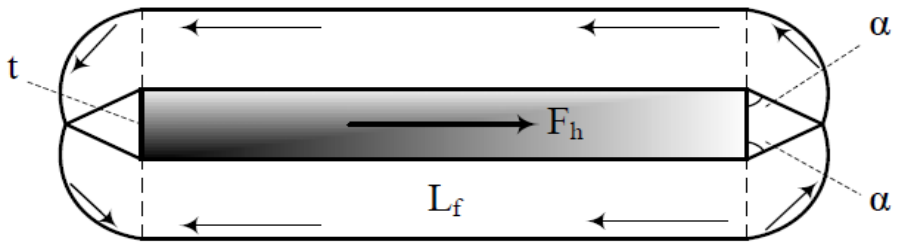

Figure 3.12 Upper bound mechanism of a fluke subjecting pure tangential force

3.3.3 Ultimate Moment Bearing Capacity of Flukes in Uniform Soils

The upper bound mechanism of the fluke subjecting pure moment (Figure 3.13) shows the internal energy dissipation only exists on the periphery of circular surface with the radius r:

$$r = \sqrt{\left(\frac{L_f}{2}\right)^2 + \left(\frac{t}{2}\right)^2} \tag{3.36}$$

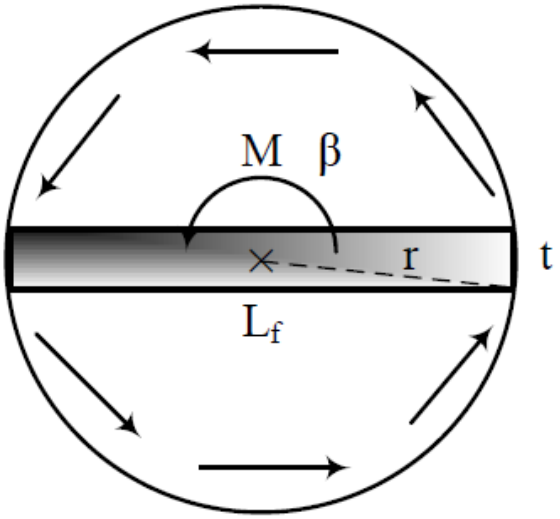

Figure 3.13 Upper bound mechanism of a fluke subjecting pure moment

Assuming the fluke rotates with angular velocity β_0, the velocity field along the circular slip surface:

$$v_0 = r\beta_0 \tag{3.37}$$

Therefore, the internal energy dissipation can be computed as following:

$$\begin{aligned} \dot{D} &= \int S_u v_0 ds = \int_0^{2\pi} S_u v_0 r d\theta = \int_0^{2\pi} S_u r \beta_0 r d\theta \\ &= 2\pi S_u r^2 \beta_0 \end{aligned} \tag{3.38}$$

The external work done by the moment M equates the total internal energy dissipation:

$$\begin{aligned}\dot{w}_E &= M\beta_0 = 2\pi S_u r^2 \beta_0 \\ &= 2\pi S_u \beta_0 \left[\left(\frac{L_f}{2} \right)^2 + \left(\frac{t}{2} \right)^2 \right] \\ &= \frac{\pi}{2} S_u \beta_0 L_f^2 \left[1 + \left(\frac{t}{L_f} \right)^2 \right]\end{aligned} \tag{3.39}$$

The moment M at the center of the fluke can be estimated from above equation:

$$M = \frac{\pi}{2} S_u L_f^2 \left[1 + \left(\frac{t}{L_f} \right)^2 \right] \tag{3.40}$$

The dimensionless moment bearing factor N_{mmax} is defined as the moment divided by the square of fluke length L_f and undrained shear strength S_u and presented in followings:

$$N_{m\max} = \frac{M}{S_u L_f^2} = \frac{\pi}{2} \left[1 + \left(\frac{t}{L_f} \right)^2 \right] \tag{3.41}$$

3.3.4 Ultimate Moment Bearing Capacity of Rectangular Flukes in Uniform Soils

Above section discusses a moment load acting on the center of the fluke under the plane strain condition; now, consider a rectangular plate with length L_f and width w_f undertakes a moment in uniform cohesive soils. The corresponding upper bound mechanism (Figure 3.14) shows the internal energy dissipates on the two top and side slip surfaces of a cylinder, which its axis (dash line) pass through the center of the fluke plate. Assume the fluke rotates with a central angular velocity β_0, the velocity field along the side surface of cylinder:

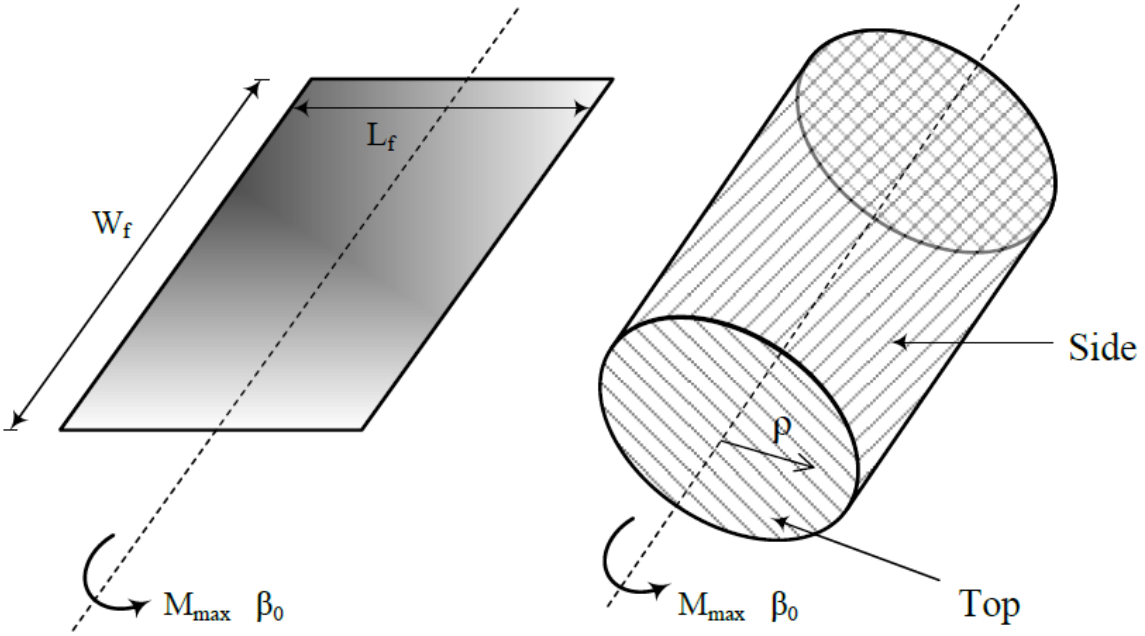

Figure 3.14 Upper bound mechanism of a rectangular fluke subjecting pure moment

$$v_s = \frac{L_f}{2}\beta_0 \tag{3.42}$$

Therefore, the internal energy dissipation on it can be computed as following:

$$\begin{aligned} \dot{D}_{side} &= \int S_u v_s dA \\ &= S_u v_s A = S_u \frac{L_f}{2}\beta_0 \left(\pi L_f\right) w_f = S_u \beta_0 \left(L_f w_f\right) L_f \left[\frac{\pi}{2}\right] \\ &= S_u \beta_0 A_f L_f \left[\frac{\pi}{2}\right] \end{aligned} \tag{3.43}$$

where A_f = Area of the fluke

Then, the velocity field on the two identical top surfaces of cylinder is:

$$v_t = \rho\beta_0 \tag{3.44}$$

Where ρ = Radial distance on the top surface

The internal energy dissipation on it can be computed as following:

$$\begin{aligned}\dot{D}_{top} &= \int S_u v_t dA = \int_0^{2\pi}\int_0^{L_f/2} S_u \rho\beta_0 \left(\rho d\,\rho d\theta\right) \\ &= S_u\beta_0\left(\frac{L_f^3}{24}\right)2\pi \\ &= S_u\beta_0 A_f L_f\left[\frac{\pi}{12}\frac{L_f}{w_f}\right]\end{aligned} \tag{3.45}$$

The external work done by the moment M equates the total internal energy dissipation:

$$\begin{aligned}\dot{w}_E &= M\beta_0 = \dot{D}_{side} + 2\dot{D}_{top} \\ &= S_u\beta_0 A_f L_f\left[\frac{\pi}{2}\right] + 2S_u\beta_0 A_f L_f\left[\frac{\pi}{12}\frac{L_f}{w_f}\right] \\ &= S_u\beta_0 A_f L_f\left[\frac{\pi}{2}\left(1+\frac{L_f}{3w_f}\right)\right]\end{aligned} \tag{3.46}$$

The moment M at the center of the fluke can be estimated from above equation:

$$M = S_u A_f L_f\left[\frac{\pi}{2}\left(1+\frac{L_f}{3w_f}\right)\right] \tag{3.47}$$

The dimensionless moment bearing factor N_{mmax} is defined as the moment divided by the fluke length L_f, fluke area A_f, and undrained shear strength S_u:

$$N_{m\max} = \frac{M}{S_u A_f L_f} = \frac{\pi}{2}\left(1+\frac{L_f}{3w_f}\right) \tag{3.48}$$

For a common fluke aspect ratio, say $w_f = 2\ L_f$, the bearing factor is:

$$N_{m\max} = \frac{\pi}{2}\left(1+\frac{L_f}{3w_f}\right) = \frac{\pi}{2}\left(1+\frac{1}{3\times 2}\right) \approx 1.83 \tag{3.49}$$

According to the result of the finite element study by Yang et.al (2008), it is very close to the number (1.83) shown above.

The moment bearing factor for a finite thickness plate in uniform cohesive soils can be derived by the same procedures illustrated in the previous and current sections:

$$N_{m\max} = \frac{\pi}{2}\left[1+\left(\frac{t}{L_f}\right)^2\right]\left\{1+\frac{L_f}{3w_f}\sqrt{1+\left(\frac{t}{L_f}\right)^2}\right\} \tag{3.50}$$

This close form solution matches Equation 3.41 while the width of the plate approaches infinity; whereas, it turns out to be Equation 3.48 for a vanishing thickness plate.

3.3.5 Ultimate Torsional Bearing Capacity of Very Thin Rectangular Flukes in Uniform Soils

When the anchor is subjected to the out-of-plane loads, such as a partially failed mooring system, torsion may occur. An upper bound mechanism for torsion (Figure 3.15) shows that the internal energy dissipates only on the top and bottom interfaces, since the thickness of the plate is zero (Yang et. al, 2008). From symmetry about two axes, the total internal energy dissipation is four times of the energy of a quarter plate dissipating:

$$\dot{D}_{total} = \dot{D}_{top} + \dot{D}_{bottom} = 2\times 4\left[\dot{D}_{(1)} + \dot{D}_{(2)}\right] \tag{3.51}$$

The angle ψ in region (1) is:

$$\tan\psi = {w_f}\Big/{L_f} = R_{wL} \tag{3.52}$$

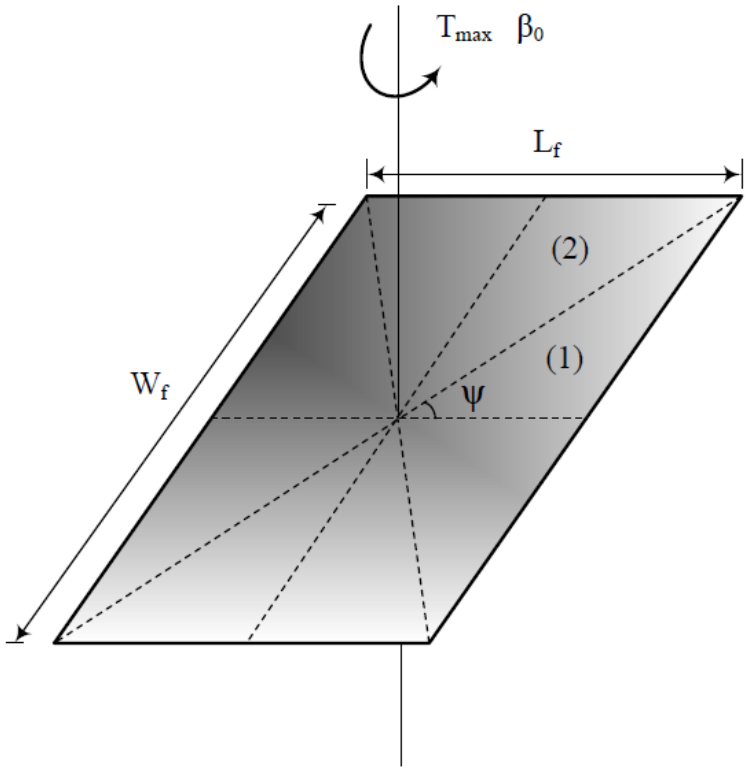

Figure 3.15 Upper bound mechanism of a thin rectangular fluke subjecting pure torsion

Assuming the fluke rotates about its center with angular velocity β_0, the velocity field in the region (1) can be estimated by $v_0 = r\beta_0$, where r is the distance to the axis. Hence, the internal energy dissipation in this zone:

$$\begin{aligned}
\dot{D}_{(1)} &= \int S_u v_0 dA = \int S_u r\beta_0 (rd\theta) dr = \int_0^{\psi}\int_0^{L_f \sec\theta/2} S_u r^2 \beta_0 dr d\theta \\
&= S_u\beta_0 \int_0^{\psi} \frac{1}{3}\left(\frac{L_f}{2}\right)^3 \sec^3\theta d\theta \\
&= S_u\beta_0 \frac{L_f^3}{24}\frac{1}{2}\left[\ln\left|\sec\psi + \tan\psi\right| + \sec\psi\tan\psi\right] \\
&= S_u\beta_0 \frac{L_f^3}{48}\left[\ln\left|\frac{\sqrt{L_f^2 + w_f^2}}{L_f} + \frac{w_f}{L_f}\right| + \frac{w_f\sqrt{L_f^2 + w_f^2}}{L_f^2}\right]
\end{aligned} \tag{3.53}$$

By substituting Equation 3.52 into above formula, the internal energy dissipation can be presented as following:

$$\dot{D}_{(1)} = S_u \beta_0 \frac{L_f^3}{48}\left[\ln\left|\sqrt{1+R_{wL}^2} + R_{wL}\right| + R_{wL}\sqrt{1+R_{wL}^2}\right] \tag{3.54}$$

The internal energy dissipation in region (2) could be calculated by the same derivation:

$$\begin{aligned}\dot{D}_{(2)} &= S_u \beta_0 \frac{w_f^3}{48}\left[\ln\left|\frac{\sqrt{w_f^2+L_f^2}}{w_f} + \frac{L_f}{w_f}\right| + \frac{L_f\sqrt{w_f^2+L_f^2}}{w_f^2}\right] \\ &= S_u \beta_0 \frac{L_f^3}{48} R_{wL}^3\left[\ln\left|\sqrt{1+R_{wL}^{-2}} + R_{wL}^{-1}\right| + R_{wL}^{-1}\sqrt{1+R_{wL}^{-2}}\right]\end{aligned} \tag{3.55}$$

Therefore, the total energy dissipation is:

$$\begin{aligned}\dot{D}_{total} &= 8\left[\dot{D}_{(1)} + \dot{D}_{(2)}\right] \\ &= S_u \beta_0 \frac{L_f^3}{6}\left\{\left[\ln\left|\sqrt{1+R_{wL}^2} + R_{wL}\right| + R_{wL}\sqrt{1+R_{wL}^2}\right] + \right. \\ &\quad \left. R_{wL}^3\left[\ln\left|\sqrt{1+R_{wL}^{-2}} + R_{wL}^{-1}\right| + R_{wL}^{-1}\sqrt{1+R_{wL}^{-2}}\right]\right\}\end{aligned} \tag{3.56}$$

The external work done by the torsion T equates the total internal energy dissipation:

$$\begin{aligned}\dot{w}_E &= T\beta_0 = \dot{D}_{total} \\ &= S_u \beta_0 \frac{L_f^3}{6}\left\{\left[\ln\left|\sqrt{1+R_{wL}^2} + R_{wL}\right| + R_{wL}\sqrt{1+R_{wL}^2}\right] + \right. \\ &\quad \left. R_{wL}^3\left[\ln\left|\sqrt{1+R_{wL}^{-2}} + R_{wL}^{-1}\right| + R_{wL}^{-1}\sqrt{1+R_{wL}^{-2}}\right]\right\}\end{aligned} \tag{3.57}$$

The torsion T at the center of the fluke can be estimated from above equation:

$$\begin{aligned}T = S_u \frac{L_f^3}{6}&\left\{\left[\ln\left|\sqrt{1+R_{wL}^2} + R_{wL}\right| + R_{wL}\sqrt{1+R_{wL}^2}\right] + \right. \\ &\left. R_{wL}^3\left[\ln\left|\sqrt{1+R_{wL}^{-2}} + R_{wL}^{-1}\right| + R_{wL}^{-1}\sqrt{1+R_{wL}^{-2}}\right]\right\}\end{aligned} \tag{3.58}$$

The dimensionless torsion bearing factor N_{tmax} is defined as the torsion divided by the fluke length L_f, fluke area A_f, and undrained shear strength S_u:

$$N_{t\max} = \frac{T}{S_u A_f L_f} = \frac{1}{6R_{wL}}\left\{\left[\ln\left|\sqrt{1+R_{wL}^2}+R_{wL}\right|+R_{wL}\sqrt{1+R_{wL}^2}\right]+ R_{wL}^3\left[\ln\left|\sqrt{1+R_{wL}^{-2}}+R_{wL}^{-1}\right|+R_{wL}^{-1}\sqrt{1+R_{wL}^{-2}}\right]\right\} \tag{3.59}$$

Considering the degree of roughness between the fluke and soils (Equation 3.28), the above formula could be modified as follows:

$$N_{t\max} = \frac{T}{S_u A_f L_f} = \frac{a_d}{6R_{wL}}\left\{\left[\ln\left|\sqrt{1+R_{wL}^2}+R_{wL}\right|+R_{wL}\sqrt{1+R_{wL}^2}\right]+ R_{wL}^3\left[\ln\left|\sqrt{1+R_{wL}^{-2}}+R_{wL}^{-1}\right|+R_{wL}^{-1}\sqrt{1+R_{wL}^{-2}}\right]\right\} \tag{3.61}$$

It is notable that Yang (2008) also suggested the close form solution of dimensionless torsion bearing factor for full rough foundation condition ($a_d = 1$) as:

$$N_{t\max} = \frac{w_f^2}{6L_f^2}\left\{\frac{\sin\theta}{\cos^2\theta}+\ln\left|\tan\left(\frac{\pi}{4}+\frac{\theta}{2}\right)\right|\right\}+\frac{L_f}{6w_f}\left\{\frac{\cos\theta}{\sin^2\theta}-\ln\left|\tan\left(\frac{\theta}{2}\right)\right|\right\} \tag{3.62}$$

where $\theta = \tan^{-1}\left(L_f \big/ w_f\right)$

Although two solutions look different apparently, the bearing factors calculated from these two formulae are identical. For example, N_{tmax} = 0.765 and N_{tmax} = 1.186 for aspect ratio R_{wL} = 1 and R_{wL} = 2, respectively.

Figure 3.16 illustrates how the dimensionless torsion and moment bearing factors vary over a range of aspect ratio R_{wL} = 1-5. Both the thickness and width effects are considered in the analysis (Equation 3.50). It seems that aspect ratio plays a more

important role in N_{mmax} than thickness effect does and both two curves do not vary too much while the aspect ratio is greater than 2. On the other hand, the torsion bearing factor curve (a_d = 1) increases dramatically and intersects the moment bearing factor curves at the aspect ratio R_{wL} = 3.2. The results also imply that the fluke has low resistance to twist (yaw, Figure 3.15) relative to rotation (pitch and roll, Figure 3.14) when the aspect ratio is less than 3.2. For adhesion factor a_d = 0.5 (S_t = 2), the torsion bearing factor is one half of that for full adhesion. Hence, it can be inferred that the anchor may adjust its orientation to follow the anchor line relatively easily during the out-of-plane load applying, especially in high sensitivity soils.

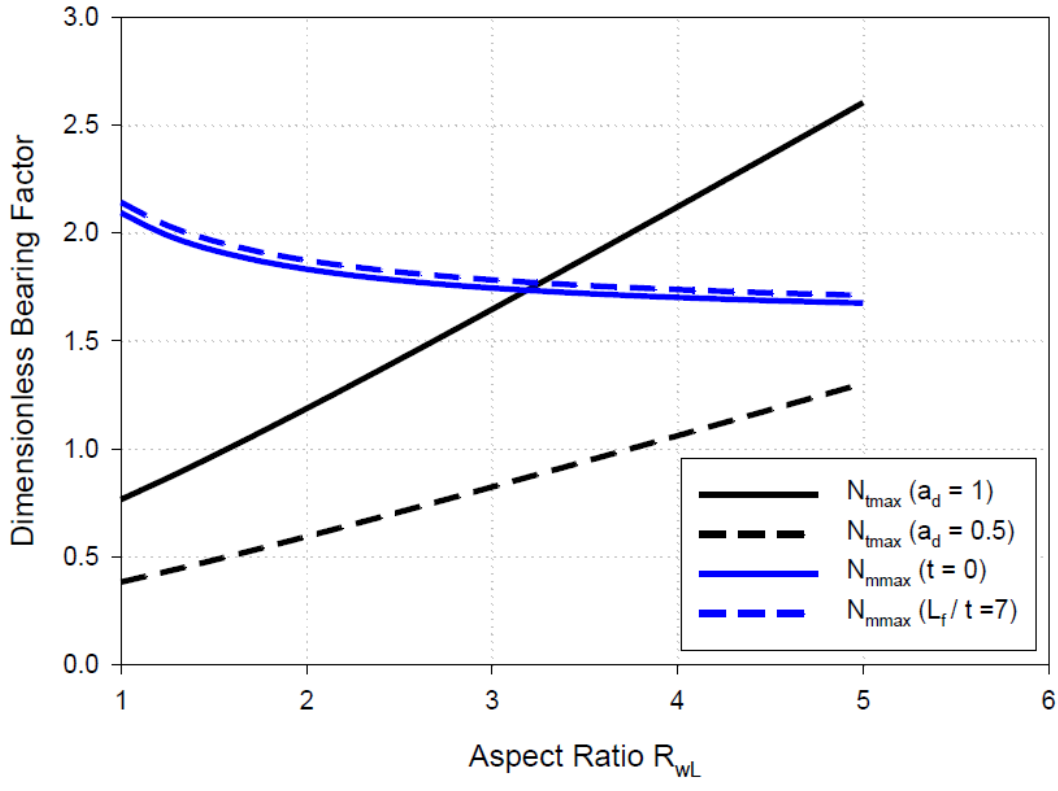

Figure 3.16 Dimensionless bearing factor for subjecting pure torsion or moment

3.3.6 Ultimate Bearing Capacities of Flukes in Non-uniform Soils

The previous sections discuss the dimensionless bearing factors of a rectangular plate subjecting pure vertical load, horizontal load, moment, or torsion in homogeneous and isotropic cohesive soils. Nevertheless, as mentioned in section 1.3.2, most of soils are not uniform but their strengths increase with the embedded depths (Equation 1.1). At the beginning of this section, the dimensionless normal-direction bearing factor will be reinvestigated based on the same upper bound mechanism but in non-uniform soils. Others could be derived by the similar concept.

Consider a very thin (thickness t = 0) fluke subjected to a normal force F_n oriented at an angle θ_f from horizontal in soil having a strength profile $S_u = S_{u0} + kz$. The corresponding velocity field of upper bound mechanism is shown in Figure3.17:

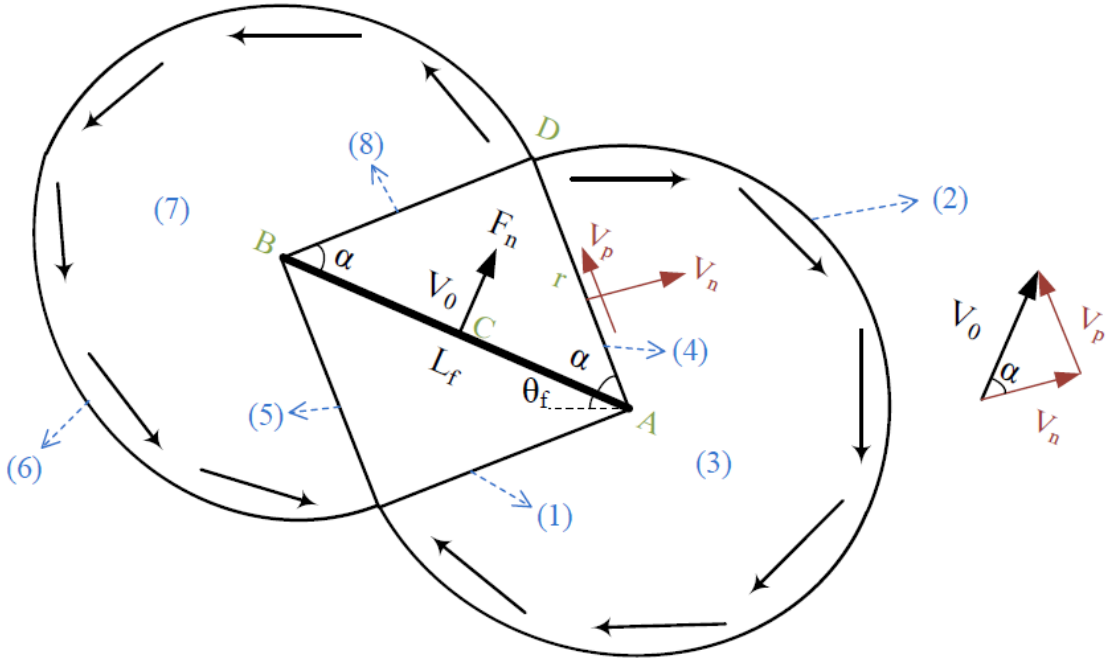

Figure 3.17 Upper bound mechanism of a thin fluke subjecting pure normal force

The mechanism can be divided into two parts which point A and B are the reference points of corresponding regions. In part A, the internal energy dissipation exists on the deformable zone (3) and slip surfaces (1), (2), and (4); whereas, it exists on the deformable zone (7) and slip surfaces (5), (6), and (8) in part B. Both the normal and tangential velocities (v_n & v_p) can be determined by Equation 3.22.

Part A

The undrained shear strength at point A is:

$$S_{uA} = S_{u0} + k\left(z_c + \frac{L_f}{2}\sin\theta_f \right) = S_{uc} + 0.5kL_f \sin\theta_f \tag{3.63}$$

where z_c = the depth of point c (center of the fluke)

Therefore, the internal energy dissipation along the slip surface (1) is:

$$\dot{D}_1 = \int_0^r \left[S_{uA} + ks\sin\left(\alpha - \theta_f\right) \right] v_p ds = v_p \left[S_{uA} r + \frac{1}{2} kr^2 \sin\left(\alpha - \theta_f\right) \right] \tag{3.64}$$

where r = $\dfrac{L_f/2}{\cos\alpha} = \overline{AD}$

Similarly, the internal energy dissipation along the slip surface (4) is:

$$\dot{D}_4 = \int_0^r \left[S_{uA} - ks\sin\left(\alpha + \theta_f\right) \right] v_p ds = v_p \left[S_{uA} r - \frac{1}{2} kr^2 \sin\left(\alpha + \theta_f\right) \right] \tag{3.65}$$

In addition, the internal energy dissipation along the slip surface (2) is:

$$\begin{aligned} \dot{D}_2 &= \int_{-(\pi-\alpha)-\theta_f}^{(\pi-\alpha)-\theta_f} \left[S_{uA} - r\sin\psi \right] v_n r d\psi = v_n r \left[S_{uA}\psi + r\cos\psi \right]_{-(\pi-\alpha)-\theta_f}^{(\pi-\alpha)-\theta_f} \\ &= v_n r \left\{ 2S_{uA}\left(\pi - \alpha\right) + r\left[\cos\left(\pi - \left(\alpha + \theta_f\right)\right) - \cos\left(\pi - \left(\alpha - \theta_f\right)\right) \right] \right\} \\ &= v_n r \left\{ 2S_{uA}\left(\pi - \alpha\right) + r\left[-\cos\left(\alpha + \theta_f\right) + \cos\left(\alpha - \theta_f\right) \right] \right\} \end{aligned} \tag{3.66}$$

Finally, the internal energy dissipation in the deformable region (3):

$$\dot{D}_3 = \int_v S_u \left|\dot{\gamma}\right|_{\max} dv$$

where $S_u = S_{uA} - \rho \sin\psi \qquad \left|\dot{\gamma}\right|_{\max} = 2\left|\dot{\varepsilon}_{r\theta}\right| = 2\left|\frac{1}{2}\left(\frac{1}{r}\frac{\partial u_r}{\partial \theta} + \frac{\partial u_\theta}{\partial r} - \frac{u_\theta}{r}\right)\right| = \frac{v_n}{r} = \frac{v_0 \cos\alpha}{r}$

$$\begin{aligned}
\dot{D}_3 &= \int_{-(\pi-\alpha)-\theta_f}^{(\pi-\alpha)-\theta_f} \int_0^r \left[S_{uA} - \rho \sin\psi\right] \frac{v_n}{\rho} \rho d\rho d\psi \\
&= v_n \int_{-(\pi-\alpha)-\theta_f}^{(\pi-\alpha)-\theta_f} \left[S_{uA} r - \frac{r^2}{2}\cos\psi \right] d\psi \\
&= v_n r \left[S_{uA} r\psi + \frac{r^2}{2}\cos\psi \right]\Bigg|_{-(\pi-\alpha)-\theta_f}^{(\pi-\alpha)-\theta_f} \\
&= v_n \left\{ 2S_{uA} r\left(\pi-\alpha\right) + \frac{r^2}{2}\left[\cos\left(\pi - \left(\alpha+\theta_f\right)\right) - \cos\left(\pi - \left(\alpha-\theta_f\right)\right)\right]\right\} \\
&= v_n \left\{ 2S_{uA} r\left(\pi-\alpha\right) + \frac{r^2}{2}\left[-\cos\left(\alpha+\theta_f\right) + \cos\left(\alpha-\theta_f\right)\right]\right\}
\end{aligned} \tag{3.67}$$

Part B

The undrained shear strength at point B is:

$$S_{uB} = S_{u0} + k\left(z_c - \frac{L_f}{2}\sin\theta_f \right) = S_{uc} - 0.5kL_f \sin\theta_f \tag{3.68}$$

Therefore, the internal energy dissipation along the slip surface (5) is:

$$\dot{D}_5 = \int_0^r \left[S_{uB} + ks\sin\left(\alpha+\theta_f\right)\right] v_p ds = v_p \left[S_{uB} r + \frac{1}{2}kr^2 \sin\left(\alpha+\theta_f\right)\right] \tag{3.69}$$

Similarly, the internal energy dissipation along the slip surface (8) is:

$$\dot{D}_8 = \int_0^r \left[S_{uB} - ks\sin\left(\alpha-\theta_f\right)\right] v_p ds = v_p \left[S_{uB} r - \frac{1}{2}kr^2 \sin\left(\alpha-\theta_f\right)\right] \tag{3.70}$$

In addition, the internal energy dissipation along the slip surface (6) is:

$$\begin{aligned}\dot{D}_6 &= \int_{(\alpha-\theta_f)}^{(\alpha-\theta_f)+2(\pi-\alpha)} \left[S_{uB} - r\sin\psi\right] v_n r\, d\psi = v_n r\left[S_{uB}\psi + r\cos\psi\right]_{(\alpha-\theta_f)}^{(\alpha-\theta_f)+2(\pi-\alpha)} \\ &= v_n r\left\{2S_{uB}\left(\pi-\alpha\right) + r\left[\cos\left(-\alpha-\theta_f\right) - \cos\left(\alpha-\theta_f\right)\right]\right\} \\ &= v_n r\left\{2S_{uA}\left(\pi-\alpha\right) + r\left[\cos\left(\alpha+\theta_f\right) - \cos\left(\alpha-\theta_f\right)\right]\right\}\end{aligned} \tag{3.71}$$

Finally, the internal energy dissipation in the deformable region (7):

$$\dot{D}_7 = \int_v S_u \left|\dot{\gamma}\right|_{\max} dv$$

where $S_u = S_{uA} - \rho\sin\psi \qquad \left|\dot{\gamma}\right|_{\max} = 2\left|\dot{\varepsilon}_{r\theta}\right| = 2\left|\frac{1}{2}\left(\frac{1}{r}\frac{\partial u_r}{\partial\theta} + \frac{\partial u_\theta}{\partial r} - \frac{u_\theta}{r}\right)\right| = \frac{v_n}{r} = \frac{v_0\cos\alpha}{r}$

$$\begin{aligned}\dot{D}_7 &= \int_{(\alpha-\theta_f)}^{(\alpha-\theta_f)+2(\pi-\alpha)} \int_0^r \left[S_{uB} - \rho\sin\psi\right]\frac{v_n}{\rho}\rho\, d\rho\, d\psi \\ &= v_n \int_{(\alpha-\theta_f)}^{(\alpha-\theta_f)+2(\pi-\alpha)} \left[S_{uB} r - \frac{r^2}{2}\cos\psi\right] d\psi \\ &= v_n r\left[S_{uB} r\psi + \frac{r^2}{2}\cos\psi\right]_{(\alpha-\theta_f)}^{(\alpha-\theta_f)+2(\pi-\alpha)} \\ &= v_n\left\{2S_{uB} r\left(\pi-\alpha\right) + \frac{r^2}{2}\left[\cos\left(-\alpha-\theta_f\right) - \cos\left(\alpha-\theta_f\right)\right]\right\} \\ &= v_n\left\{2S_{uB} r\left(\pi-\alpha\right) + \frac{r^2}{2}\left[\cos\left(\alpha+\theta_f\right) - \cos\left(\alpha-\theta_f\right)\right]\right\}\end{aligned} \tag{3.72}$$

The external work done by normal force F_n equates the total internal energy dissipation:

$$\begin{aligned}\dot{w}_E = F_n v_0 &= \dot{D}_1 + \dot{D}_2 + \dot{D}_3 + \dot{D}_4 + \dot{D}_5 + \dot{D}_6 + \dot{D}_7 + \dot{D}_8 \\ &= 2v_p r\left(S_{uA} + S_{uB}\right) + 4v_n r\left(\pi-\alpha\right)\left(S_{uA} + S_{uB}\right) \\ &= 4v_0\sin\alpha\frac{L_f/2}{\cos\alpha}S_{uc} + 8v_0\frac{L_f/2}{\cos\alpha}\left(\pi-\alpha\right)S_{uc}\cos\alpha \\ &= S_{uc} v_0 L_f\left\{4\left[\left(\pi-\alpha\right) + \frac{\tan\alpha}{2}\right]\right\}\end{aligned} \tag{3.73}$$

Note: $S_{uc} = \frac{1}{2}\left(S_{uA} + S_{uB}\right)$

The normal force F_n can be estimated from above equation:

$$F_n = S_{uc} L_f \left\{ 4 \left[\left(\pi - \alpha\right) + \frac{\tan\alpha}{2} \right] \right\} \tag{3.74}$$

The normal dimensionless bearing factor N_{nmax} can be defined as the normal force divided by the fluke length L_f and undrained shear strength at the center of the fluke S_{uc}:

$$N_{n\max} = \frac{F_n}{S_{uc} L_f} = 4 \left[\left(\pi - \alpha\right) + \frac{\tan\alpha}{2} \right] \tag{3.75}$$

Comparing with Equation 3.32, two equations will be identical when the adhesion factor $a_d = 1$ and thickness $t = 0$. A very important result is that all closed form solutions for dimensionless bearing factors in uniform soils can be employed directly in linear-increasing strength soils as long as the loads (includes forces, moment, and torsion) are normalized by the fluke center shear strength S_{uc} and corresponding geometric properties of the fluke.

Accordingly, the dimensionless bearing factors for pure normal force, horizontal force, moment, and torsion could be redefined as:

$$N_{n\max} = \frac{F_n}{S_{uc} L_f} = 4 \left\{ \left[\left(\pi - \alpha\right) + \frac{\tan\alpha}{2} \right] + \frac{t}{2L_f} \left[a_d + \left(1 + a_d\right)\cos\alpha \right] \right\} \tag{3.76}$$

$$N_{s\max} = \frac{F_h}{S_{uc} L_f} = 4 \left\{ \frac{t}{L_f} \left[\left(\pi - \alpha\right) + \frac{\tan\alpha}{2} \right] + \frac{1}{2} \left[a_d + \left(1 + a_d\right)\cos\alpha \right] \right\} \tag{3.77}$$

$$N_{m\max} = \frac{M}{S_{uc} A_f L_f} = \frac{\pi}{2}\left[1+\left(\frac{t}{L_f}\right)^2\right]\left\{1+\frac{L_f}{3w_f}\sqrt{1+\left(\frac{t}{L_f}\right)^2}\right\} \tag{3.78}$$

$$N_{t\max} = \frac{T}{S_{uc} A_f L_f} = \frac{a_d}{6R_{wL}}\left\{\left[\ln\left|\sqrt{1+R_{wL}^2}+R_{wL}\right|+R_{wL}\sqrt{1+R_{wL}^2}\right]+ R_{wL}^3\left[\ln\left|\sqrt{1+R_{wL}^{-2}}+R_{wL}^{-1}\right|+R_{wL}^{-1}\sqrt{1+R_{wL}^2}\right]\right\} \tag{3.79}$$

CHAPTER IV

MECHANICS OF DRAG EMBEDMENT ANCHORS SUBJECTING IN-PLANE LOADINGS

4.1 Research Tasks

The analysis presented herein focuses on an idealized anchor configuration comprising a rectangular fluke attached to a cylindrical shank, the intent being to elucidate the basic mechanics of DEA behavior with a widespread degree of generality to all anchors. It is, of course, recognized that geometric details unique to a given anchor can affect anchor performance which must be evaluated on an ad hoc basis. Analysis of DEA behavior comprises two tasks: (1) the anchor capacity at any given embedment depth and orientation, and (2) the trajectory of the anchor during drag embedment. Given that anchor load capacity typically increases with increasing embedment depth, realistic prediction of the latter is particularly important. This chapter addresses both aspects of anchor performance. The work presented advances the state of knowledge on this topic by considering the effects of different anchor geometries, soil sensitivity, and the chain angle at the soil surface. This chapter also presents an improved analysis method for allowing the chain angle to vary with embedment depth. The analysis is confined to fine-grained seabed soils for which undrained conditions are assumed to prevail during the drag embedment process.

Anchor chain tension and geometry in soil are also investigated in this research. Actually, the behavior of the anchor is strongly influenced by the chain during the

penetration and the resultant force at anchor must be equal to the padeye chain tension since they are connected at the shackle point. When the chain subjects the anchor to out-of-plane (lateral) loads due to the effects of hurricanes, the anchor attempts to travel following the direction of the resultant force applied on the chain but the soil resistances withstand the tendency of the whole anchor system. Therefore, what the work herein investigates an anchor system-soils interaction problem.

4.2 Anchor Capacity

Holding capacity is the primary task in the anchor research work. In chapter II, several researchers proposed analytical and empirical methods for estimated the holding capacity in soils. Empirical methods are based on calibration to each ad hoc case. They have the advantage that the implicitly account for the complex geometry of actual anchors. However, it is difficult to extrapolate empirical data to other anchor geometries and soil conditions. The following research works are based on a regular anchor shape (rectangular) model combined with the plasticity theory presented in previous chapter to investigate the behavior and capacity of the anchor. The aim of the study is to understand the basic mechanics of drag anchors, recognizing that the influence of complex anchor geometry must be evaluated in future analytical or experimental studies.

4.2.1 Analysis Model

The analysis considers an anchor (Figure 4.1) having a fluke length L_f, a shank length L_s, a fluke-shank attachment point distance L_j, and a fluke-shank angle θ_{fs}. The anchor line exerts a force F oriented at an angle θ_a from horizontal. The shank is oriented at an angle θ_s from horizontal, and $\theta_{as} = \theta_a - \theta_s$ is defined as the angle of the

anchor line force F relative to the orientation of the shank. Initial consideration is given to a thin shank, $D_s \approx 0$, such that no soil resistance force is mobilized by the shank.

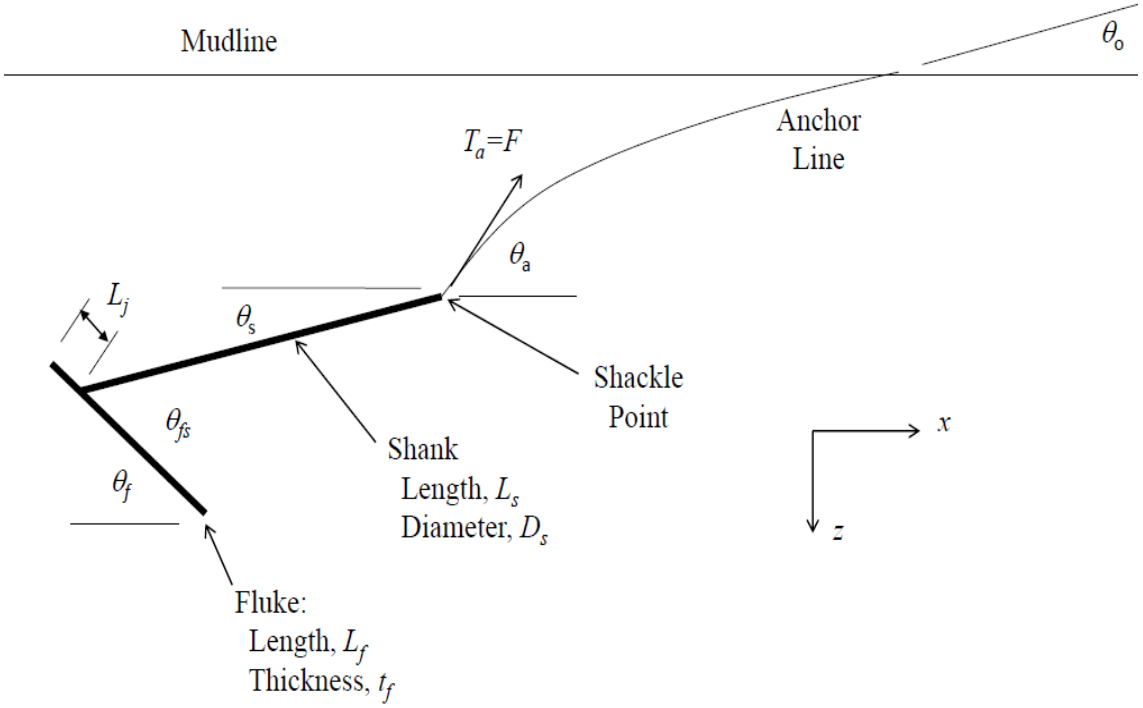

Figure 4.1 Anchor definition sketch

Figure 4.2 shows the equivalent forces and moments acting on the center of the fluke. The tangential and normal forces as well as the resultant moment are as follows:

$$F_n = F \sin(\theta_{fs} + \theta_{as}) = F\, c_1 \tag{4.1}$$

$$F_t = F \cos(\theta_{fs} + \theta_{as}) = F\, c_2 \tag{4.2}$$

$$M = FL_f \left\{ \sin(\theta_{fs} + \theta_{as})\left[\frac{L_j}{L_f} + \frac{L_s}{L_f}\cos\theta_{fs} - \frac{1}{2}\right] - \cos(\theta_{fs} + \theta_{as})\sin\theta_{fs}\,\frac{L_s}{L_f}\right\} = FL_f c_3 \tag{4.3}$$

The subscripts *n* and *t* will denote directions normal and tangential to the surface of the fluke. The moment *M* in Equation 4.3 is in reference to the centroid of the fluke. The anchor line angle relative to the shank, θ_{as}, will in general vary throughout the various stages of loading. Therefore an essential first step is to define how anchor capacity *F* varies with variation in θ_{as}, a relationship that will be termed the anchor capacity curve.

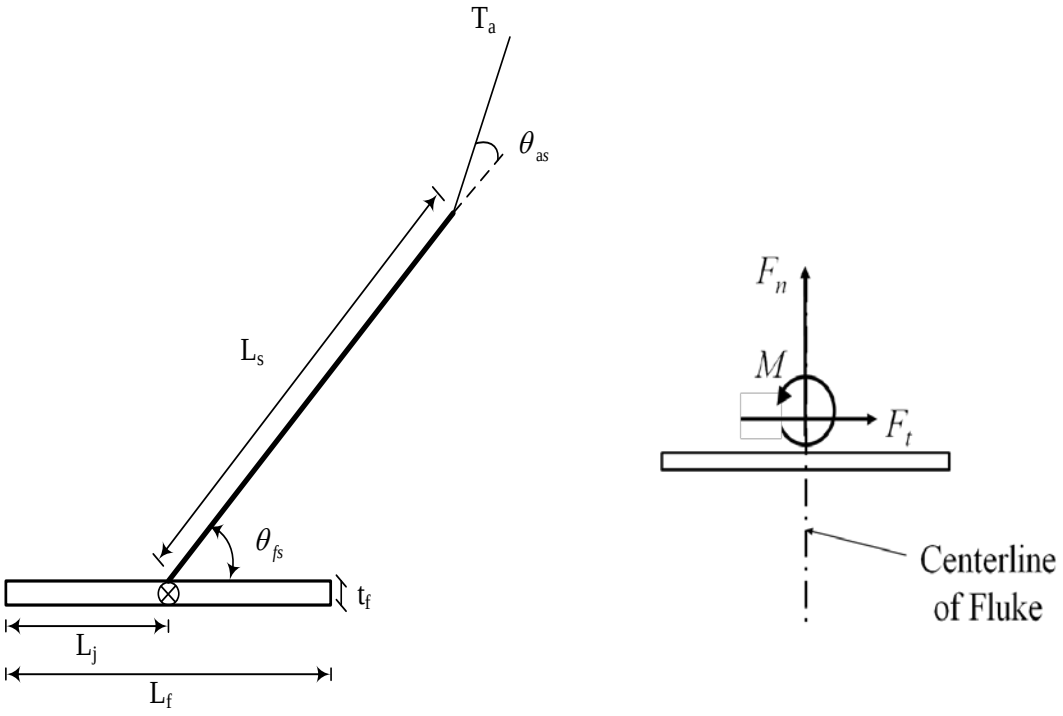

Figure 4.2 Equivalent forces and mement acting on fluke

Normalizing all terms by soil strength and fluke length leads to the following more convenient expressions for dimensionless anchor capacity N_e in terms of dimensionless resistance for pure normal, tangential and moment loading, N_p, N_s, and N_m, respectively:

$$N_e = F / S_u A_f \tag{4.4}$$

$$N_n = F_n / S_u A_f = N_e c_1 \tag{4.5}$$

$$N_t = F_t / S_u A_f = N_e c_2 \tag{4.6}$$

$$N_m = M / S_u A_f L_f = N_e c_3 \tag{4.7}$$

where $A_f = L_f w_f$ is the fluke area for a fluke of width w_f and s_u is the soil undrained shear strength. The maximum values of these bearing factors, N_{nmax}, N_{tmax}, and N_{mmax}, occur under conditions of pure normal, tangential, and rotational loading, respectively. The upper bound limit analysis solutions Equation 3.76 and 3.78 are employed to calculate the ultimate dimensionless normal and moment bearing factors with the assumptions rigid wedge angle α equals to π/4 and the width effect is neglected ($w_f \to \infty$, plane strain problem):

$$N_{n\max} = \frac{F_n}{S_{uc} L_f} = 3\pi + 2 + \frac{t_f}{L_f}\left(a_d + \frac{1+a_d}{\sqrt{2}}\right) \tag{4.8}$$

$$N_{m\max} = \frac{M}{S_{uc} A_f L_f} = \frac{\pi}{2}\left[1 + \left(\frac{t_f}{L_f}\right)^2\right] \tag{4.9}$$

The tangential bearing factor suggested by Andersen et al. (2003) is used in the analysis due to the overestimation of the horizontal upper bound solution:

$$N_{t\max} = 2\left(\alpha + N_{tip}\frac{t_f}{L_f}\right) \approx 2\alpha + 15\frac{t_f}{L_f} \tag{4.10}$$

It should be noted that the above formula is based on friction (Equation 3.28) on the upper and lower interface of the fluke, and the bearing capacity of N_cS_u at both end of the plate in deep soil (N_c = 7.5 for plane strain problem). Murff et al. (2005) present comparisons of the O'Neill solutions to finite element (FE) solutions for a plate aspect

ratio $L_f/t_f = 7$ over a range of adhesion values a_d varying from 0 to 1, as well as for $L_f/t_f = 20$ for a fully rough plate. The overall agreement is good between the FE solutions and Equation 4.8 to 4.10. For normal loads, Eq. 8 tends to exceed the FE estimates by 3-4%. For moment loading, the greatest discrepancy between FE solutions and Eq. 10 is about 9% for a fully rough plate.

4.2.2 Non-interactive Behavior

The first model considered assumes no interaction between the three load components; e.g., ultimate moment capacity is unaffected by the magnitudes of the normal and tangential components of loading, etc. Although a simplification of actual behavior, analysis of the anchor in terms of three clearly defined collapse mechanisms facilitates a conceptual understanding of drag anchor behavior and provides a preliminary assessment of anticipated anchor behavior. In the non-interactive case, the load capacity for the anchor will be the least of the following three collapse loads:

Normal Mechanism: $N_{en} = N_{n\max} / |c_1|$ (4.11)

Tangential Mechanism: $N_{et} = N_{t\max} / |c_2|$ (4.12)

Rotational Mechanism: $N_{em} = N_{m\max} / |c_3|$ (4.13)

Figure 4.3 shows a plot of N_e versus θ_{as} for a base case analysis (Table 4.1), $L_s/L_f = 1.5$, $L_j/L_f = 0.25 = 0$, $L_f/t_f = 7$, and $\theta_{fs} = 50^o$. Examination of c_1 and c_2 in Equations 4.11 and 4.12 show N_{en} and N_{et} to be simple multiples of the cosecant and secant functions, $\csc(\theta_{fs} + \theta_{as})$ and $\sec(\theta_{fs} + \theta_{as})$, respectively. A singularity occurs in the rotational collapse load function when the line of action of the resultant force F passes through the fluke

centroid. The right side of the singularity corresponds to a forward (counter-clockwise) rotation and vice-versa. The solid curve in Figure 4.3 shows the controlling capacity curve for the anchor. In the region where rotational capacity tends to infinity, a translational mechanism replaces rotation as the critical collapse mechanism.

Table 4.1 Base case condition for anchor capacity and trajectory predictions

Anchor Properties:
Fluke Length, L_f = 2 m Shank Length, L_s = 3 m Junction Point, L_j = 0.5 m Fluke-Shank Angle, θ_{fs} = 50 degrees Fluke Width, w_f = 3 m Fluke Thickness, t_f = 0.28 m
Anchor Line Properties:
Line Diameter, b = 0.073 m Bearing Factor, N_c = 12 Multiplier, E_n = 1 (wire line) Weight per Unit Length, ρ = 0.28 kN/m Tangential-Frictional Resistance, μ = 0.4
Seabed Properties:
Mudline Strength, s_{u0} = 2 Strength Gradient, k = 1.57 kPa/m Sensitivity, S_t = 3

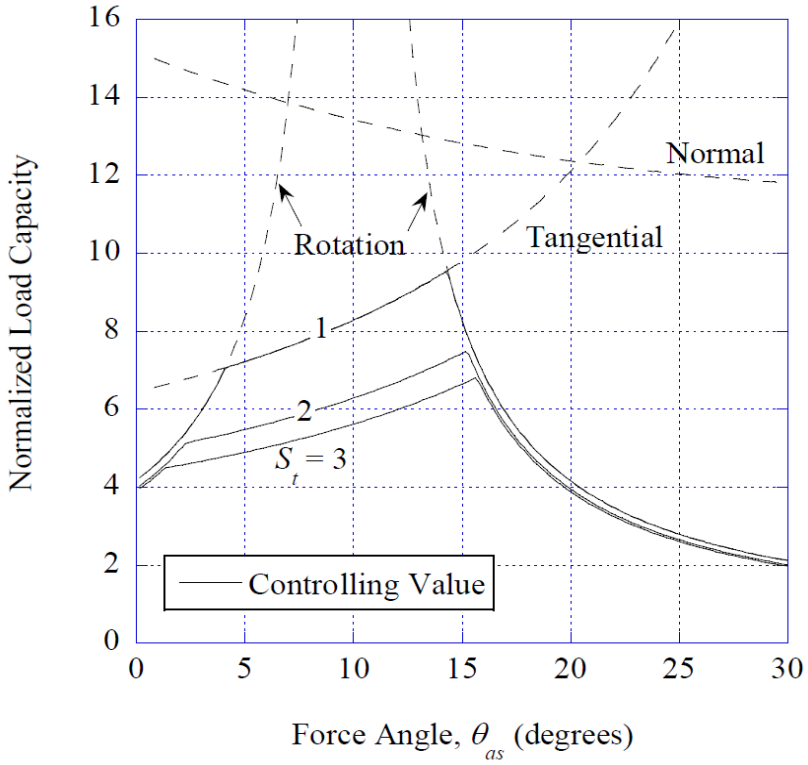

Figure 4.3 Anchor capacity curve for noninteractive resistance model

For drag embedment to occur, the controlling mechanism must be tangential translation, such that the anchor fluke will tend to slice downward in a direction parallel to the fluke as opposed to plowing upward and normal to the fluke. Viewed from this perspective, an anchor can be considered as a DEA if it exhibits the characteristics shown in Figure 4.3; i.e., tangential motion always replaces rotation as the critical collapse mechanism in the region where the rotational resistance increases without bound.

In light of the above comments, it is seen that the anchor capacity curve has three regions: (1) reverse rotation (clockwise) occurring at low load angles, $\theta_{as} < -3^{o}$ in this

example, (2) translation parallel to the fluke at intermediate load angles $-3^o < \theta_{as} < 15^o$, and (3) forward rotation at steep load angles $\theta_{as} > 15^o$. The maximum capacity N_{emax} = 9.7 occurs when the collapse mechanism transitions from a translational to a forward rotational mode. The effect of soil sensitivity S_t may be considered by taking $a_d = 1/ S_t$ in Equation 4.8 and 4.10. Soil sensitivity is seen to have three effects. First, it reduces the tendency for reverse rotation. Secondly, it increases the angle at which the controlling collapse mechanism transitions from a translational to a forward rotational mode. Finally, it reduces the maximum capacity N_{emax}; for the case considered, as S_t increases from 1 to 3 N_{emax} reduces by about 30%.

4.2.3 Interactive Effects

While the non-interactive model discussed above provides useful insights for understanding drag anchor mechanics, obtaining a realistic quantitative description of anchor capacity requires a proper accounting of the interaction effects amongst the three load components. Bransby and O'Neill (1999) propose an interaction relationship (yield function) having the following form:

$$f = \left(\frac{F_n}{F_{n\max}} \right)^q + \left[\left(\frac{M_n}{M_{\max}} \right)^m + \left(\frac{F_t}{F_{t\max}} \right)^n \right]^{\frac{1}{p}} - 1 = 0 \qquad (4.14)$$

Appropriate values of the interaction coefficients m, n, p, q are typically estimated by fitting Equation 4.14 to finite element calculations of ultimate capacity of the fluke under combined loading conditions. Examples of such curve fits for a wide fluke, with

thickness aspect ratio L_f/t_f =7, are given by Murff et al. (2005). Table 4.2 shows different estimates of interaction coefficients derived from finite element studies.

Table 4.2 Load capacity interaction coefficients for fluke with L_f/t_f =7

Exponent	Murff et al. (2005)	Yang et al. (2008)
m	1.56	1.40
n	4.19	3.49
p	1.57	1.31
q	4.43	4.14

By virtue of Equations 4.5-4.7, Equation 4.14 can be re-written as follows:

$$f = \left(\frac{|c_1| N_e}{N_{n\max}} \right)^q + \left[\left(\frac{|c_3| N_e}{N_{m\max}} \right)^m + \left(\frac{|c_2| N_e}{N_{t\max}} \right)^n \right]^{\frac{1}{p}} - 1 = 0 \tag{4.15}$$

The effective bearing factor for the anchor is then taken as the root of the equation $f(N_e) = 0$. As the coefficients c_1, c_2, c_3 are functions of uplift angle θ_{as}, the anchor capacity curve, N_e vs θ_{as}, may be computed by sweeping through the range of interest for θ_{as}.

Figure 4.4 shows example curves for sensitivities S_t = 1-3, for the base case analysis (Table 4.1) defined earlier. In the central portion of the curve dominated by translational motion parallel to the fluke, soil sensitivity strongly influences anchor capacity. In contrast, at the extremes of negative and large positive θ_{as} angles, anchor behavior is dominated by rotational motions and sensitivity has only a very minor effect.

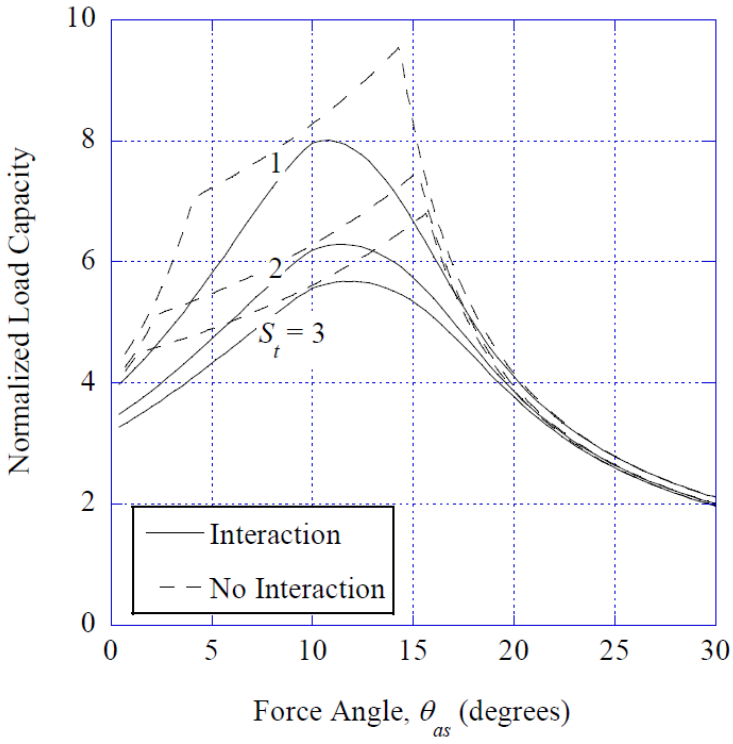

Figure 4.4 Anchor capacity curve for interactive resistance model

During drag embedment, the relative magnitudes of translational and rotational motions are of particular importance. Assuming an associated flow law, the angular and tangential velocity of the fluke, $\dot{\beta}$ and v_t, can be computed by taking appropriate partial derivatives of f:

$$\dot{\beta} = \lambda \frac{\partial f}{\partial M} \tag{4.16}$$

$$v_t = \lambda \frac{\partial f}{\partial F_t} \tag{4.17}$$

$$v_n = \lambda \frac{\partial f}{\partial F_n} \tag{4.18}$$

where λ = scalar multiplier.

The ratio of rotation to tangential translation, R_{rt} is therefore:

$$R_{rt} = \dot{\beta} L_f / v_t = \frac{c_3}{|c_3|} \frac{m}{n} \frac{N_{t\max}}{N_{m\max}} \frac{\left(|N_m| / N_{m\max}\right)^{m-1}}{\left(|N_t| / N_{t\max}\right)^{n-1}} \tag{4.19}$$

Since this ratio will vary from zero to infinity, it is convenient to plot the relative rotation in terms of a rotation parameter ψ defined by:

$$\psi = \frac{2}{\pi} \tan^{-1}\left(\dot{\beta} L_f / v_t\right) \tag{4.20}$$

where ψ is positive for positive N_m and vice-versa. For pure tangential translation $\psi = 0$, while for pure forward (counter-clockwise) rotation about the centroid of the plate $\psi = 1$. Figure 4.5 plots ψ as a function of θ_{as} for the base case analysis in Figure 4.4. In this example, $\psi = 0$ occurs at θ_{as} of about 8 degrees. The relative rotation continually increases with increasing θ_{as}, with essentially pure rotation occurring at about θ_{as} = 25-30 degrees. A plot of ψ for the non-interactive model, also in Figure 4.5, shows abrupt steps occurring at the transitions between reverse rotational, translational, and forward rotational modes of motion. Comparison to the non-interactive model predictions in Figures 4.4 and 4.5 indicates that interaction effects reduce both the maximum anchor capacity (by about 20%) and the anchor line angle θ_{as} at which the maximum capacity occurs (by about one-third in this example). The closest match between the interactive and non-interactive models occurs at $\theta_{as} = 8^0$, which corresponds to the point of pure translation ($\psi = 0$) in the interactive model.

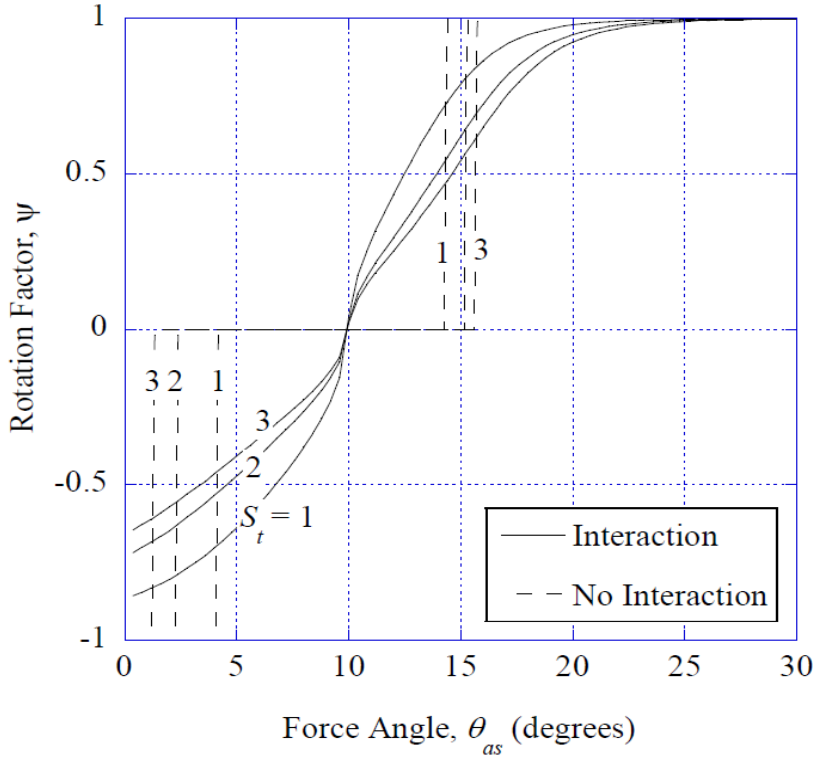

Figure 4.5 Anchor rotation in base case analysis

The ratio of normal to tangential translation R_{nt} is computed in a manner analogous to that of Equation 4.19:

$$R_{nt} = \nu_n / \nu_t = \frac{\left(N_{t\max} / N_{n\max}\right)(pq/n)}{\left[\left(\left|N_m\right| / N_{m\max}\right)^m + \left(\left|N_t\right| / N_{t\max}\right)^n\right]^{(1/p)-1}} \frac{\left(\left|N_n\right| / N_{n\max}\right)^{q-1}}{\left(\left|N_t\right| / N_{t\max}\right)^{n-1}} \tag{4.21}$$

Again, plotting a range of R_{nt} spanning from zero to infinity is facilitated by introducing a normal motion parameter ν defined as follows:

$$\nu = \frac{2}{\pi}\tan^{-1}\left(\nu_n / \nu_t\right) \tag{4.22}$$

Figures 4.6 through 4.10 illustrate the effects of the anchor geometry on the capacity curve from Equation 4.15 for an anchor in a soil with sensitivity S_t = 3 starting with a base configuration, $\theta_{fs} = 50^0$, $L_s/L_f = 1.5$, and $L_j/L_f = 0.25$. Figure 4.6 shows the effects of varying the fluke-shank angle. The peak capacity more than doubles over the range considered, $\theta_{fs} = 30\text{-}60^0$, while variations in θ_{fs} have only minor influence the angle θ_{as} at which maximum capacity is mobilized.

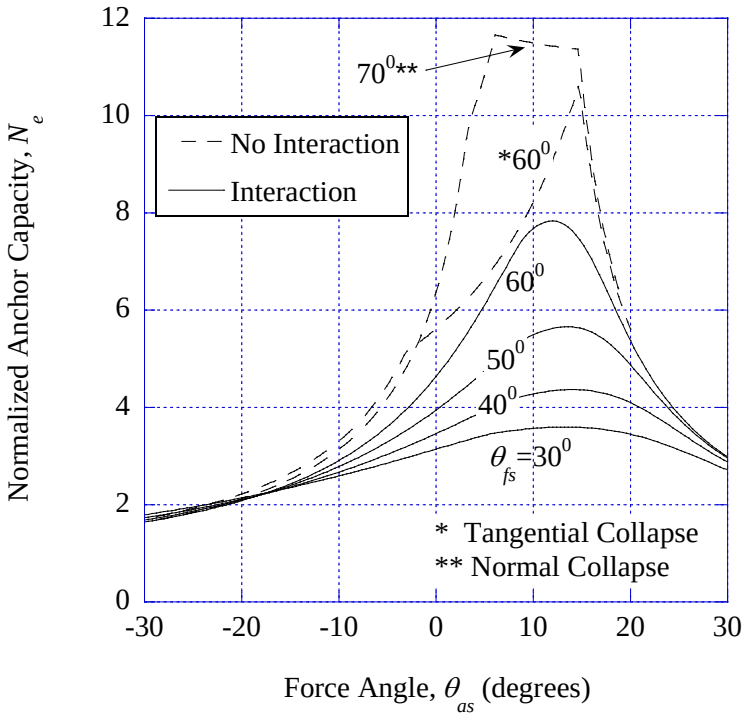

Figure 4.6 Effect of fluke-shank angle on anchor capacityN_e

The trend shown in Figure 4.6 would suggest that fluke-shank θ_{fs} should be maximized to achieve maximum anchor capacity. This is true to an extent; however, analysis using the non-interacting model (Equation 4.11-4.13, dashed lines) shows that

as θ_{fs} increases from 60^0 to 70^0, tangential motion no longer becomes a controlling collapse mechanism; i.e., the anchor will tend to move normal, rather than parallel, to the fluke. Figure 4.7, depicting the normal translation parameter ν as a function of θ_{as} presents a quantitative measure of this tendency. For small fluke-shank angles, say θ_{fs} = 30^0, the tendency for normal translation is virtually nil at any uplift angle θ_{as}. By contrast, at large θ_{fs} the normal component of fluke motion is substantial even for small θ_{as} values.

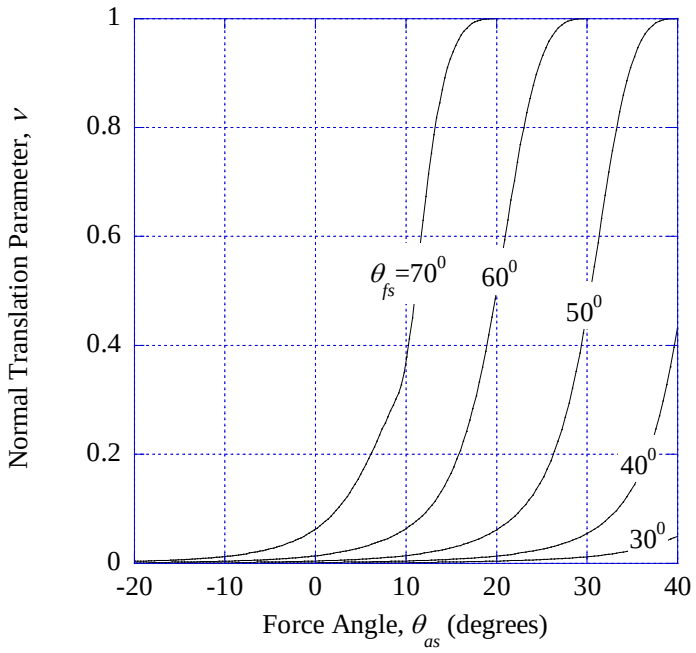

Figure 4.7 Effect of fluke-shank angle on anchor normal motions *v*

As might be expected based on Figures 4.6 and 4.7, the fluke-shank angles θ_{fs} on drag anchors in practice seldom exceed 50^0 to avoid any tendency for excessive motions

normal to the fluke. Figure 4.8, showing the influence of the shank length L_s/L_f on anchor capacity, indicates that a shorter shank length tends to produce a higher general level of anchor resistance for L_s/L_f values down to about 0.5.

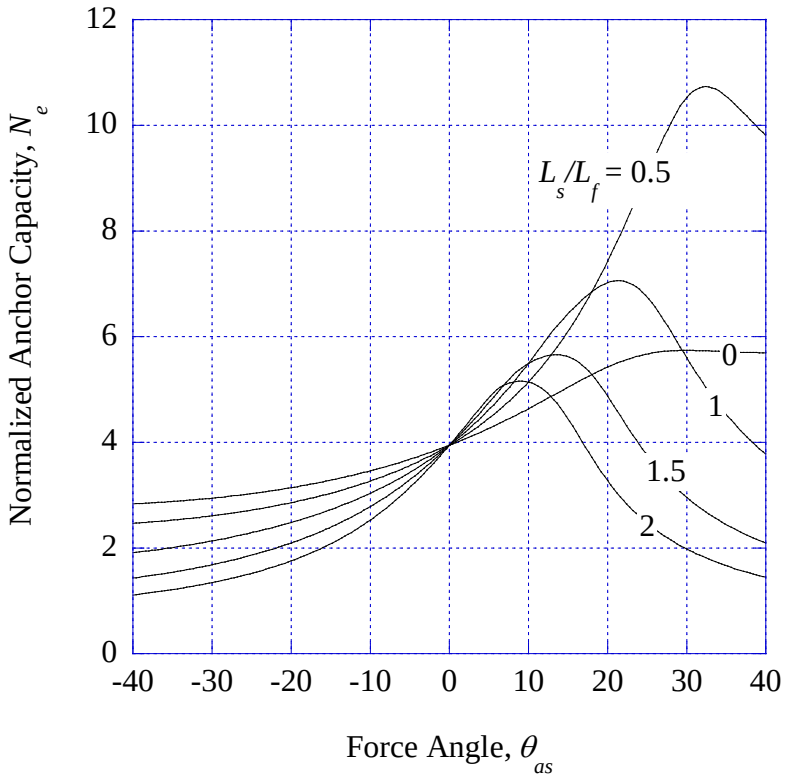

Figure 4.8 Effect of shank length on anchor capacityN_e

However, Figure 4.9 shows that reducing the shank length below L_s/L_f =1 alters the kinematic behavior of the anchor, with the gradual transition from reverse to forward rotation characteristic of longer shank lengths, L_s/L_f =1-2, being absent in the anchors have shank lengths L_s/L_f <1. Figures 8 and 9 show that having no shank at all, L_s/L_f =0, is clearly ineffective. DEA's and VLA's in practice typically have shank lengths in the

range 1.2-2; therefore, the curves in Figures 4.9 and 4.10 representing shank lengths L_s/L_f =1-2 can be considered characteristic of actual anchors. Figure 4.10 shows the effect of moving the fluke-shank attachment inward a distance L_j from the trailing edge of the fluke. The analyses show overall anchor capacity to decline with increasing L_j/L_f. Accordingly, from the standpoint of maximizing the capacity of a DEA, maintaining a relatively low value of L_j/L_f will prove most beneficial. However, subsequent phases of deployment of an anchor must still kept in mind. For example, after opening of the shank in a VLA, the more favorable location for the fluke-shank attachment point is near the centroid of the fluke.

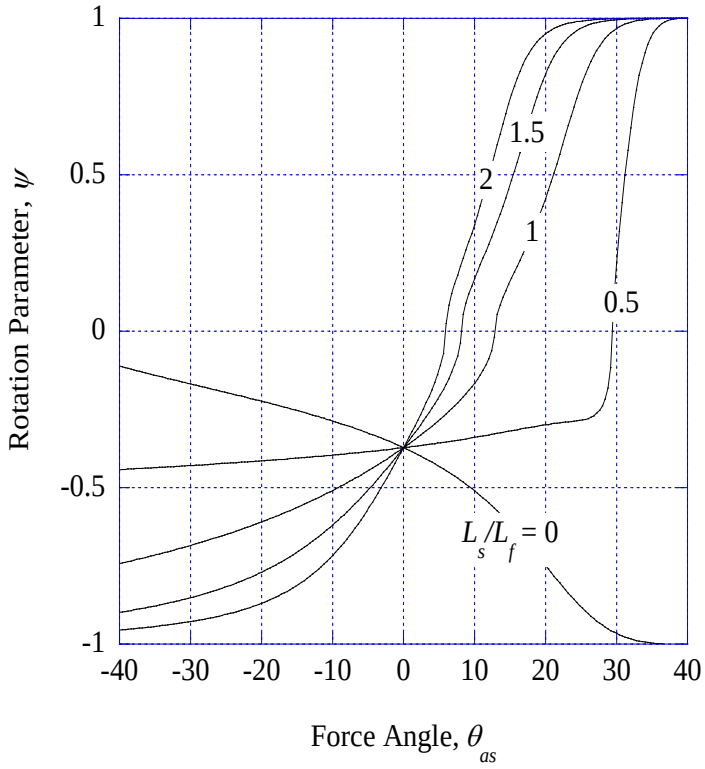

Figure 4.9 Effect of shank length on anchor rotation ψ

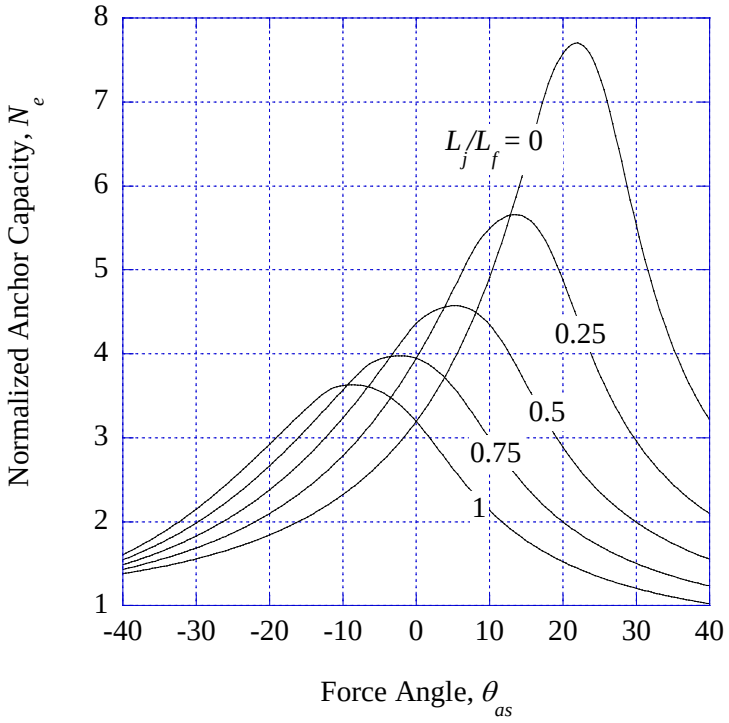

Figure 4.10 Anchor capacity curve, effect of fluke-shank attachment location

4.3 Anchor Chain Tension and Geometry

As mentioned in previous section, the behavior of the anchor is guided by the chain during the penetration. The early work of embedded anchor chains has developed by the Reese (1973) and Gault and Cox (1974); in 1982, Vivatrat et al. suggested the generalized governing equations with the soil frictional resistance and self-weight of the chain. Neubecker and Randolph (1995) evaluated previous studies and then proposed the close form solutions for anchor line tension and geometry for the special cases of soil profiles having (1) uniform strength and (2) strength proportional to depth. Their models were validated by laboratory tests.

4.3.1 Anchor Chain Tension in Soils

Figure 4.11 shows an anchor chain segment with the length *ds* with an angle θ to horizontal in soil. The tension T acts on the centroid of the cross-section of the chain which unit-length normal soil resistance Q, tangential soil resistance F, and body weight w act on its side surface.

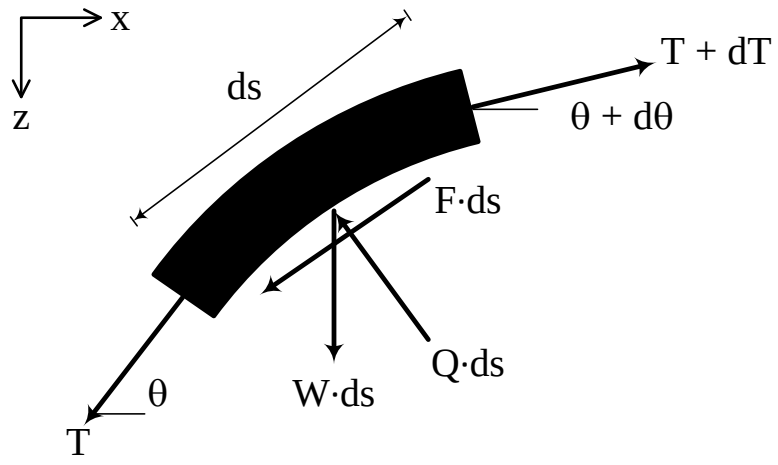

Figure 4.11 Force equilibrium for chain element

There exists a relation between Q and F:

$$F = \mu Q \tag{4.23}$$

where μ = fictional coefficient (0.4-0.6)

By the normal and tangential direction force equilibriums:

$$\text{Normal direction: } T\frac{d\theta}{ds} = -Q + w\cos\theta \tag{4.24}$$

$$\text{Tangential direction: } \frac{dT}{ds} = F + w\sin\theta \tag{4.25}$$

Substituting Equations 4.24 and 4.25 into 4.23 leads to:

$$\frac{d}{ds}\left(Te^{\mu\theta}\right) = we^{\mu\theta}\left(\sin\theta + \mu\cos\theta\right) \tag{4.26}$$

If the self-weight of the chain w is negligible comparing with soil resistance, the above equation can be simplified as:

$$\frac{d}{ds}\left(Te^{\mu\theta}\right) = 0 \qquad \Rightarrow Te^{\mu\theta} = C \text{ (Constant)} \tag{4.27}$$

Now, consider the two boundary conditions. At mudline (Figure 4.1), the tension and angle are T_0 and θ_0 respectively; whereas, the tension and angle are T_a and θ_a at the padeye. Then, substitute these two boundary conditions into above equation:

$$Te^{\mu\theta} = C = T_a e^{\mu\theta_a} = T_0 e^{\mu\theta_0} \tag{4.28}$$

$$T = T_a e^{\mu(\theta_a - \theta)} \tag{4.29}$$

$$T_0 = T_a e^{\mu(\theta_a - \theta_0)} \tag{4.30}$$

Equation 4.30 establishes the tension relationship between the shackle point and mudline. It is obvious that tension is only affected by the orientation of the chain at two boundaries if the self-weight is neglected. In general, the padeye angle θ_a is much greater than the mudline angle θ_0 (0^0-5^0), so the mudline tension is also greater than the padeye tension.

Equation 4.29 can be substituted into the force equilibrium of the chain in normal direction (Equation 4.24) under the assumption of weightless chain:

$$T_a e^{\mu(\theta_a - \theta)}\frac{d\theta}{ds} = -T_a \sin\theta e^{\mu(\theta_a - \theta)}\frac{d\theta}{dz} = -Q \tag{4.31}$$

Then,

$$T_a \int_{\theta}^{\theta_a} \sin\theta e^{\mu(\theta_a-\theta)} \frac{d\theta}{dz} = \int_z^D Q dz$$

$$\Rightarrow -\frac{T_a}{1+\mu^2}\left[e^{\mu(\theta_a-\theta)}\left(\cos\theta + \mu\sin\theta\right)\right]\Big|_{\theta}^{\theta_a} = \int_z^D Q dz = \bar{Q}\left(D-z\right)$$

$$\Rightarrow \bar{Q}\left(D-z\right) = \frac{T_a}{1+\mu^2}\left[e^{\mu(\theta_a-\theta)}\left(\cos\theta + \mu\sin\theta\right) - \left(\cos\theta_a + \mu\sin\theta_a\right)\right]$$

$$= \frac{T_a}{1+\mu^2} \times \frac{\left(\theta_a^2 - \theta^2\right)}{2}\left(1+\mu^2\right)$$

$$\Rightarrow \bar{Q}\left(D-z\right) = \frac{T_a\left(\theta_a^2 - \theta^2\right)}{2} = \int_z^D Q dz \tag{4.32}$$

where D = Depth of the shackle point

$\bar{Q}$ = Average normal soil resistance

Substituting the mudline boundary condition into Equation 4.32 leads to:

$$\frac{T_a\left(\theta_a^2 - \theta_0^2\right)}{2} = \bar{Q}D = \left[\left(E_n b\right) N_c \left(S_{u0} + \frac{kD}{2}\right)\right] D \tag{4.33}$$

where E_n = multiplier to be applied to chain bar diameter

N_c= bearing factor for wire anchor line

b = chain bar or wire diameter

S_{u0} = soil undrained shear strength at mudline

k = soil strength gradient with respect to depth

Actually, Equation 4.33 describes the anchor chain tension and its orientation variation with different soil strength properties and chain dimension. Once the chain diameter and

soil properties are known, the anchor line tension is inverse proportional to the difference of square of two angles.

Now, define two dimensionless factors:

$$\hat{T}_a = \frac{T_a}{S_{ua} b^2} = \frac{T_a}{(S_{u0} + kD) b^2} \tag{4.34}$$

$$\eta = \frac{kb}{S_{u0}} \tag{4.35}$$

$$\hat{z} = \frac{D}{b} \tag{4.36}$$

Equation 4.33 could be modified as following by above two equations substituted:

$$\frac{E_n N_c \eta}{2} (\hat{z})^2 + \left(E_n N_c - \frac{\hat{T}_a \eta (\theta_a^2 - \theta_0^2)}{2} \right) \hat{z} - \frac{\hat{T}_a (\theta_a^2 - \theta_0^2)}{2} = 0 \tag{4.37}$$

Since E_n, N_c, and η are constants and only $\hat{z}$ is the independent variable, the differentiation of the Equation 4.37 is:

$$\begin{aligned} E_n N_c (1 + \eta \hat{z}) - \frac{\hat{T}_a \eta (\theta_a^2 - \theta_0^2)}{2} - \eta \hat{z} \frac{(\theta_a^2 - \theta_0^2)}{2} \frac{d\hat{T}_a}{d\hat{z}} - \hat{T}_a \eta \hat{z} \left(\theta_a \frac{d\theta_a}{d\hat{z}} - \theta_0 \frac{d\theta_0}{d\hat{z}} \right) \\ - \frac{d\hat{T}_a}{d\hat{z}} \frac{(\theta_a^2 - \theta_0^2)}{2} - \hat{T}_a \left(\theta_a \frac{d\theta_a}{d\hat{z}} - \theta_0 \frac{d\theta_0}{d\hat{z}} \right) = 0 \end{aligned} \tag{4.38}$$

Using chain rule:

$$\frac{d\hat{T}_a}{d\hat{z}} = \frac{d\hat{T}_a}{d\theta_a} \frac{d\theta_a}{d\hat{z}} \tag{4.39}$$

$$\frac{d\theta_0}{d\hat{z}} = \frac{d\theta_0}{d\theta_a} \frac{d\theta_a}{d\hat{z}} \tag{4.40}$$

Then,

$$E_n N_c\left(1+\eta\hat{z}\right)-\frac{\hat{T}_a\eta(\theta_a^2-\theta_0^2)}{2}-\frac{(\theta_a^2-\theta_0^2)}{2}\left(1+\eta\hat{z}\right)\frac{d\hat{T}_a}{d\theta_a}\frac{d\theta_a}{d\hat{z}}$$
$$-\hat{T}_a\left(1+\eta\hat{z}\right)\left(\theta_a-\theta_0\frac{d\theta_0}{d\theta_a}\right)\frac{d\theta_a}{d\hat{z}}=0 \tag{4.41}$$

The anchor line angle rotation rate at padeye is:

$$\frac{d\theta_a}{d\hat{z}}=\frac{\left(\frac{E_n N_c}{\hat{T}_a}-\frac{\theta_a^2-\theta_0^2}{2(1/\eta+\hat{z})}\right)}{\left(\theta_a-\theta_0\frac{d\theta_0}{d\theta_a}\right)+\frac{1}{\hat{T}_a}\frac{d\hat{T}_a}{d\theta_a}\frac{\theta_a^2-\theta_0^2}{2}} \tag{4.42}$$

Similarly, using chain rule:

$$\frac{d\hat{T}_a}{d\theta_a}=\frac{d\hat{T}_a}{d\theta_{as}}\frac{d\theta_{as}}{d\theta_a}=\frac{d\hat{T}_a}{d\theta_{as}}\frac{d\left(\theta_a-\theta_s\right)}{d\theta_a}=\frac{d\hat{T}_a}{d\theta_{as}}\left(1-\frac{d\theta_s}{d\theta_a}\right) \tag{4.43}$$

Finally, Equation 3.42 can be modified as:

$$\frac{d\theta_a}{d\hat{z}}=\frac{\left(\frac{E_n N_c}{\hat{T}_a}-\frac{\theta_a^2-\theta_0^2}{2(1/\eta+\hat{z})}\right)}{\left(\theta_a-\theta_0\frac{d\theta_0}{d\theta_a}\right)+\frac{1}{\hat{T}_a}\frac{d\hat{T}_a}{d\theta_{as}}\left(1-\frac{d\theta_s}{d\theta_a}\right)\frac{\theta_a^2-\theta_0^2}{2}} \tag{4.44}$$

The reason for transforming Equation 4.42 to 4.44 is that the rate of change of normalized shackle tension is closely linked to the rate of change of the angle θ_{as} changing rate based on numerical studies (Section 4.4). Although the equation illustrates the anchor line angle changing at shackle point, it is also regarded as the angle changing of the shank or the fluke to investigate the trajectory of the anchor (Aubeny and Chi, 2010).

4.3.2 Anchor Chain Geometry in Soils

The geometry of the chain can be significant, particularly in shallow water where the length of embedded chain in the soil affects the chain geometry in the water column. The anchor chain inclined angle to the horizontal θ can be determined from the Equation 4.32:

$$\theta^2 = \theta_a^2 - \frac{2}{T_a}\int_z^D Q dz \tag{4.45}$$

Consider the normal soil resistance which its strength is proportional to the depth:

$$Q = q\ E_n N_c b = \left(S_{u0} + kz\right) E_n N_c b \tag{4.46}$$

Then, substitute above relation into Equation 4.45:

$$\begin{aligned} \theta^2 &= \theta_a^2 - \frac{2E_n N_c b}{T_a}\int_z^D \left(S_{u0} + kz\right) dz \\ &= \theta_a^2 - \frac{2E_n N_c b}{T_a}\left(S_{u0}D + \frac{1}{2}kD^2\right) + \frac{2E_n N_c b}{T_a}\left(S_{u0}z + \frac{1}{2}kz^2\right) \end{aligned} \tag{4.47}$$

At mudline (z = 0), the angle $\theta = \theta_0$ so the above equation could be modified as:

$$\theta^2 = \theta_0^2 + \frac{2E_n N_c b}{T_a}\left(S_{u0}z + \frac{1}{2}kz^2\right) \tag{4.48}$$

Let $z^* = \frac{z}{D}$, above equation can be written as:

$$\theta^2 = \theta_0^2 + \frac{2E_n N_c b}{T_a}\left(S_{u0}Dz^* + \frac{kD^2}{2}\left(z^*\right)^2\right) \tag{4.49}$$

Let $C_1 = \frac{2E_n N_c b}{T_a} S_{u0} D \qquad C_2 = \frac{E_n N_c b}{T_a} kD^2 \qquad x^* = \frac{x}{D}$

The anchor chain inclination angle is then:

$$\theta = -\frac{dz}{dx} = -\frac{dz^*}{dx^*} = \sqrt{\theta_0^2 + C_1 z^* + C_2 \left(z^*\right)^2} \tag{4.50}$$

Then, the normalized geometry of the chain can be determined by the following:

$$\int_0^{x^*} dx^* = -\int_1^{z^*} \frac{dz^*}{\sqrt{\theta_0^2 + C_1 z^* + C_2 \left(z^*\right)^2}}$$

$$\Rightarrow x^* = \int_{z^*}^1 \frac{dz^*}{\sqrt{\theta_0^2 + C_1 z^* + C_2 \left(z^*\right)^2}}$$

$$= \frac{1}{\sqrt{C_2}} \ln\left[2C_2 z^* + C_1 + 2\sqrt{C_2\left(C_2\left(z^*\right)^2 + C_1 z^* + \theta_0^2\right)} \right]\Bigg|_{z^*}^1$$

$$x^* = \frac{1}{\sqrt{C_2}} \ln\left[\frac{2C_2 + C_1 + 2\sqrt{C_2\left(C_2 + C_1 + \theta_0^2\right)}}{2C_2 z^* + C_1 + 2\sqrt{C_2\left(C_2\left(z^*\right)^2 + C_1 z^* + \theta_0^2\right)}} \right] \tag{4.51}$$

Since both the chain depth and distance are normalized by the anchor shackle penetration D, the dimensionless x^*-z^* relation is obtained from Equation 4.51 and then the real geometry can be computed simply by multiplying the shackle depth. The ratio of two dimensionless parameters C_2 and C_1 implies the condition of soil profiles:

$$\frac{C_2}{C_1} = \frac{1}{2}\frac{kD}{S_{u0}} = \frac{1}{2}\eta^* \tag{4.52}$$

For uniform soil, the factor $\eta^* = 0$; whereas, it approaches infinity for a soil with zero mudline strength. Figure 4.12 presents the normalized anchor chain geometry curves for different soil conditions. The dash curves present the limiting cases for all possible chain

geometries in all soil conditions ($\eta^* = 0$ & $\eta^* \to \infty$). With increasing the η^* value, the anchor chain intercepts with mudline (z = 0) at larger distance to the shackle point.

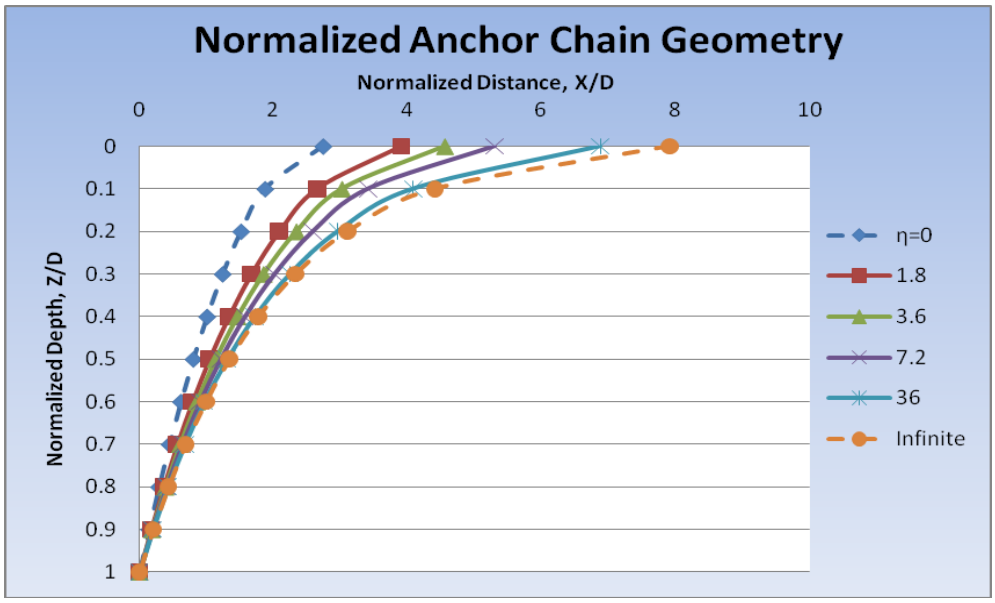

Figure 4.12 Normalized anchor chain geometry

One special case is the mudline strength $S_{u0} = 0$ ($C_1 = 0$ or $\eta^* \to \infty$). The equation of chain geometry can be determined from Equation 4.51:

$$x^* = \frac{1}{\sqrt{C_2}} \ln\left[\frac{2C_2 + 2\sqrt{C_2\left(C_2 + \theta_0^2\right)}}{2C_2 z^* + 2\sqrt{C_2\left(C_2\left(z^*\right)^2 + \theta_0^2\right)}}\right] = \frac{1}{\sqrt{C_2}} \ln\left[\frac{1 + \sqrt{1 + \frac{\theta_0^2}{C_2}}}{z^* + \sqrt{\left(z^*\right)^2 + \frac{\theta_0^2}{C_2}}}\right] \quad (4.53)$$

Actually above equation matches the solution of case of soil with bearing resistance proportional to depth developed by Neubecker and Randolph (1995). Another special

case is the chain in uniform soil ($C_2 = 0$ or $\eta^* = 0$). The solution also can be derived from Equation 4.51 by L'Hospital's rule:

$$x^* = \lim_{C_2 \to 0} \left\{ \frac{1}{\sqrt{C_2}} \ln \left[\frac{2C_2 + C_1 + 2\sqrt{C_2\left(C_2 + C_1 + \theta_0^2\right)}}{2C_2 z^* + C_1 + 2\sqrt{C_2\left(C_2\left(z^*\right)^2 + C_1 z^* + \theta_0^2\right)}} \right] \right\}$$

$$= \lim_{C_2 \to 0} \left\{ \frac{4\sqrt{C_2} + \dfrac{2\sqrt{C_2}\left(2C_2 + C_1 + \theta_0^2\right)}{\sqrt{C_2\left(C_2 + C_1 + \theta_0^2\right)}}}{2C_2 + C_1 + 2\sqrt{C_2\left(C_2 + C_1 + \theta_0^2\right)}} \right.$$

$$\left. - \frac{4\sqrt{C_2} z^* + \dfrac{2\sqrt{C_2}\left(2C_2\left(z^*\right)^2 + C_1 z^* + \theta_0^2\right)}{\sqrt{C_2\left(C_2\left(z^*\right)^2 + C_1 z^* + \theta_0^2\right)}}}{2C_2 z^* + C_1 + 2\sqrt{C_2\left(C_2\left(z^*\right)^2 + C_1 z^* + \theta_0^2\right)}} \right\}$$

$$= \frac{1}{C_1} \frac{2\left(C_1 + \theta_0^2\right)}{\sqrt{C_1 + \theta_0^2}} - \frac{1}{C_1} \frac{2\left(C_1 z^* + \theta_0^2\right)}{\sqrt{C_1 z^* + \theta_0^2}}$$

$$x^* = \sqrt{\frac{C_1}{4}} \left[\sqrt{\frac{\theta_0^2}{C_1} + 1} - \sqrt{\frac{\theta_0^2}{C_1} + z^*} \right] \tag{4.54}$$

Similarly, Neubecker and Randolph also present closed form solution for this case equivalent to Equation 4.54. It is obvious that their two equations present the chain geometry of these two special cases (two dash curves in Figure 4.12) and it may not be representative of many soil profiles. It should be noted that the normalized distance x^* in

the case of mudline strength $S_{u0} = 0$ ($\eta^* \to \infty$) approaches infinity at the mudline for the case of a horizontal mudline angle ($\theta_0 = 0$).

4.4 Anchor Trajectory

The section 4.2 presented an analysis of the load capacity and kinematic behavior of a drag embedment anchor at a given instant in its trajectory. The second aspect of the problem involves the prediction of the trajectory of the anchor as drag embedment progresses. In doing so, it is necessary to consider the mechanics of the anchor line in addition to those of the anchor itself. Therefore, the anchor chain tension and geometry and chain rotation rate at shackle point are investigated in previous sections.

Although these solutions are strictly valid only for small chain angles, Neubecker and Randolph (1995) report reasonable agreement to more rigorous solutions. For a fixed shackle point depth *z*, Equation 4.33 describes an inverse square relationship between tension T_a and anchor line angle θ_a at the shackle point. By invoking Equation 4.4, any anchor capacity curve may be expressed in terms of total anchor capacity *F* as a function of θ_a, so long as the current anchor orientation θ_s (Figure 4.1) is known. The intersection of the two loci, T_a-θ_a and F-θ_a produces a unique solution (T_a, θ_a) for anchor line tension and angle at given depth in the trajectory. The procedure for anchor trajectory prediction described in the following paragraphs initializes at a shallow pre-embedment depth, say 1 m, for which an initial anchor line tension and uplift angle are computed using the above approach. Figure 4.13 shows an example of this initialization procedure for typical marine clay conditions (s_{u0} = 2 kPa, k = 1.57 kPa/m) with an

anchor line diameter b=0.073 m and the shank initially in a horizontal position, θ_s = 0. The anchor capacity curves for sensitivity S_t = 1-3 are based on the N_e - θ_{as} curves presented earlier for the base case anchor. The anchor line tension curve is computed from Equation 4.33. The recursive algorithm presented below produces subsequent computations of (T_a, θ_a) as the anchor traverses through its trajectory (Figure 4.14).

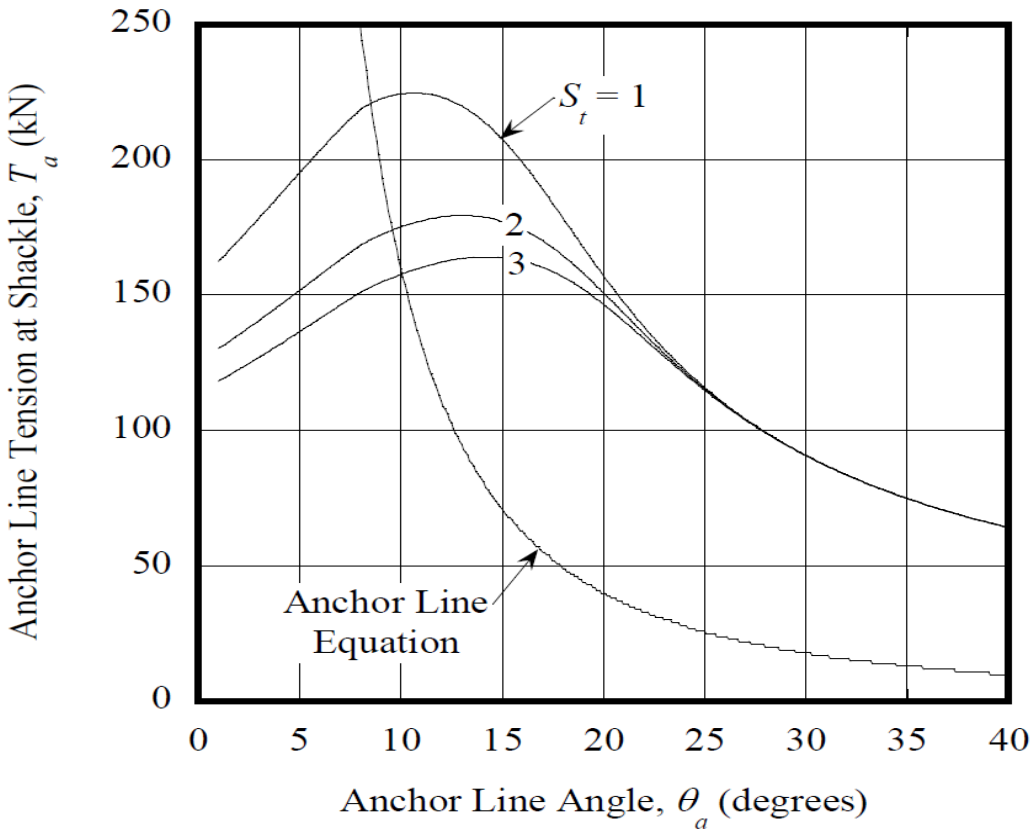

Figure 4.13 Relationship between anchor capacity curve and anchor line tension

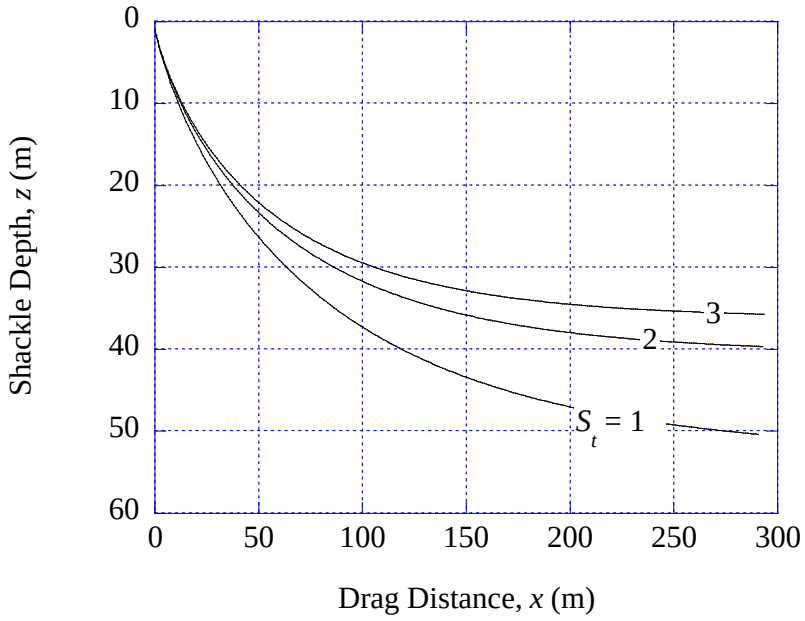

Figure 4.14 Anchor trajectory prediction during drag embedmen

4.4.1 Algorithm for Trajectory Prediction

As discussed earlier, a DEA is designed to translate primarily in a direction parallel to the fluke. Forward (counter-clockwise) rotation of the anchor will move the fluke toward a horizontal orientation which will limit the maximum depth of embedment. An analytical description of this process requires evaluation of: (1) the rate of increase in the anchor line angle θ_a with increasing embedment z, (2) the instantaneous difference between the anchor line angle and the shank angle $\theta_{as} = \theta_a - \theta_s$, and (3) the rate of rotation of the shank $\dot{\theta}_s = \dot{\beta}$ as a function of θ_{as}. The last item is governed by Equation 4.19. With regard to the first item, implicit differentiation of Equation 4.33 with respect

to z and rearrangement of terms leads to the following equation for the change in the anchor line angle θ_a at the shackle point with increasing embedment depth z.

Equation 4.44 is a refinement of an analysis presented by Aubeny et al. (2008), the most significant change being the ability to simulate conditions of variable normalized tension $\hat{T}_a$. This equation provides the basis for a recursive algorithm for predicting anchor trajectory comprising the following steps:

1. The anchor is advanced a distance Δt parallel to the fluke. From Equation 4.21, the corresponding translation normal to the fluke Δn is computed (typically small for a DEA). These motions are then resolved into vertical and horizontal components $\Delta z = \Delta t \sin\theta_f - \Delta n \cos\theta_f$ and $\Delta x = \Delta t \cos\theta_f + \Delta n \sin\theta_f$.
2. The change in the anchor line uplift angle $\Delta\theta_a$ over the depth increment Δz is computed using Equation 4.44. This requires evaluation of $d\theta_s / d\theta_a \approx \Delta\theta_s / \Delta\theta_a$. The shank rotation $\Delta\theta_s$ (=$\Delta\beta$) occurring over the increment Δt is computed from Equation 4.16, and the anchor line angle change $\Delta\theta_a$ is computed through successive iterations using Equation 4.44.
3. From the computed incremental changes in the anchor line angle and the anchor orientation, $\Delta\theta_a$ and $\Delta\theta_s$, the angle θ_{as} is updated, followed by updates of $\hat{T}_a$ and $d\hat{T}_a / d\theta_{as}$. The fluke angle θ_f is similarly updated.
4. Steps 1 through 3 are repeated until the fluke achieves a horizontal orientation $\theta_f = 0$.

At shallow embedment depths it is well known that the anchor capacity is lessened due to the proximity of the free surface (Rowe and Davis, 1982), with normal collapse

load at the surface being about one-half of that at embedment depths greater than three fluke lengths. Preliminary calculations using a reduced bearing factor at shallow depth indicated that the free surface effect did not significantly affect the overall trajectory prediction provided that the anchor did not experience a premature pull-out. However, the analyses did highlight the potential for the normal collapse load to reduce to a greater degree than the tangential collapse load due to the free surface effect. As noted earlier, if collapse occurs in a direction predominantly normal to the fluke, the drag embedment process cannot develop and premature pull-out can occur.

4.4.2 Typical Trajectory Calculation

Figure 4.14 presents the predicted trajectory for the base case anchor for the initial conditions corresponding to Figure 4.13. Figures 4.15 and 4.16 present the corresponding prediction of normalized shackle point tension $\hat{T}_a$ and force angle θ_{as}. During the initial stage of penetration the patterns of force angle θ_{as} (Figure 4.16) differ according to soil sensitivity S_t. However, as embedment progresses the force angle for all S_t tend toward a constant value of slightly more than 8^0, which for the base case anchor corresponds to pure translation parallel to the fluke ($\psi = 0$, Figure 4.5). As θ_{as} approaches its equilibrium value $\hat{T}_a$ becomes constant (Figure 4.15).

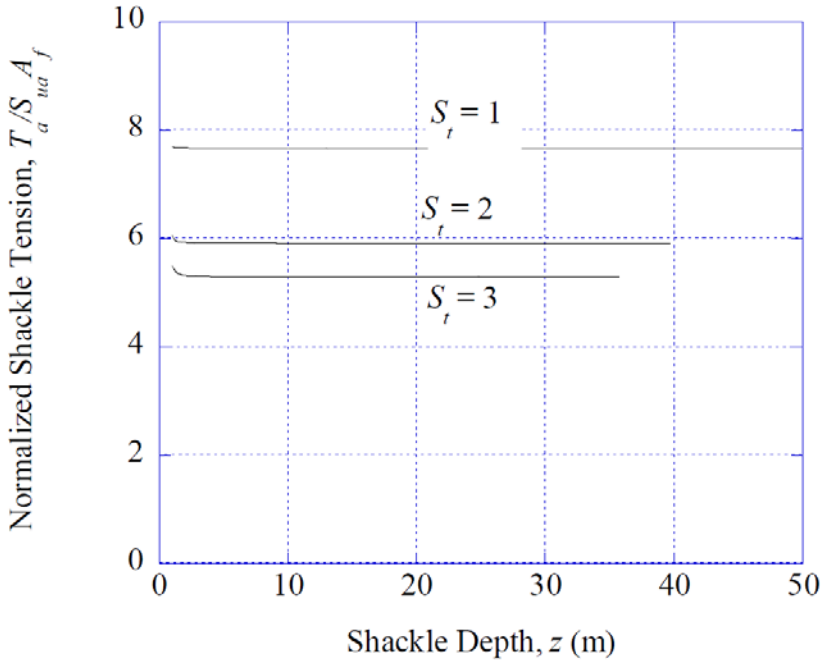

Figure 4.15 Normalized anchor tension at shackle point during drag embedment

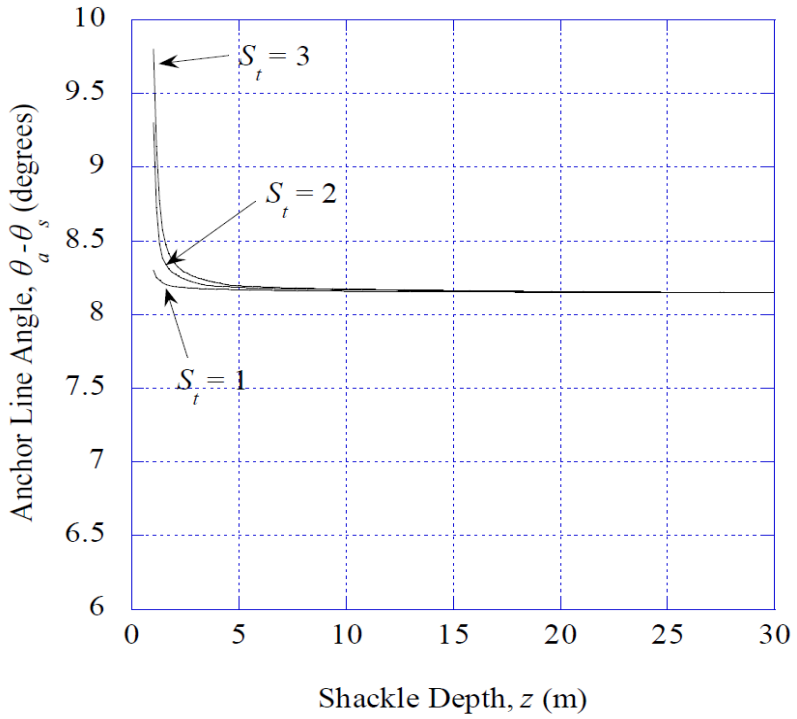

Figure 4.16 Force uplift angle θ_{as} during drag embedment

The trajectory predictions in Figure 4.14 indicate that greater embedment depths occur in less sensitive soils. At first glance this result is somewhat unexpected. However, under conditions of $d\hat{T}_a / d\theta_{as} = 0$, Equation 4.44 indicates that the higher $\hat{T}_a$ associated with low S_t will in fact reduce the rate of anchor rotation, thereby increasing the drag embedment depth.

From the base case analysis as well as parametric studies of other anchor geometries, the trajectory simulations bring to light several significant aspects of drag embedment penetration:

- Reverse rotation (negative ψ) of the anchor is inherently a self-limiting process. The tendency for reverse rotation often arises during the early stages of embedment when θ_a - and therefore θ_{as} - is small (Figure 4.5). However, by decreasing θ_s reverse rotation leads to an increase in θ_{as}. Figure 4.5 indicates that any sustained increase in θ_{as} will eventually push the anchor into the positive portion of the ψ-θ_{as} curve, which effectively halts the reverse rotational motion.
- The tendency for the anchor to experience significant forward rotation is limited for a reason similar to that discussed above regarding reverse rotation. Namely, if $\dot{\theta}_s > \dot{\theta}_a$, the angle θ_{as} declines, thereby retarding the rate of forward rotation. Consequently, the anchor moves toward an equilibrium state in which $\dot{\theta}_s = \dot{\theta}_a$; i.e., the rate of anchor rotation equals the rate of increase in the anchor line angle at the shackle. The model simulations indicate that this equilibrium state develops very

early in the trajectory; therefore, the equilibrium condition dominates anchor behavior during drag embedment.

- As a consequence of the development of an equilibrium force angle, a single value of normalized tension $(\hat{T}_a)_{eq}$ maintains itself during drag embedment once the equilibrium state is achieved. Noting that $\hat{T}_a = N_e A_f / b^2$, it follows that a single value of N_e on the anchor capacity curve largely governs the course of the anchor trajectory. For a condition of $\dot{\theta}_s = \dot{\theta}_a$ to exist, clearly some forward rotation is required. However, the model simulations indicate that the rate of anchor rotation required to keep pace with the rate of increase in the anchor line angle is quite small; i.e., ψ is positive but small. Thus, as a practical matter, the equilibrium bearing factor for the anchor closely corresponds to the translational condition for the anchor, $(N_e)_{eq} = N_e$ ($\psi = 0$).

A significant implication of the above discussion is that a single unchanging characteristic of the anchor, $(\hat{T}_a)_{eq}$, influences its trajectory during drag embedment once the equilibrium state is achieved. This considerably simplifies the anchor trajectory calculations, and permits the focus to be directed toward the behavior of the anchor line rather than the anchor. This is evident from Equation 4.44; when $d\theta_s/d\theta_a = 1$, the only variable quantities affecting $\dot{\theta}_a$ are the anchor line angles at the shackle and the mudline, θ_a and θ_0, respectively. It should finally be noted that the notion of an equilibrium value $(\hat{T}_a)_{eq}$ of an anchor is consistent with field measurements showing a

constant value of normalized shackle point tension throughout most of the trajectory (Aubeny et al, 2008).

Figure 4.17 presents the results of an example parametric study in which fluke-shank angle is varied from θ_{fs} = 30-50^0 and ratio of shank to fluke length is varied from L_s/L_f = 1-2. The wider fluke angle results in a 40-50% increase in anchor penetration depth. The predictions in Figure 4.17 also show that shortening the anchor shank from L_s/L_f = 2 to 1 increases penetration depth by some 25-30%. As is implied from Equation 4.44, a higher $(\hat{T}_a)_{eq}$ leads to a reduced rate of anchor rotation and, hence, greater penetration depth.

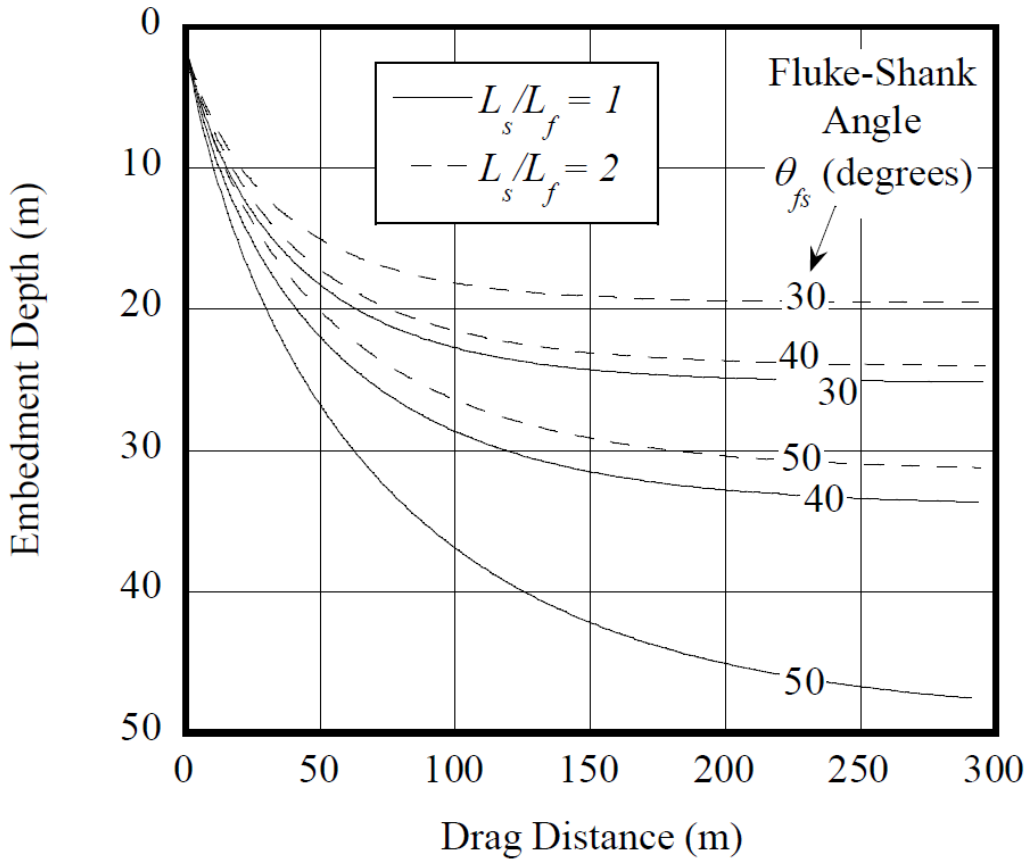

Figure 4.17 Effect of anchor geometry on predicted trajectory

Therefore, anchor geometries having the greater bearing factors under a state of pure translational motion, $(N_e)_{eq}$, can be expected to penetrate the greatest depth. Referring back to Figures 4.6 and 4.8, the anchor capacity analyses showed that widening the fluke-shank angle and shortening the shank both tend to increase the bearing factor of an anchor; consequently, the trend of the predictions presented in Figure 4.17 is not unexpected. Figure 4.18 shows the consequent increase in anchor load capacity as the fluke-shank angle is widened and the shank length is shortened. Optimizing the anchor geometry produces two benefits in that it increases both the effective bearing factor of the anchor, N_e, and the embedment depth (typically associated with higher soil strength s_u). For the parametric study considered, the combined effect from both sources is seen to enhance the ultimate load capacity of the anchor by a factor of 4 to 5.

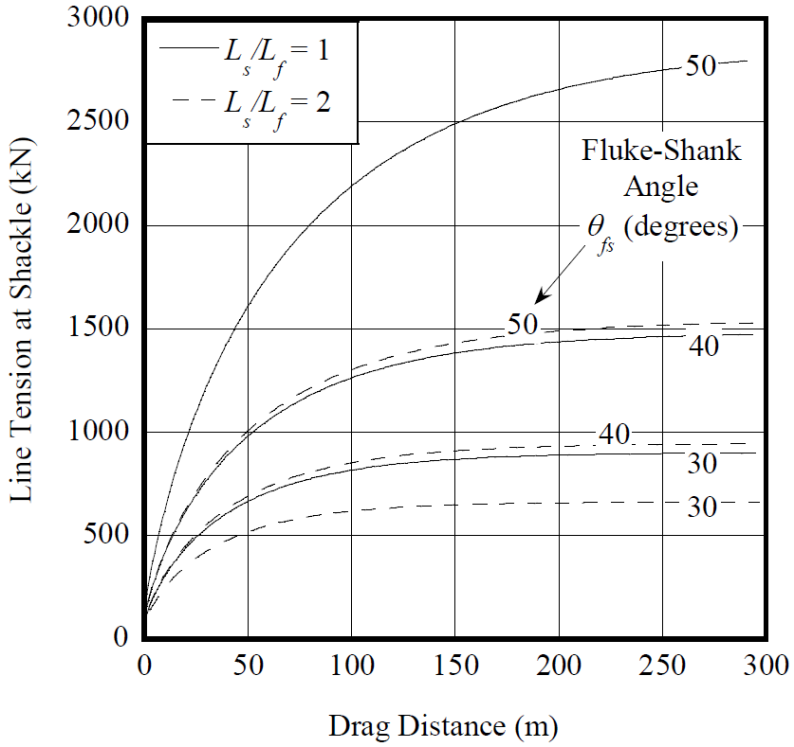

Figure 4.18 Effect of anchor geometry on predicted load capacity

4.4.3 Anchor Trajectory and Chain Geometry Prediction from Field Measured Data

Although the anchor trajectory and chain geometry can be predicted well from the methods discussed in previous sections, they may be more accurate if some field measured data, including in-situ soil strength properties, are involved in the prediction. During the procedure of the installations of drag anchors, both the anchor line tension and the chain inclined angle at mudline (T_0 and θ_0) are measured. Therefore, from the aspect of anchor chain in soils, only the chain tension and uplift angle at shackle point are unknown. Recall the chain solutions in section 4.3.1, Equation 4.30 elucidates the relationship of chain tensions and angle between mudline and padeye. Since the increment of chain angle at shackle is determined by Equation 4.44, the shackle tension can be computed by Equation 4.30 with the shackle chain angle θ_a substituted.

Combined with the equations stated above, the algorithm for computing the anchor trajectory with field measured mudline tension and uplift angle are developed as following steps:

1. Compute initial shackle tension by Equation 4.30 with initial θ_a assumed.
2. Calculate the soil strength at shackle S_{ua} from Equation 4.34.
3. Compute the depth of padeye from Equation 1.1.
4. Calculate the depth increment by $\Delta z = z_i - z_{i-1}$
5. Estimate the new traveling distance by $x_i = x_{i-1} + \dfrac{\Delta z}{\tan \theta_{f,i-1}}$.
6. Calculate the changing rate of the line angle at shackle from Equation 4.44 and it is equal to that of rotation of the fluke.

7. Estimate the incremental angle change by $\Delta\theta_a = \left(\frac{d\theta_a}{dz}\right)\Delta z$.

8. Update the next step fluke angle $\theta_{f,i+1} = \theta_{f,i} + \Delta\theta_a$ and the next step anchor line angle $\theta_{a,i+1} = \theta_{a,i} + \Delta\theta_a$.

9. Repeat steps 1 through 8 until the fluke approaches to a horizontal direction.

Figure 4.19 shows the field measured mudline tension T_0 and calculated shackle tension T_a; as mentioned in section 4.3.1, the mudline tension always exceeds the shackle tension and both curves approach constant values due to the orientation of the trajectory tending to be horizontal. In the figure, the symbols (*) in mudline tension curve present the measured data and based on the analytical experiences, the results of predictions will be limited if the number of data is not enough or the data sampling spacing is too large.

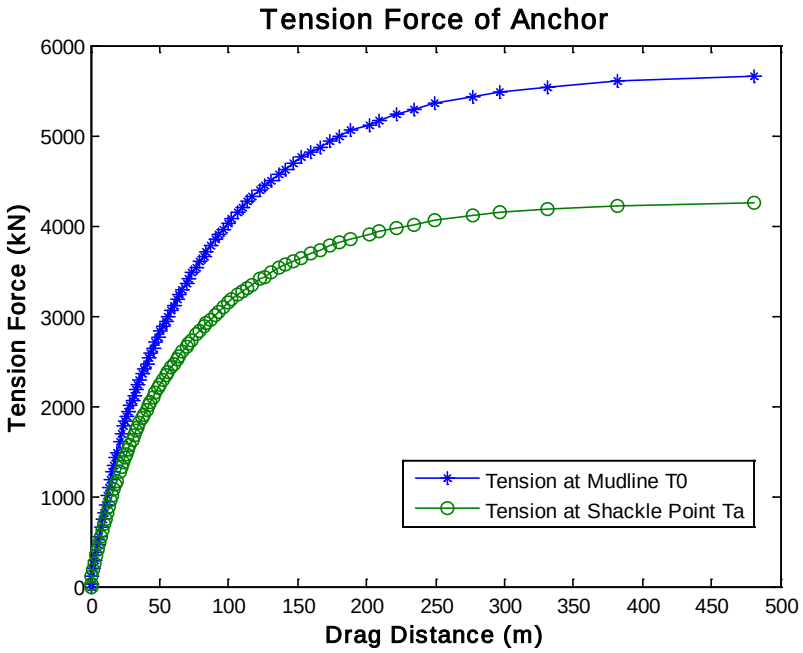

Figure 4.19 Anchor line tension prediction from field measured data

The trajectory of the anchor and the geometry of the chain are shown in Figure 4.20. The symbols (*) in the trajectory curve are the calculation results from the corresponding field measured mudline tension. The dash curves are the chain geometries of corresponding anchor locations. Although the chain geometry can be obtained from Equation 4.51, its location is calculated based on the shackle point position, i.e., the relative position to the padeye. The absolute location should be determined after the anchor padeye position is computed. In addition, due to the scales of the abscissa and ordinate in the figure, the real chain geometry is not as steep as shown in the figure due to the scale distortion.

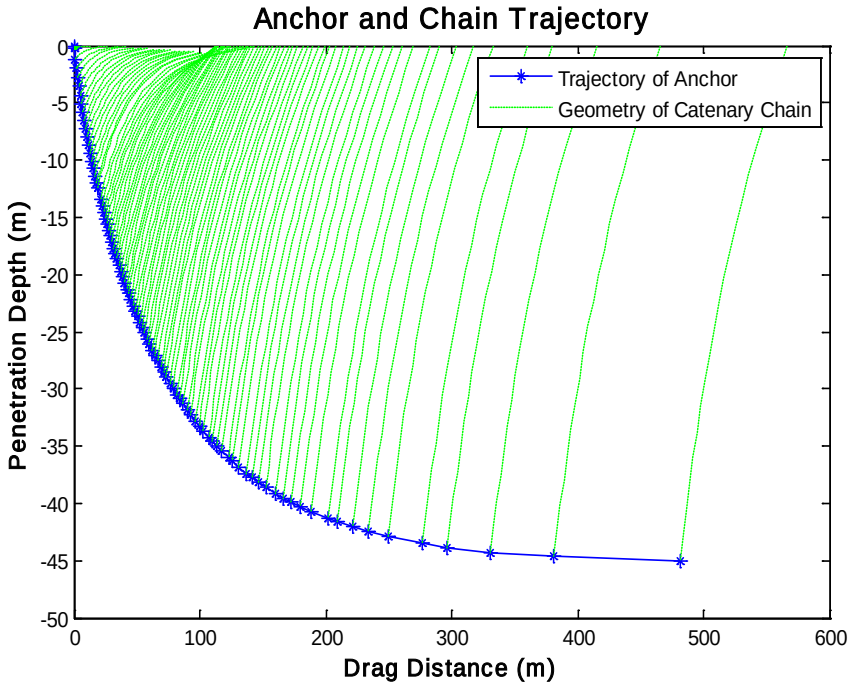

Figure 4.20 Anchor trajectory and chain geometry prediction from field measured data

CHAPTER V

MECHANICS OF DRAG EMBEDMENT ANCHORS SUBJECTING OUT-OF-PLANE LOADINGS

5.1 Research Motivation

Mooring systems for offshore floating structures, such as the semi-submersible mobile offshore drilling units (MODUs) commonly used for hydrocarbon exploration, typically comprise eight to twelve mooring lines positioned about the structure. Caissons or plate anchors may be used to secure the mooring lines; this chapter focuses on situations where drag embedment anchors (DEAs) are used, but some of the general concepts presented will apply to any anchor. When a DEA is loaded as intended, the following conditions are assumed to hold: (1) the anchor line load acts in the plane containing the shank of the anchor, a condition referred to as “in-plane” loading, and (2) the anchor chain (or anchor line if a wire line is used) lies in a vertical plane. During extreme storm events, MODUs will sometimes experience a partial failure of the mooring system. Partial failure of mooring systems for floating structures will subject drag anchors to loads having an appreciable component outside of the intended plane of loading. Partial failures of mooring systems during hurricanes in recent years have generated an interest in understanding drag anchor performance under these conditions. The consequent movement of the MODU following a partial failure will generally invalidate both assumptions stated above. Firstly, the anchor line force will no longer lie in the plane of the shank, and the anchor will be subjected to “out-of-plane” loading.

Yang et al. (2010) analyze the effect of such out-of-plane loading on anchor load capacity. Secondly, the anchor chain will no longer lie in a vertical plane; the effect of this condition on the ultimate pullout capacity of a DEA is the primary focus of this study.

5.2 Anchor Chain in an Oblique Plane

5.2.1Modeling of In-situ Situation

Figure 5.1(a) shows a plan view of the problem under consideration. A global coordinate system, x_g- y_g -z_g, may be established such that z_g is the vertical coordinate, x_g is in the plane of intended loading, and y_g is normal to the plane of intended loading. Prior to the storm event, an in-plane condition of loading exists, $\phi_{ag} = \phi_{0g} = 0$, where the angle ϕ denotes the departure of the anchor chain from an in-plane condition. The angles θ_{ag} and θ_{0g} denote the direction of the anchor chain measured from a horizontal plane at the pad-eye and mudline, respectively. The mudline angles ϕ_{0g} and θ_{0g} are arbitrarily prescribed boundary conditions for the problem. The pad-eye angles ϕ_{ag} and θ_{ag} will be computed by a procedure to be described subsequently, but for the present we will assume they have been defined. Unit vectors describing the direction of the anchor chain at the shackle and mudline can then be computed using Equations 5.1 and 5.2, respectively, as shown below:

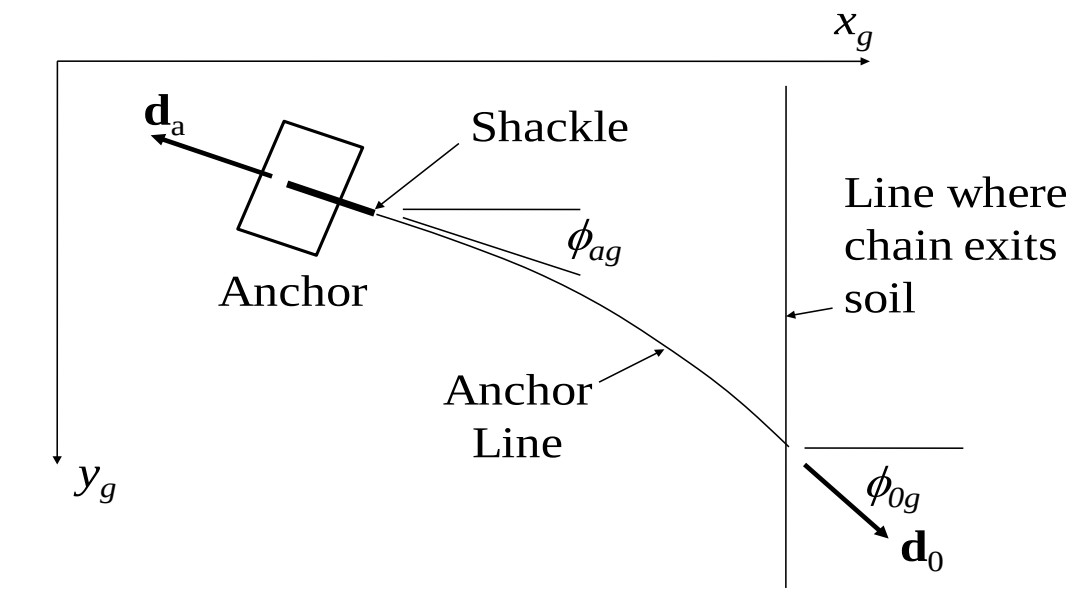

θ_{ag} in vertical plane oriented ϕ_{ag} from x_g-axis
θ_{0g} in vertical plane oriented ϕ_{0g} from x_g-axis

(a) Plan view

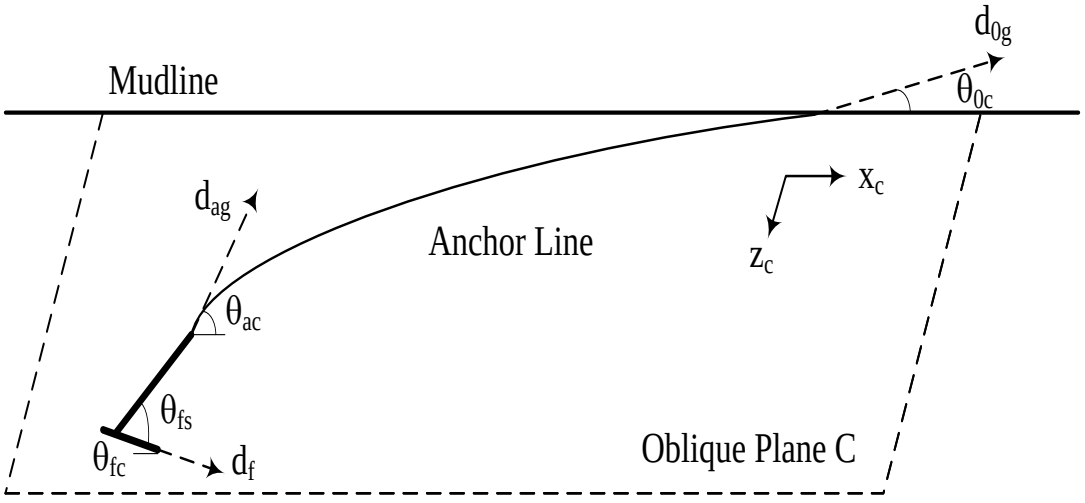

(b) Side view

Figure 5.1 Definition sketch for out-of-plane loading

$$\vec{d}_{ag} = -\,[\cos\theta_{ag}\cos\phi_{ag},\ \cos\theta_{ag}\sin\phi_{ag},\ \sin\theta_{ag}] \tag{5.1}$$

$$\vec{d}_{0g} = [\cos\theta_{0g}\cos\phi_{0g},\ \cos\theta_{0g}\sin\phi_{0g},\ \sin\theta_{0g}] \tag{5.2}$$

Further, a plane containing the direction vectors $\vec{d}_{ag}$ and $\vec{d}_{0g}$, which shall be termed the 'c-plane' (Figure 5.1(b)), can be defined in terms of the following cross product:

$$\vec{n} = \vec{d}_{0g} \times \vec{d}_{ag} \,/\, \left|\vec{d}_{0g} \times \vec{d}_{ag}\right| = [n_{xg}\ \ n_{yg}\ \ n_{zg}] \tag{5.3}$$

where $\vec{n}$ is a unit vector normal to the c-plane.

Figure 5.2 shows the system of forces acting on a chain element in the c-plane, considering the equilibrium of a chain element *ds*, where T is line tension, Q is soil resistance acting normal to chain, F is friction, and W is chain weight per unit length. Except at very shallow depths, W is small relative to the shearing resistance of the soil and may be reasonably neglected.

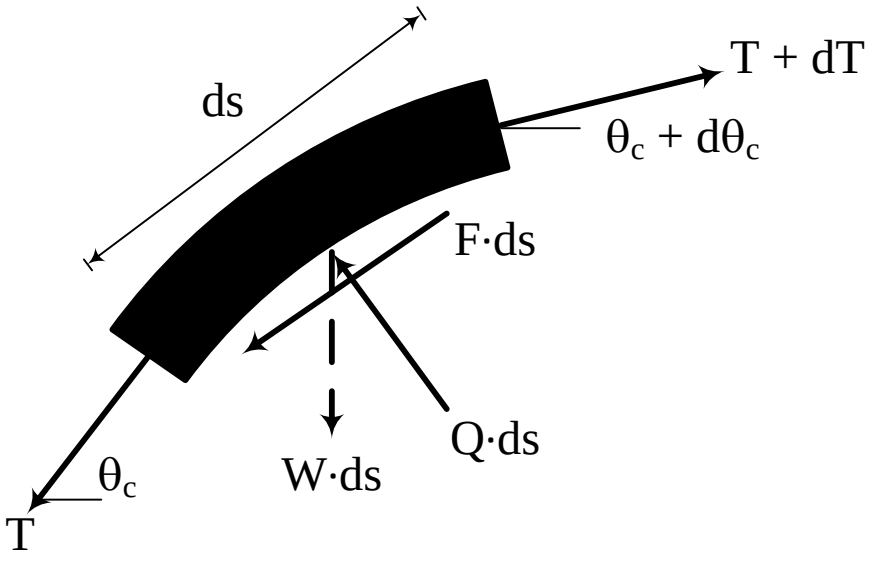

Figure 5.2 Force equilibrium for chain element on the oblique plane C

The body weight W (dash vector in Figure 5.2), comparing with Figure 4.11, is always downward vertically and not on the oblique plane. Hence, under the condition of weightless chain, the anchor line will be completely on the plane as well as the normal and tangential soil resistance.

By virtue of Equation 5.3, the tensions at the pad-eye and mudline, T_a and T_0, act within the c-plane. If the self-weight W of the chain is neglected, the integrated resultants of F and Q must also act within the c-plane. Therefore, the chain can be considered to lie in the c-plane, an oblique plane normal to the unit vector $\vec{n}$, so long as the anchor self-weight is small relative to the shearing resistance of the soil. Accordingly, the anchor line equations developed for anchor chains in a vertical plane (Neubecker & Randolph, 1995) can be adapted to the out-of-plane problem, provided appropriate coordinate transformations are made. DEA trajectory calculations derived from the Neubecker-Randolph equations (Aubeny & Chi, 2010) can similarly be adapted to calculations outside the vertical plane.

5.2.2 Coordinate Transformation

A coordinate system (x_c, y_c, z_c) can now be defined for which the chain lies in the x_c-z_c plane, subsequently termed the c-frame. It should be noted that the unit normal $\vec{n}$ to the plane of the chain acts in the y_c direction in c-frame system. The transformation is accomplished by first rotating the x_g -y_g axes an angle δ_h about the z_g axis, and then rotating an angle δ_v about the x_c axis to create an x_c-y_c-z_c frame. The appropriate matrix relating the global g-frame to the plane of the chain c-frame is then as follows:

$$\left[R_{gc}\right]=\begin{bmatrix}\cos\delta_h & \sin\delta_h & 0\\ -\cos\delta_v\sin\delta_h & \cos\delta_v\cos\delta_h & \sin\delta_v\\ \sin\delta_v\sin\delta_h & -\sin\delta_v\cos\delta_h & \cos\delta_v\end{bmatrix} \tag{5.4}$$

The angles δ_h and δ_v are defined in term of the unit normal vector $\vec{n}$ (components n_{xg}, n_{yg}, n_{zg} in the global frame) as follows:

$$\tan\delta_h=-\frac{n_{xg}}{n_{yg}} \tag{5.5}$$

$$\tan\delta_v=n_{zg} \tag{5.6}$$

Subsequent subscripts “g” and “c” in this chapter refer to the global frame and the frame oriented about the plane of the chain, respectively. It should be noted that the direction of the angles follow the right-hand rule.

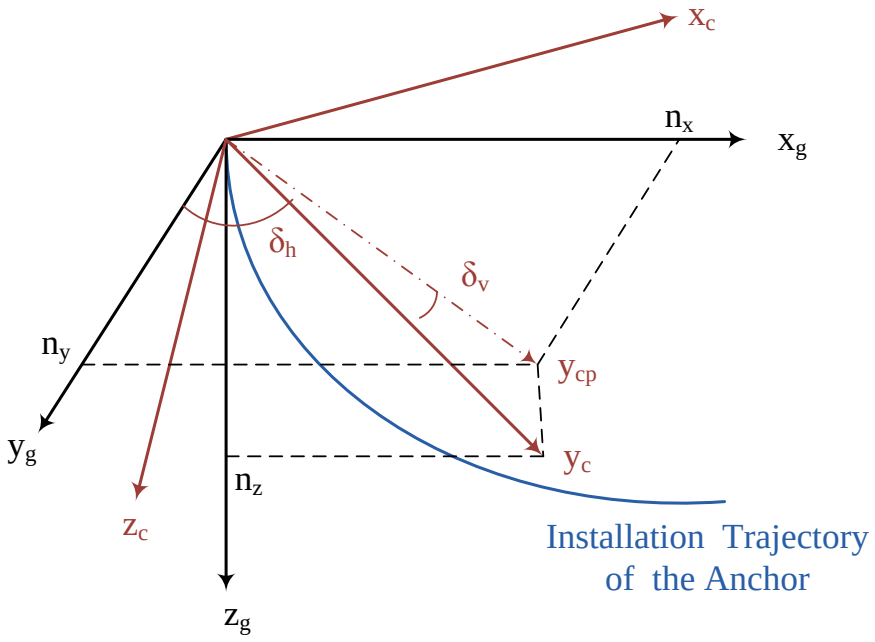

Figure 5.3 Relationship between global and local-chain coordinates

Figure 5.3 illustrates the relationship between global and local coordinates as well as the definition of two angles. The blue curve presents a trajectory of the anchor subjecting in-plane loading on the x_g -z_g plane (vertical plane); actually, this curve is the trajectory of anchor installation. The normal vector of the vertical plane is the same direction of y_g axis and y_c matches the normal (Equation 5.3) of the oblique plane (x_c –z_c). The relationship of these two coordinates can be described by the corresponding normal directions: (1) the global normal y_g rotates a horizontal angle δ_h to y_{cp} axis which is the projection of the normal of the oblique plane, and (2) from y_{cp} axis rotates a vertical angle δ_v to y_c. The coordinate transformation relation for the first rotation is:

$$\begin{Bmatrix} x_c \\ y_{cp} \\ z_g \end{Bmatrix} = \begin{bmatrix} \cos\delta_h & \sin\delta_h & 0 \\ -\sin\delta_h & \cos\delta_h & 0 \\ 0 & 0 & 1 \end{bmatrix} \begin{Bmatrix} x_g \\ y_g \\ z_g \end{Bmatrix} = [T_{\delta h}] \begin{Bmatrix} x_g \\ y_g \\ z_g \end{Bmatrix} \tag{5.7}$$

Then, the coordinate transformation relation for second rotation is:

$$\begin{Bmatrix} x_c \\ y_c \\ z_c \end{Bmatrix} = \begin{bmatrix} 1 & 0 & 0 \\ 0 & \cos\delta_h & \sin\delta_h \\ 0 & -\sin\delta_h & \cos\delta_h \end{bmatrix} \begin{Bmatrix} x_c \\ y_{cp} \\ z_g \end{Bmatrix} = [T_{\delta v}] \begin{Bmatrix} x_c \\ y_{cp} \\ z_g \end{Bmatrix} \tag{5.8}$$

Therefore, the transformation relation between g-frame and c-frame shown in Equation 5.4 can be derived as following:

$$[R_{gc}] = [T_{\delta v}][T_{\delta h}] \tag{5.9}$$

Having defined the frame rotation angles [R_{gc}], transformations of key variables from the g-frame to the c-frame can proceed. The anchor line angle at the pad-eye θ_{ac} measured in the c-plane can be evaluated by using Equations 5.4-5.6 to determine the

vector components of $\vec{d}_a$ in the c-frame, $\vec{d}_{ac} = -[d_{axc}\ d_{ayc}\ d_{azc}]$, from which θ_{ac} in Figure 5.4 can be calculated:

$$\theta_{ac} = \tan^{-1}\left(\frac{d_{azc}}{d_{axc}}\right) \tag{5.10}$$

A similar transformation is possible for the anchor line angle at the mudline θ_{0c}.

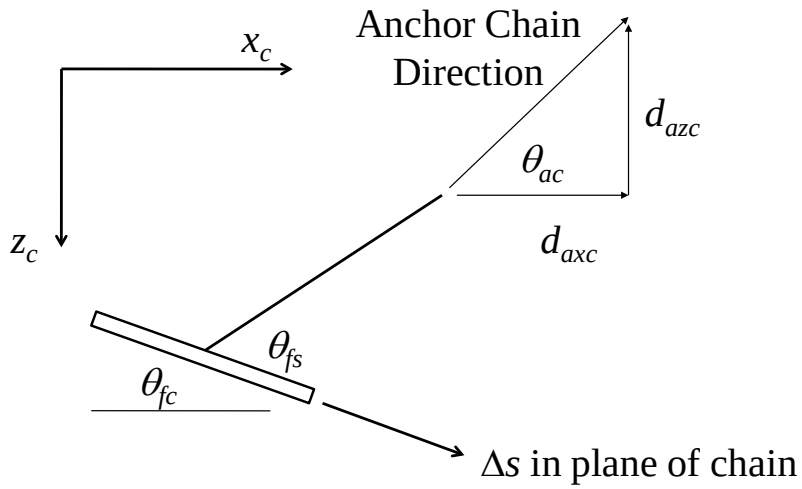

Figure 5.4 Anchor in plane of chain

5.3 Out-of-Plane Anchor Tension and Trajectory

5.3.1 Modification of Anchor Chain Tension and Rotation Theory

As mentioned in previous sections, the anchor chain lies on an oblique plane since the self body weight is small relative to the soil resistance. The chain tension and angle rotation theory discussed in subsection 4.3 may not applicable directly because they are derived based on in-plane motion, i.e., the anchor travels on a vertical plane. Therefore, a revised form of the Neubecker and Randolph (1995) relationship between line tension

and line angles can now be derived along the same procedures as Equation 4.33 for the case of an anchor line lying in an oblique plane:

$$T_a\left(\theta_{ac}^2-\theta_{0c}^2\right)/2=E_nN_cbZ_c\left(s_{u0}+kZ_c\cos\delta_v/2\right) \tag{5.11}$$

where T_a is anchor line tension at shackle point, E_n is multiplier applied to chain bar diameter, N_c= bearing factor for wire anchor line, b = chain bar or wire diameter, s_{u0} is the soil undrained shear strength at mudline, k is soil strength gradient with depth, and Z_c is the distance from the anchor shackle to mudline in the z_c direction. From Figure 5.5 it is apparent that $Z_c = z_c / \cos^2 \delta_v$. The angle δ_v is defined in Equation 5.6 and shown in Figure 5.3; actually, it is also the angle between z_c and z_g axis (Figure 5.5).

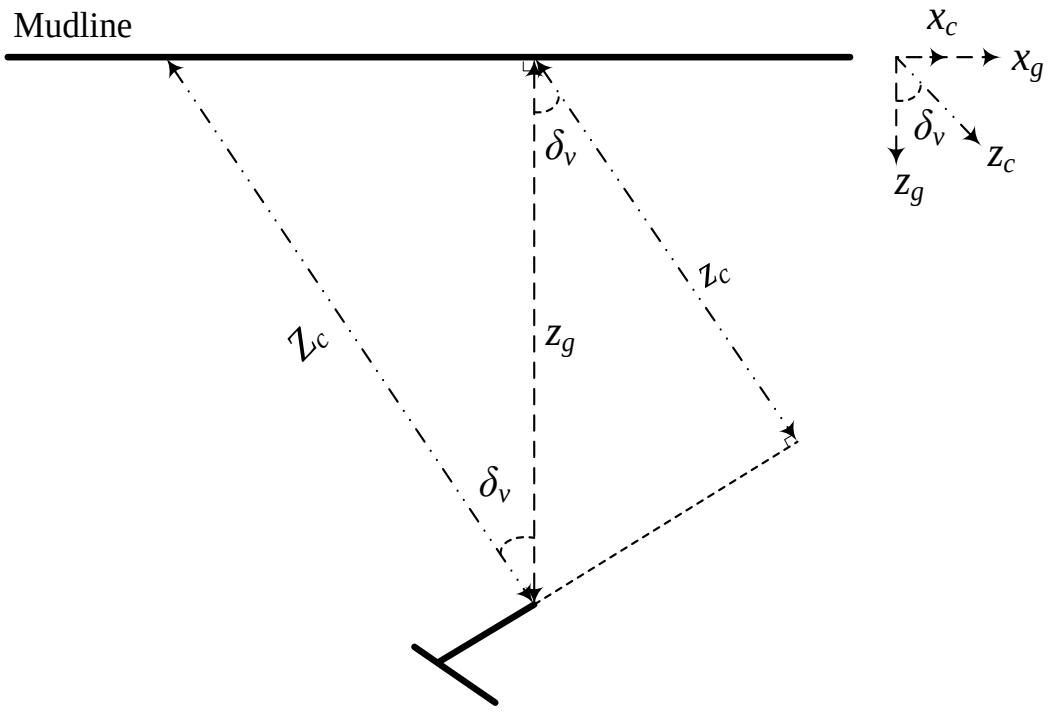

Figure 5.5 Depth parameters in the plane of chain

The $x_g - z_g$ frame and the $x_c - z_c$ frame shown in Figure 5.5 are not in the same plane (vertical plane). The angle between x_g and z_g axis is δ_h. In addition, the chain tension relation between mudline and shackle (Equation 4.30) should be modified as:

$$T_0 = T_a e^{\mu(\theta_{ac} - \theta_{0c})} \tag{5.12}$$

Although above equation is described in $x_c - z_c$ frame, the magnitudes of chain tension T_0 and T_a do not change with different coordinates.

Finally, for trajectory calculations the rate of change of θ_{ac} with respect to the change in depth can calculated in the manner described by Aubeny & Chi (2010). When expressed in terms of z_c rather than Z_c, the rate equation takes the following form:

$$\frac{d\theta_{ac}}{d\hat{z}_c} = \frac{\left(\frac{E_n N_c}{\hat{T}_a} - \frac{\theta_{ac}^2 - \theta_{0c}^2}{2(1/\eta_c + \hat{z}_c / \cos^2 \delta_v)} \right)}{\cos^2 \delta_v \left(\theta_{ac} - \theta_{0c} \frac{d\theta_{0c}}{d\theta_{ac}} \right)} \tag{5.13}$$

where $\hat{z}_c$ is normalized depth of shackle (= z_c/b), $\hat{T}_a$ is normalized tension at shackle (= $T_a / s_{ua}\ b^2$), s_{ua} is soil shear strength at the shackle, $d\theta_{0c}/d\theta_{ac}$ is the rate of change of mudline angle, η_c is a strength gradient parameter (= $b\ k \cos \delta_v / s_{u0}$). Therefore, the rate equation for computing the change in θ_{ac} with increasing embedment in the three-dimensional case assumes a nearly identical form to that of an anchor contained within a vertical plane. It should be always kept in mind that only the tension or normalized tension terms, including dimensionless bearing factors, are invariant with different coordinates in Equation 5.11-5.13.

5.3.2 Numerical Computation Sequence for Anchor Trajectory

Having formulated the necessary transformations to describe the anchor chain in an oblique plane, trajectory prediction can proceed according to the sequence outlined below.

1. Initial installation to an arbitrarily selected depth z_i and the tension T_{ai} corresponding to this depth are computed using the procedure of Aubeny and Chi (2010) developed for vertical in-plane motion. Anchor line angles at the end of this installation stage are θ_{agi} and θ_{0gi}.
2. At this point, a partial mooring failure is simulated in which the anchor line angle at the mudline deviates from the intended plane of loading (the x_g direction in Figure 5.1) by an angle ϕ_{0g}. The anchor line angle at the pad-eye is assumed to be initially unaffected by this change, such that $\phi_{ag} = 0$ and $\theta_{ag} = \theta_{agi}$. From Equations 5.1-5.7, the anchor line angles, θ_{aci} and θ_{0ci} measured in the c-plane, can be computed. Inserting these values into Equation 5.11 permits the current line tension T_a to be calculated. The calculations will show that the current pad-eye tension is less than the original installation tension, $T_a < T_{ai}$. Therefore, as continued loading occurs, the anchor will remain stationary and the angle θ_{ac} decreases until $T_a = T_{ai}$. During this "line tautening" process, the orientation of the c-plane changes continuously as θ_{ac} changes.
3. When the line tension reaches the point at which $T_a = T_{ai}$, further loading will be accompanied by a resumption of the drag embedment process, now in the c-plane. Experience with simulations of two-dimensional trajectories (Aubeny & Chi, 2010)

implied that a drag anchor rapidly aligns itself with the anchor line such that the line of action of T_a acts through the center of the anchor. A similar process is assumed to occur under three-dimensional loading conditions. That is, upon resumption of the drag embedment process, the anchor is assumed to rapidly re-align itself such that the shank lies in the c-plane.

4. Considering the orientation of the anchor in the c-plane (Figure 5.4), the orientation of the fluke will therefore be $\theta_{fc} = \theta_{fs} - \theta_{ac}$. If the fluke advances an increment of distance Δs in the direction of the fluke, then the components of displacement in the c-plane become:

$$\Delta x_c = \Delta s \cdot \cos\theta_{fc} \tag{5.14}$$

$$\Delta y_c = 0 \tag{5.15}$$

$$\Delta z_c = \Delta s \cdot \sin\theta_{fc} \tag{5.16}$$

5. The coordinates of the shackle in the global frame are accomplished through the use of the inverse of matrix $[R_{gc}]^{-1}$:

$$\begin{Bmatrix} \Delta x_g \\ \Delta y_g \\ \Delta z_g \end{Bmatrix} = \left[R_{gc} \right]^{-1} \begin{Bmatrix} \Delta x_c \\ 0 \\ \Delta z_c \end{Bmatrix} \tag{5.17}$$

6. The anchor chain angle changing rate on the oblique plane can be computed by Equation 5.13 and then the angle changing during this incremental embedment is:

$$\Delta\theta_{ac} = \frac{d\theta_{ac}}{d\hat{z}_c} \cdot \Delta z_c \tag{5.18}$$

7. After updating the chain angle by above equation, the new shackle tension in c-frame coordinate is determined by the following:

$$\vec{\mathrm{d}}_{ac} = \cos\theta_{ac}\vec{i}_c + 0\,\vec{j}_c - \sin\theta_{ac}\vec{k}_c \tag{5.19}$$

where $\vec{i}_c$, $\vec{j}_c$, and $\vec{k}_c$ are unit vector in c-frame coordinates. Then, the shackle tension can be converted to g-frame coordinate by:

$$\vec{\mathrm{d}}_{ag} = \left[R_{gc}\right]^{-1} \cdot \vec{\mathrm{d}}_{ac} \tag{5.20}$$

As occurs with drag embedment in a vertical plane (e.g. O'Neill et al. 1999), the anchor reaches an ultimate embedment depth when the centerline of the fluke is parallel to the ground surface and shackle tension converges to a maximum value. Actually, the procedure stated above involves some assumptions:

- The fluke is stationary as the chain changes its orientation until the anchor line tension at the padeye reaches its initial installation value T_{ai}.
- Anchor chain lies on an oblique plane.
- Not until the fluke resumes penetration does the tension at the shackle point corresponding increase.
- The fluke corrects its orientation automatically such that there always exists an angle θ_{fs} (fluke-shank angle) between the fluke and shackle tension in the inclined plane (Figure 5.4).
- The anchor stops traveling until its penetrating direction $\vec{\mathrm{d}}_f$ parallels direction of local in-plane coordinate x_c.

For the process described above, two variables with respect to out-of-plane loading will affect the trajectory and capacity of the anchor following partial failure of the mooring system, the first being the magnitude of the out-of-plane orientation angle of the chain at the mudline. The second is the initial installation depth z_i. For parametric studies, an installation penetration ratio R_p may be defined as follows:

$$R_p = \frac{z_i}{z_{\max}} \tag{5.21}$$

where z_{max} is the ultimate embedment depth under conditions of purely in-plane loading.

As an illustrative parametric study of drag anchor trajectory predictions for out-of-plane loading, we consider the case of drag embedment of an anchor with 12-m^2 anchor in a soft clay having zero strength at the mudline and a strength gradient k = 1.57 kPa/m. The anchor line in this example is a wire line with diameter b = 0.089 m. Pad-eye tension was related to soil strength at the pad-eye s_{ua} and fluke area A_f by the relationship $T_a = N_e\, s_{ua}\, A_f$, where is N_e is the anchor bearing factor. A bearing factor N_e = 5 was selected for this example. Trajectory predictions were performed for ϕ_{0g} = 30 degrees, and R_p was set to 0.25, 0.5, and 0.75. The anchor line angle at the mudline was maintained in a horizontal orientation at all stages of the simulation, ϕ_{0g} = 0.

Figure 5.6 shows the projections of the predicted trajectories onto the plane of intended loading (x_g–z_g plane) for the various cases. In all cases in which R_p is less than unity, continued embedment occurs following the occurrence of out-of-plane loading. However, the ultimate embedment depth, and therefore anchor load capacity, is

considerably less than what would develop had the anchor continued its trajectory in a vertical plane.

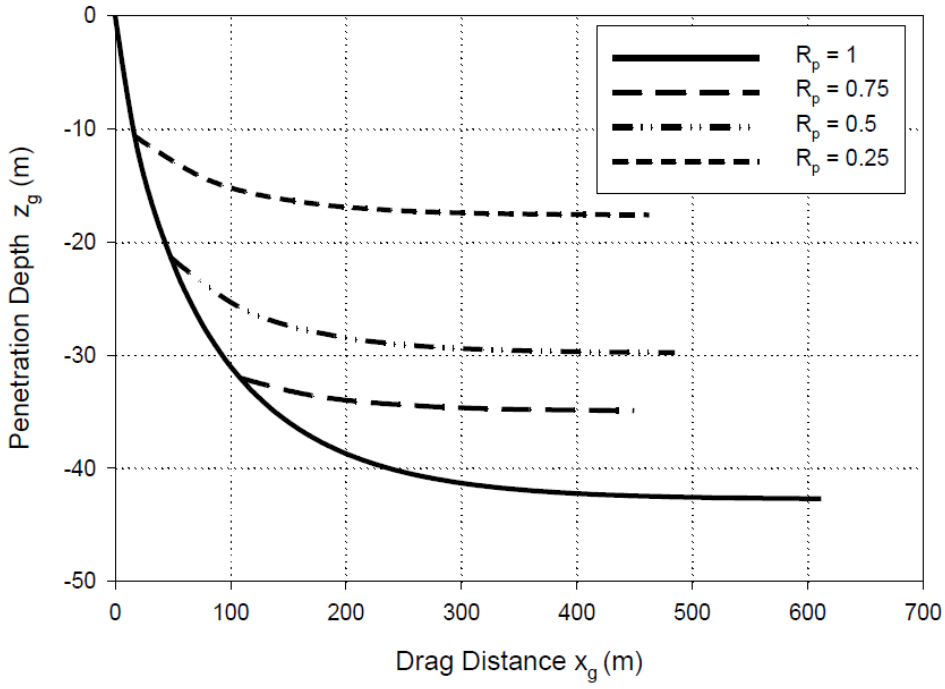

Figure 5.6 Predicted effect of out-of-plane loading on anchor trajectory

Figure 5.7 shows the anchor load capacities corresponding to the trajectory predictions in Figure 5.6. Consistent with the trajectory predictions, after partial failure of the mooring system, there is a modest gain in anchor load capacity under sustained dragging. However, the ultimate capacity is much less than that which would develop under continued dragging within the original vertical plane of intended loading.

Figure 5.8 shows the predicted trajectory in a plan view; i.e. a projection of the anchor trajectory onto the x_g–y_g plane. The out-of-plane path exhibits a slight curvature, with greater curvature corresponding to lower R_p values. The scale is exaggerated in the

y_g-direction, but a close inspection of the plot shows that the average angle of the deflected anchor path is roughly comparable to the out-of-plane anchor line angle ϕ_{0g} imposed at the mudline.

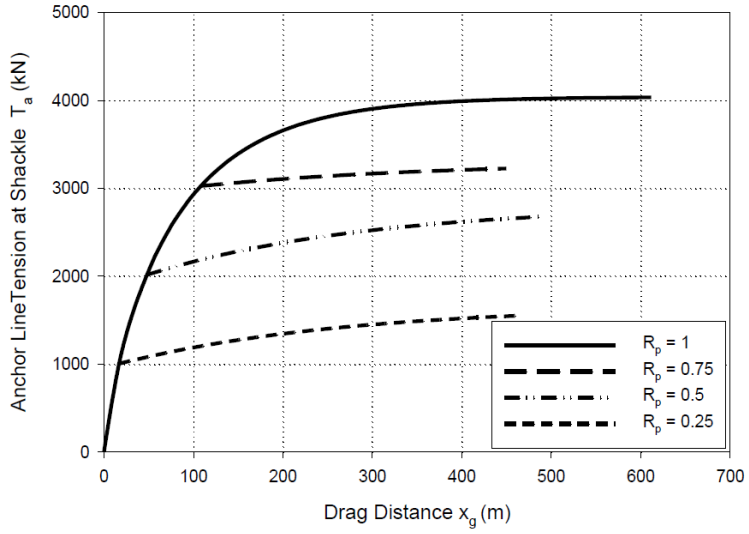

Figure 5.7 Predicted effect of out-of-plane loading on anchor load capacity

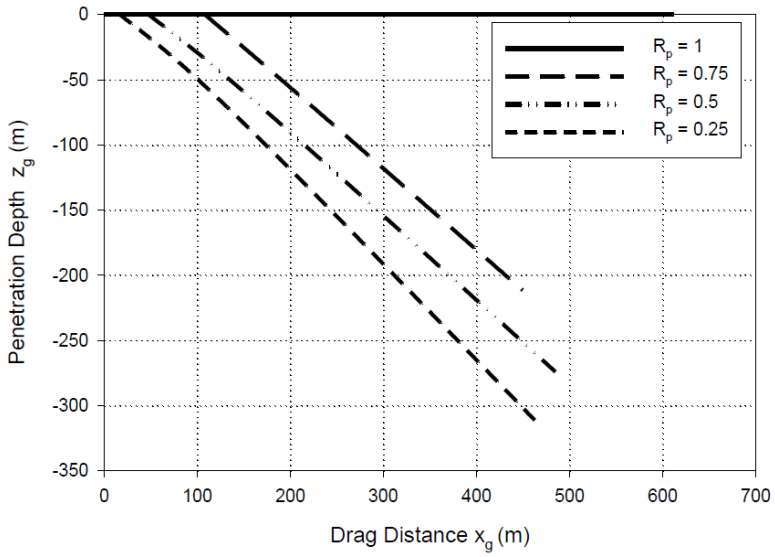

Figure 5.8 Predicted trajectory out of plane of intended loading

It is noted that Step 2 of the analysis procedure makes a fairly significant assumption in maintaining $\phi_{ag} = 0$ during the process which defines the re-configuration of the chain following a partial mooring failure. If, for example, ϕ_{ag} were actually greater than zero, the reduction in ultimate embedment depth and load capacity would be somewhat less. In the extreme (unlikely) case of ϕ_{ag} equaling ϕ_{0g}, the anchor would simply resume its trajectory in a vertical plane oriented an angle ϕ_{ag} from the x_g-axis, with no loss of ultimate embedment or capacity. Thus, from this perspective, the assumed behavior in Step 2 provides a conservative prediction of the effects of out-of-plane loading due to a partial mooring failure. A planned program of laboratory model tests are expected to shed light on the validity of the assumptions made in formulating the analysis procedure, particularly those in Step 2.

Figure 5.9 shows the trajectories of anchors in three-dimensional space. The dotted curve shows the in-plane motion trajectory for installation anchor ($R_p = 1$) and the other locates the trajectory subjecting lateral loadings for the ratio of penetration $R_p = 0.5$ on the oblique plane. On the other hand, the complete installation curve is totally on the vertical plane (x_g-z_g plane) and has no component in y_g direction. The projections of trajectories of two curves on the x_g-z_g and x_g-y_g planes are shown in Figure 5.6 and 5.8, respectively. One of the most important hypotheses is that the chain lies in an oblique plane; however, because the anchor is connected with the chain at the shackle point, it follows that the trajectory of anchor should be also on this plane (the color plane in Figure 5.9).

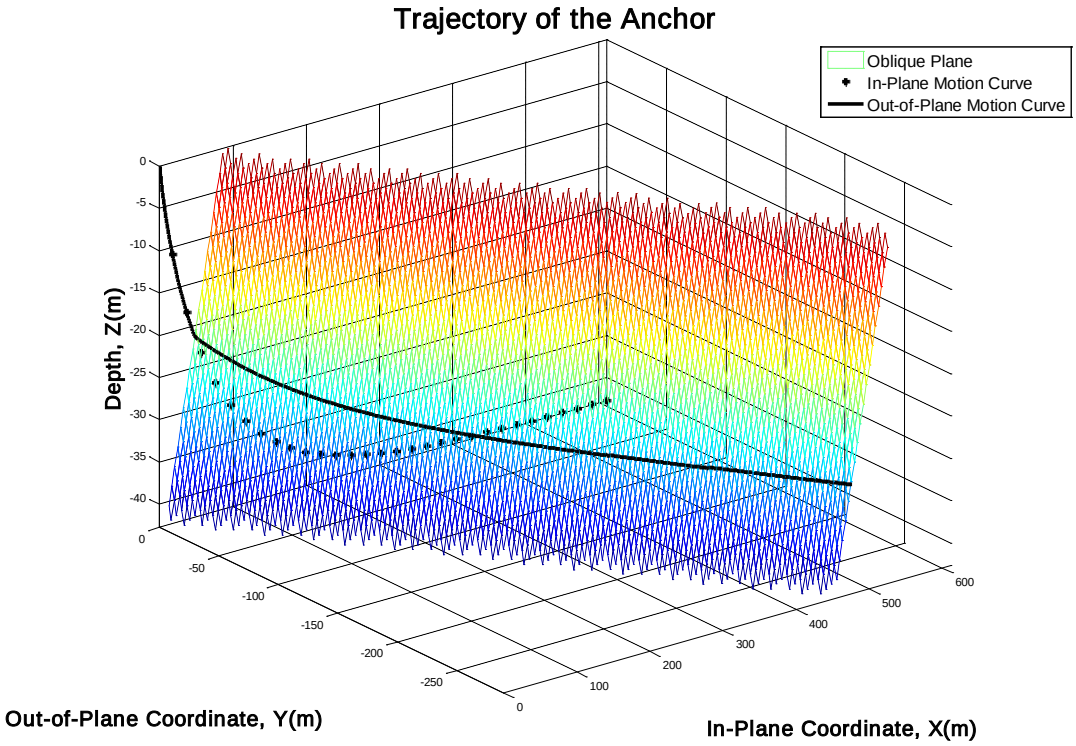

Figure 5.9 3-D trajectory of the anchor for $R_p = 0.5$

5.4 Out-of-Plane Anchor Chain Geometry

5.4.1 Modification of Chain Geometry Theory

Section 4.3.2 elucidates the chain geometry for the anchor subjecting in-plane loading in soil which its strength is proportional to the depth. The formula of geometry could be employed on an oblique plane, like the chain tension and rotation equations, but the transformation of coordinates is necessary. Form Equation 4.51, the geometry of chain on an oblique plane is:

$$x_c^* = \frac{1}{\sqrt{C_{2c}}} \ln \left[\frac{2C_{2c} + C_{1c} + 2\sqrt{C_{2c}\left(C_{2c} + C_{1c} + \theta_{0c}^2\right)}}{2C_{2c} z_c^* + C_{1c} + 2\sqrt{C_{2c}\left(C_{2c}\left(z_c^*\right)^2 + C_{1c} z_c^* + \theta_{0c}^2\right)}} \right] \tag{5.22}$$

where $z_c^* = \frac{z_c'}{D_c}$ $\quad$ $x_c^* = \frac{x_c'}{D_c}$

$$C_{1c} = \frac{2E_n N_c b}{T_a} S_{u0} D_c \qquad C_{2c} = \frac{E_n N_c b}{T_a} k_c D_c^2$$

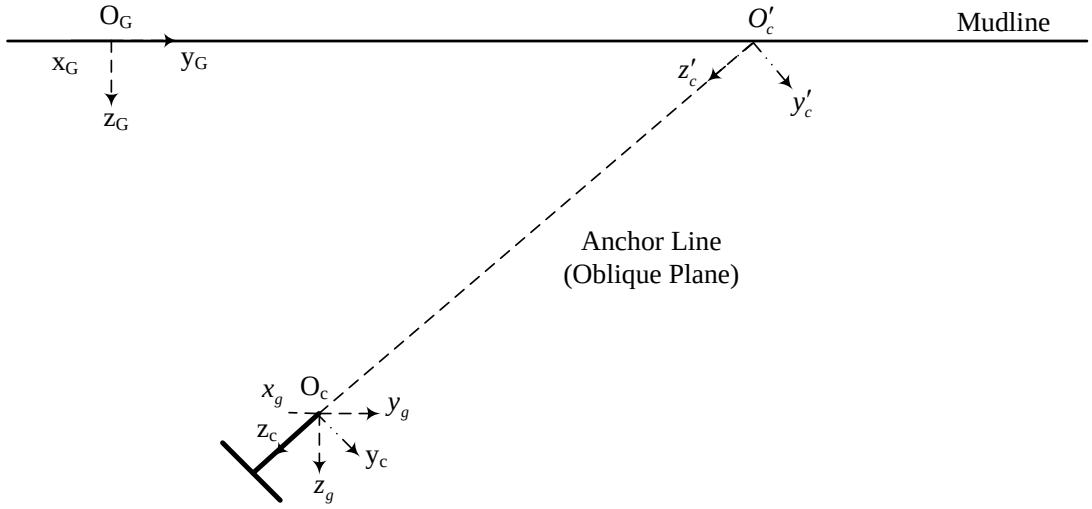

Figure 5.10 Transformation of coordinates for chain analysis

The chain geometry formula is described in the $x_c' - y_c' - z_c'$ coordinate system (Figure 5.10), the origin of which is O_c', where the direction of the x_c' axis is perpendicular to the page. The origin of the translated global coordinate system $x_G - y_G - z_G$ (O_G) is the point where the anchor starts to penetrate and it is also the reference point to describe the in-plane and out-of-plane anchor trajectory. It is emphasized that the shackle point is the reference point used to describe the location of the anchor. The point O_c represents the

location where the out-of-plane loading begins to apply on the anchor and it is also the origin of the $x_g - y_g - z_g$ system which is parallel to the global one. Therefore, there exists a translation relationship between $x_G - y_G - z_G$ and $x_g - y_g - z_g$ coordinates:

$$\begin{Bmatrix} x_g \\ y_g \\ z_g \end{Bmatrix} = \begin{Bmatrix} x_G - (x_a)_G \\ y_G - (y_a)_G \\ z_G - (z_a)_G \end{Bmatrix} \tag{5.23}$$

where $(x_a)_G$, $(y_a)_G$, and $(z_a)_G$ are the coordinates of the point O_c in translated global system.

As illustrated in Figure 3.16, the fluke is relatively easy to be spun (Figure 3.15) than rotated (Figure 3.14) while the aspect ratio R_{wf} is less than 3.2. Accordingly, it can be inferred that the fluke adjusts its orientation automatically to ready for travel on an oblique plane at the moment the out-of-plane loading applied. The $x_c - y_c - z_c$ system is the coordinate that has a rotational relationship with $x_g - y_g - z_g$:

$$\begin{Bmatrix} x_c \\ y_c \\ z_c \end{Bmatrix} = \left[R_{gc} \right] \begin{Bmatrix} x_g \\ y_g \\ z_g \end{Bmatrix} \tag{5.24}$$

where $\left[R_{gc} \right]$ is the rotational matrix and defined in Equation 5.4.

Finally, the $x_c' - y_c' - z_c'$ coordinate can be shifted from $x_c - y_c - z_c$ with the following relationship:

$$\begin{Bmatrix} x_c' \\ y_c' \\ z_c' \end{Bmatrix} = \begin{Bmatrix} x_c \\ y_c \\ z_c - D_c \end{Bmatrix} \tag{5.25}$$

where D_c is the distance between O_c and O_c'. It also can be determined by:

$$D_c = \frac{(z_a)_G}{\cos\delta_v} \tag{5.26}$$

Accordingly, the relation between $x_G - y_G - z_G$ and $x_c' - y_c' - z_c'$ coordinate can be described by $x_g - y_g - z_g$:

$$\begin{Bmatrix} x_c' \\ y_c' \\ z_c' + D_c \end{Bmatrix} = \begin{Bmatrix} x_c \\ y_c \\ z_c \end{Bmatrix} = \left[R_{gc}\right] \begin{Bmatrix} x_g \\ y_g \\ z_g \end{Bmatrix} = \left[R_{gc}\right] \begin{Bmatrix} x_G - (x_a)_G \\ y_G - (y_a)_G \\ z_G - (z_a)_G \end{Bmatrix} \tag{5.27}$$

The advantage of describing the chain geometry equation in $x_c' - y_c' - z_c'$ coordinate is that no component in y_c' direction is necessary. It could be regarded as an in-plane chain geometry in $x_c' - y_c' - z_c'$ space.

5.4.2 Numerical Computation Sequence for Anchor Chain Geometry

With the chain geometry equation in an oblique plane (Equation 5.22) and coordinates defined above, both the anchor trajectory and chain geometry can be presented together in a three-dimensional space by the following steps:

1. Sweep z_c^* from 0 to 1, obtain the normalized array $\{z_c^*\}$.
2. Substitute $\{z_c^*\}$ array into Equation 5.22 to obtain the normalized $\{x_c^*\}$ array.
3. The chain geometry coordinates in $x_c' - y_c' - z_c'$ space are:

   $\{x_c'\} = D_c\{x_c^*\}$ $\quad$ $\{y_c'\} = \{0\}$ $\quad$ $\{z_c'\} = D_c\{z_c^*\}$

4. By Equation 5.25, present geometry in $x_c - y_c - z_c$ space.

5. By Equation 5.24, present geometry in $x_g - y_g - z_g$ space.

6. By Equation 5.23, present geometry in $x_G - y_G - z_G$ space.

Figure 5.11 shows the anchor trajectory and chain geometry curves in a three-dimensional space based on the process described above. Similar to Figure 5.9, the dotted curve presents the result of installation to ultimate embedment (R_p = 1) and the solid black line is the trajectory for the case R_p = 0.5. Three green curves on the X_G—Z_G plane are the in-plane chain geometries which are determined by the procedures discussed in section 4.3.2; whereas, there are nine out-of-plane chain geometries plotted in red.

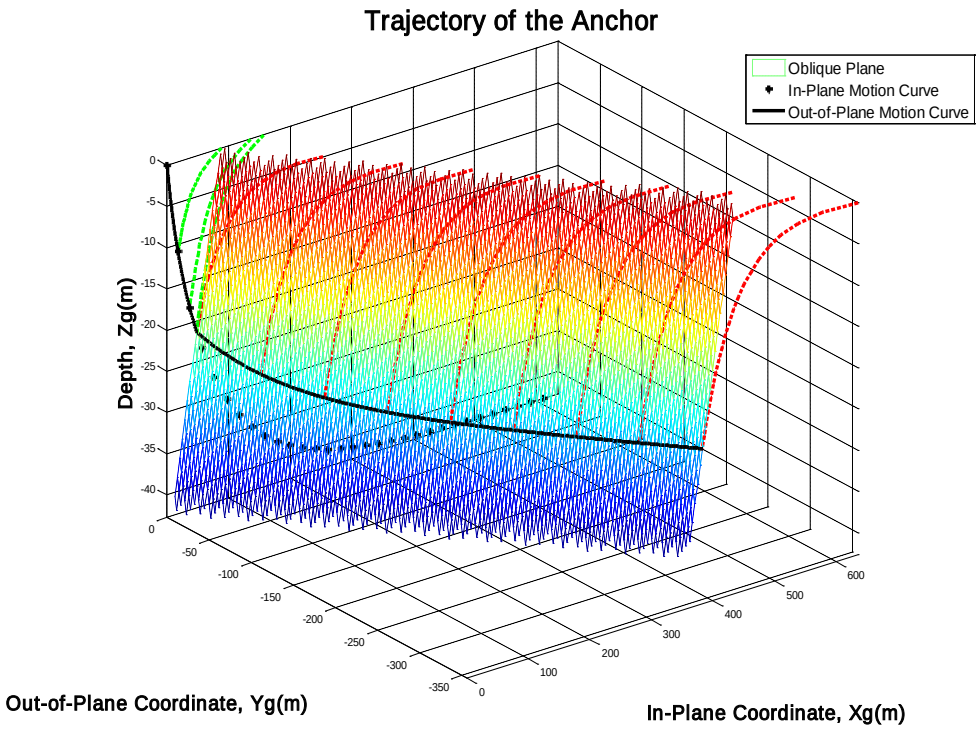

Figure 5.11 3-D anchor trajectory and chain geometry for R_p = 0.5

Based on the simulation methods stated in previous sections, both the out-of-plane anchor trajectory and chain geometry curves lie in the oblique plane. In addition, at the point at which out-of-plane loading applies on the anchor, the chain geometry changes its orientation first (from third green curve to first red one) and then the anchor starts to travel in out-of-plane direction. The following two figures elucidate the projections of anchor trajectories and chain geometries on X_G—Z_G plane and Y_G—Z_G plane. The plot in Figure 5.13 helps to clarify the change in chain geometry from the in-plane to the out-of-plane condition.

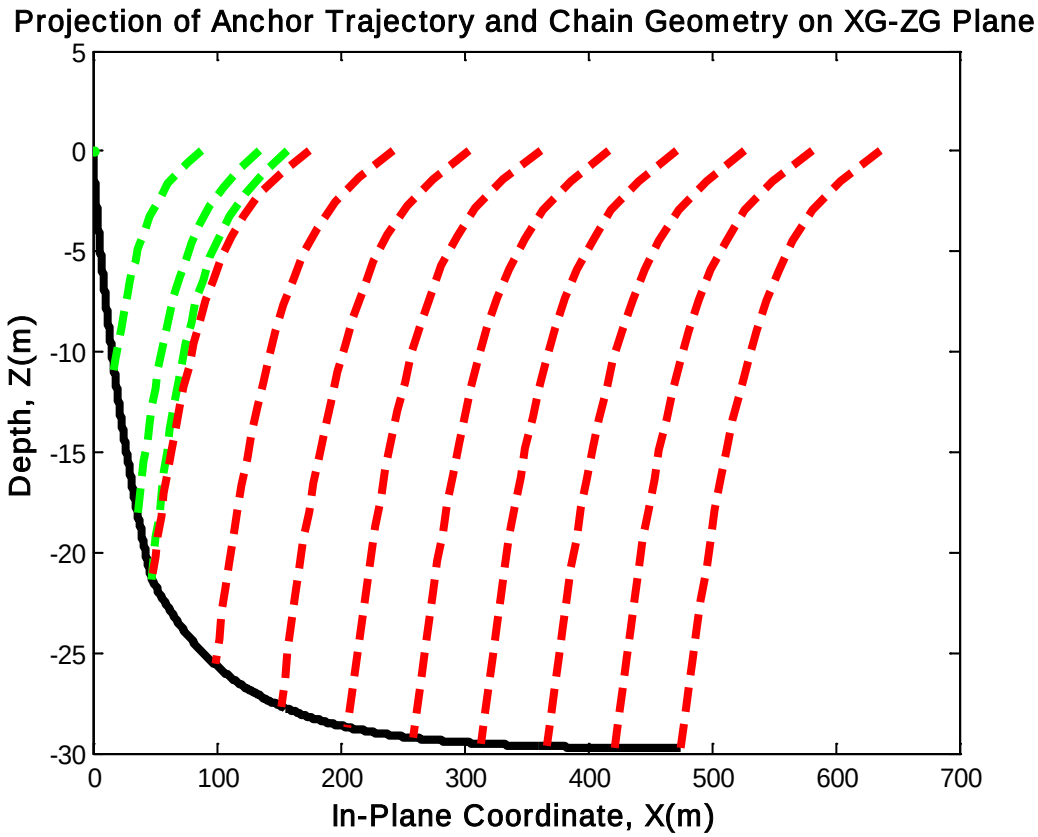

Figure 5.12 Projection of anchor trajectory and chain geometry on X_G—Z_G plane

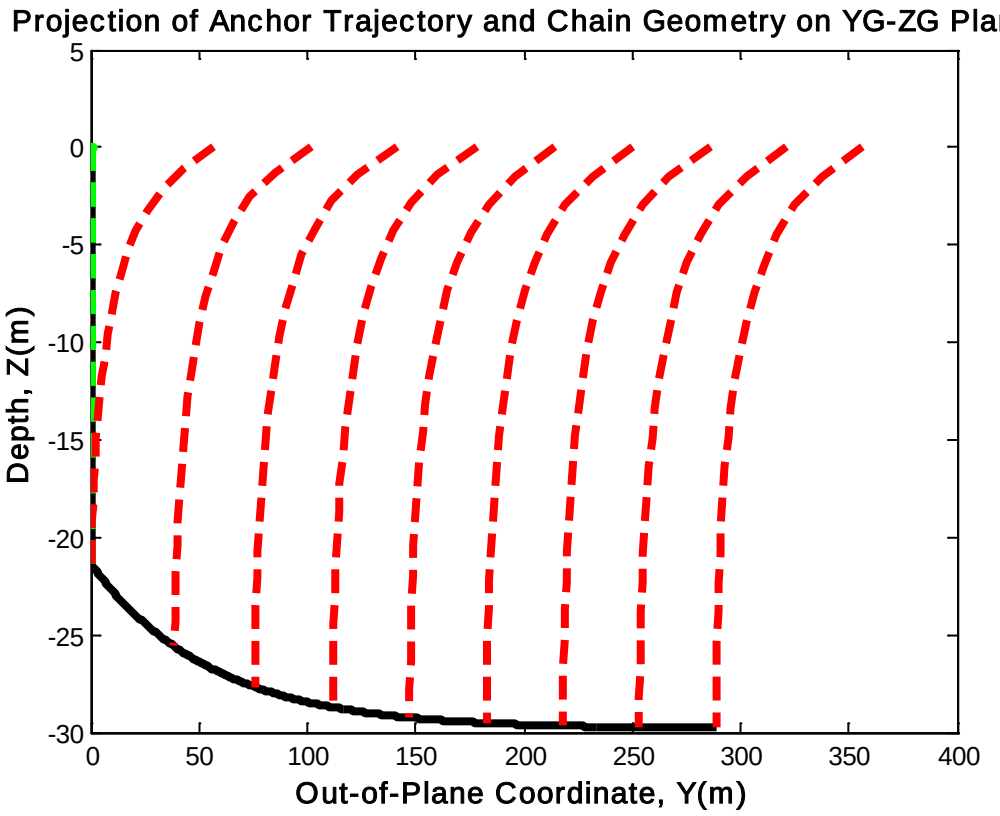

Figure 5.13 Projection of anchor trajectory and chain geometry on Y_G—Z_G plane

CHAPTER VI

STABILITY ASSESSMENT OF SPUDCAN FOUNDATION

6.1 General

Spudcan foundation behavior has significant influence on both the safety and the operation of a jack-up unit. Based on the procedure recommended by Technical & Research Bulletin 5-5A Guidelines for Site Specific Assessment of Mobile Jack-Up Units (SNAME, 2002), there are three steps in the assessment of safety and stability of a jack-up unit. A pinned foundation condition, where no rotational stiffness is considered, is assumed in the step 1 (preloading check) and step 2a (bearing capacity check). Step 2b (bearing capacity check) allows the use of linear translational and of non-linear rotational stiffness and may lead to less conservative results than step 1 and step 2a. The initial stress state corresponding to applied environmental forces should be inside of the plastic yielding surface both for the pinned foundation condition and the moment-resisting foundation condition. An initial stress state located outside of the plastic yielding surface is inadmissible and will not occur in a load and resistance factor design (LRFD). However, it may occur if a short return period is considered in the analysis and the jack-up unit may tilt dramatically and ultimately lead to failure. The step 3 in analysis is the displacement check for the spudcan foundation. It should be noted that the consideration of the suction problem of windward leg spudcan foundation is necessary and the settlement difference between the windward leg and the leeward leg may be a critical issue when the jack-up unit is subjected to a severe storm.

6.2 Preloading Assessment

The analysis considers that a jack-up unit will be preloaded to Storm Elevated Weight before drilling operations; therefore, the prediction of footing penetration during preloading is the first step of spudcan foundation assessment. For conventional foundation analysis, the spudcan (Figure 6.1) could be modeled as a flat circular foundation and the equivalent diameter is determined from the cross section area of the actual spudcan in contact with the seabed surface, i.e., the uppermost part of bearing area in contact with soil.

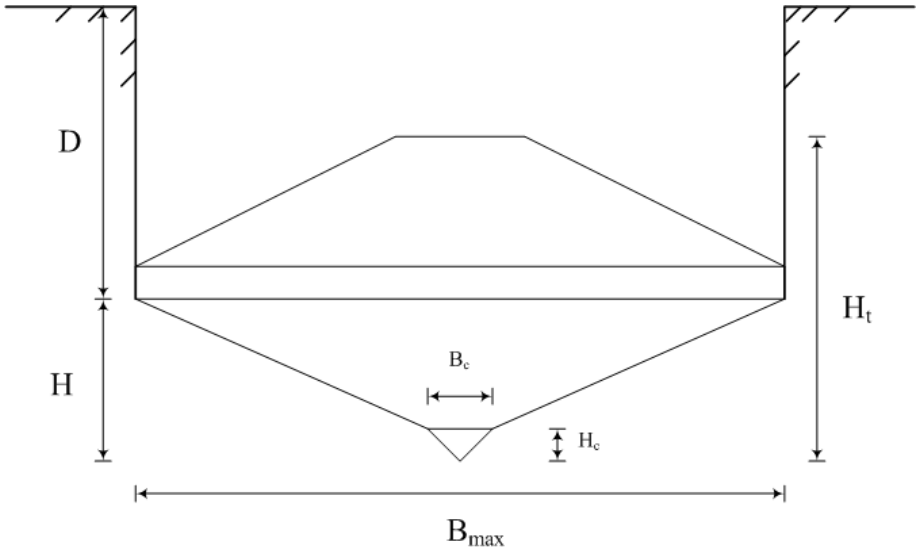

Figure 6.1 Typical spudcan geometries

However, the bearing capacity is mainly affected by the actual contact area and soil strength. The bearing capacity increases proportionally with the square of the equivalent of diameter when the spudacan foundation is partially penetrated. The formulas of determining bearing capacity for foundation in clay or sand soil are shown as follows:

Clay: $F_v = (C_u \cdot N_c \cdot S_c \cdot d_c + p_0')A$ (6.1)

Sand: $F_v = (0.5 \cdot \gamma' \cdot B \cdot N_\gamma \cdot S_\gamma \cdot d_\gamma + p_0' \cdot N_q \cdot S_q \cdot d_q)A$ (6.2)

It is recommended that the undrained shear strength C_u is taken as the strength at the penetration depth plus a one-fourth of equivalent diameter ($D + B/4$). The depth of spudcan penetration is considered as the depth to the maximum spudcan bearing area; therefore, the value of D will be less than or equal to zero for the case of partial penetration. Figures 6.2 and 6.3 are the plots of bearing capacity versus spudcan tip depth for the base case analysis considered in this study (Table 6.1) in clay and sand soils.

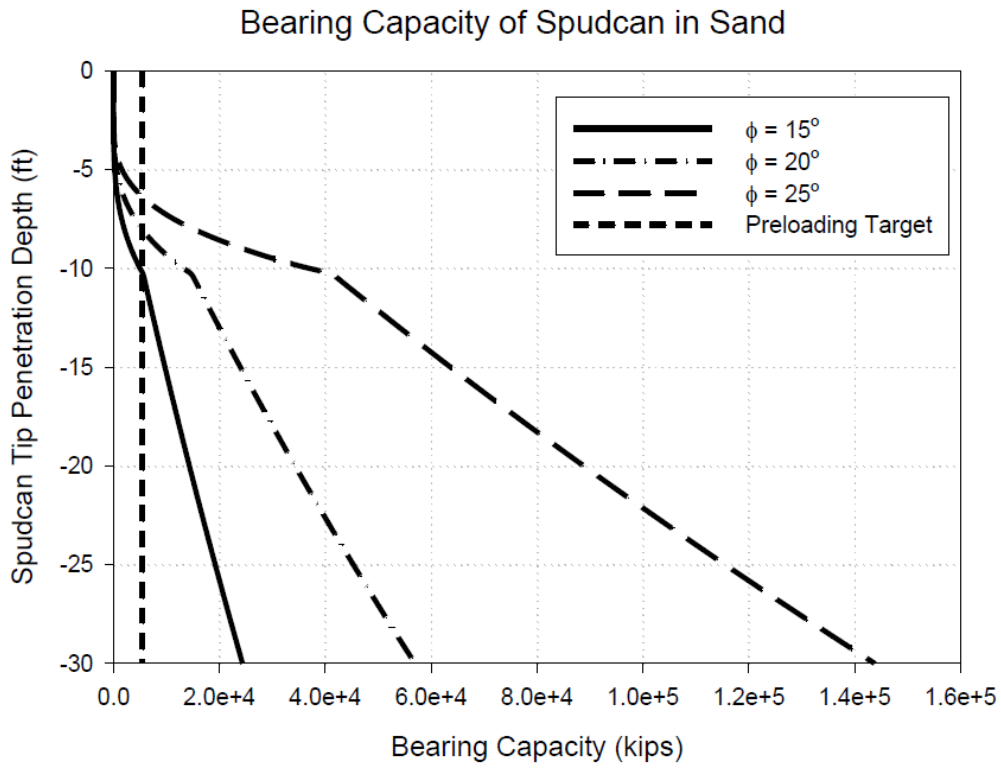

Figure 6.2 Prediction of penetration during preloading in sand

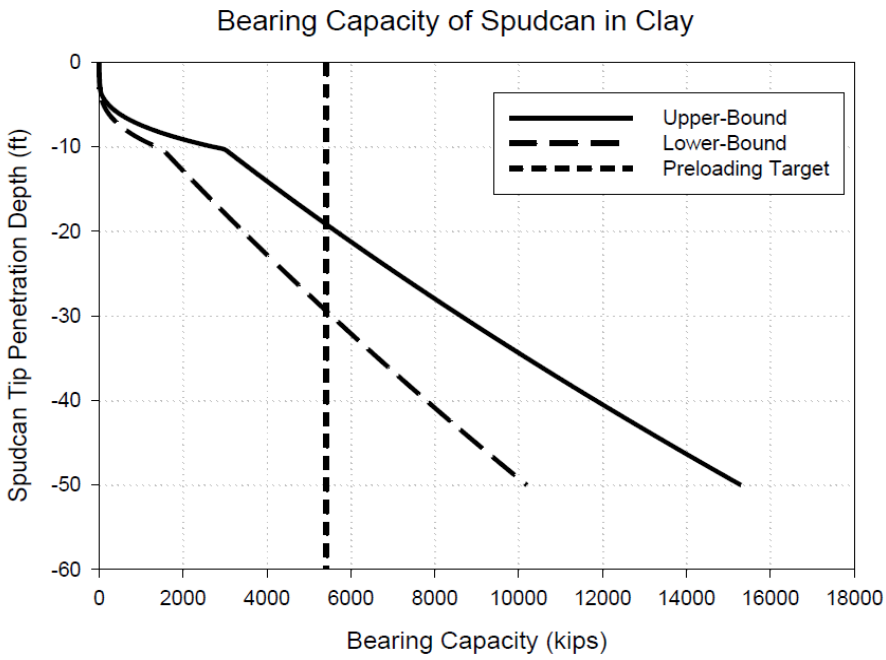

Figure 6.3 Prediction of penetration during preloading in clay

The shape of bearing capacity curve is similar to a concave cubic curve when the depth is less than the high H (10.3 ft) from tip and maximum bearing area of spudcan, because the actual contact area increases proportionally with the square of spudcan tip depth. On the other hand, it is linear when the tip penetration depth is greater than H because soil strength increases linearly with the depth. Compared with Figure 6.3, the preloading penetration depth in sand soil for $\phi = 15^0$ (10.2 ft) is much shallower than the case in clay regardless of whether in upper-bound (19.2 ft) or lower-bound (29.4 ft) undrained shear strength is considered. Sandy soil therefore offers much more bearing capacity than that from clay soil, even when a "Very Loose" is considered ($\phi = 15^0$, Table 6.2). It is suggested that the value of friction angle from laboratory triaxial test be

used in the analysis but a reduction is necessary. Equation 6.3 presents the relation between the friction angle from the triaxial test and the value used in analysis:

$$\phi_{analysis} = \phi_{triaxial} - 5^0 \tag{6.3}$$

When determining the bearing capacity in clay soil, the problem of soil back flow over the footing should be considered. The bearing capacity must be reduced by the weight of the collapsed soil mass as shown by Equation 6.4:

$$V_{L0} = F_V - F_0' \cdot A + \gamma' \cdot V \tag{6.4}$$

F_0' is the effective overburden pressure caused by the back flow soil mass at the depth uppermost part of bearing area and the V is the volume of soil replaced by the spudcan. It should be noted that the term $-F_0' \cdot A + \gamma' \cdot V$ must always be considered together. Various methods are used to evaluate the stability of the foundation hole. The common approach is to calculate the stability number. Equation 6.5 is the formula suggested by Britto and Kusakabe (1992) to calculate the stability number N_s:

$$N_s = \frac{\gamma' \cdot D}{S_u} \tag{6.5}$$

where S_u is the undrained shear strength at the depth D/2 below the mudline. The equation shown above also can be used to determine the critical penetration depth of soil back flow:

$$D_{cri} = \frac{S_u \cdot N_s}{\gamma'} \tag{6.6}$$

Hossain et al. (1975) suggested a stability number less than 6 for the stability of the foundation hole.

Table 6.1 Base case condition for spudcan capacity and penetration predictions

Spudcan Geometry: Maximum diameter of spudcan, $B_{\max} = 46$ ft High from tip and max bearing area of spudcan, $H = 10.3$ ft Total high of Spudcan, $H_t = 20.6$ ft Ratio of cone diameter to spudcan maximum diameter, $R_D = \frac{B_c}{B_{\max}} = \frac{1}{7}$ Ratio of cone high to H, $R_H = \frac{H_c}{H} = \frac{1}{3}$
Soil Properties: <u>Clay</u> Lower Bound Mudline Strength, $S_{u0} = 50$ psf Lower Bound Soil Strength Gradient, $k = 7$ psf/ft Upper Bound Mudline Strength, $S_{u0} = 120$ psf Upper Bound Soil Strength Gradient, $k = 12$ psf/ft Plastic Index, $PI = 20$ Unit Weight of Soil, $\gamma = 120$ pcf <u>Sand</u> Friction angle, $\phi = 15^o, 20^o, 25^o$ Poisson Ratio, $\upsilon = 0.3$ Unit Weight of Soil, $\gamma = 120$ pcf
Physical Specification: Storm Elevated Weight, $W_J = 16250$ kips Dead Load of Jack-Up Unit, $W_D = 6000$ kips
Environmental Force: Vertical Direction, $Q_v = 1250$ kips Horizontal Direction, $Q_h = 325$ kips Moment, $Q_m = 15000$ kips-ft

Table 6.2 Friction angle for cohesionless siliceous soil (SNAME, 2002)

Density	Soil Description	ϕ^o
Very Loose Loose Medium	Sand Sand-Silt Silt	15
Loose Medium Dense	Sand Sand-Silt Silt	20
Medium Dense	Sand Sand-Silt	25
Dense Very Dense	Sand Sand-Silt	30
Dense Very Dense	Gravel Sand	35

6.3 Bearing Capacity Assessment—Pinned Condition Footing

The vertical bearing capacity of foundation F_V is reduced when a horizontal force or moment is applied. The moment loading is neglected in the analysis when the footing is considered to be pinned. In general, the formulae suggested by Vesic and Brinch Hansen (Bowles, 1996) are used to evaluate the bearing capacity of a spudcan foundation subjected horizontal loading but they are only applicable to shallow foundations. The contribution of lateral soil resistance is a difficult issue for several reasons:

1. Some seams may exist in weak soils located below the spudcan foundation.
2. The contact area between the spudcan and soil may not be certain because of the shape of spudcan.
3. The shear strength of soil surrounding the foundation may be significantly reduced due to the disturbance during the installation.

Based on the reasons stated above, the influence of lateral soil resistance on vertical projected embedded area can either be ignored or assessed conservatively.

6.3.1 Vertical-horizontal Bearing Capacity Interaction Envelope for Footings in Sand

The equation of ultimate bearing capacity of shallow foundation with inclined loading in sand is shown as follows:

$$F_{vh} = (0.5 \cdot \gamma' \cdot B \cdot N_\gamma \cdot S_\gamma \cdot d_\gamma \cdot i_\gamma + p_0' \cdot N_q \cdot S_q \cdot d_q \cdot i_q) A \tag{6.7}$$

where F_{vh} is the vertical bearing capacity in combination with horizontal loading and i_γ and i_q are the inclination factors which presented in Equation 6.8 and 6.9:

$$i_\gamma = [1 - (\frac{F_h}{F_{vh}})^*]^{m+1} \tag{6.8}$$

$$i_q = [1 - (\frac{F_h}{F_{vh}})^*]^m \tag{6.9}$$

For a circular footing, m can be taken as 1.5. These two equations can be explained by introducing the inclination factors recommended by Meyerhof (Bowles, 1996). It is clear that, from Figure 6.4, and Equations 6.10 and 6.11, the conception of $(\frac{F_h}{F_{vh}})^*$ is the orientation of resultant force corresponding to the vertical loading.

$$i_\gamma = \begin{cases} (1 - \frac{\theta^o}{\phi^o})^2 & \phi > 0 \\ 0 & \phi = 0 \end{cases} \tag{6.10}$$

$$i_q = (1 - \frac{\theta^o}{90^o})^2 \tag{6.11}$$

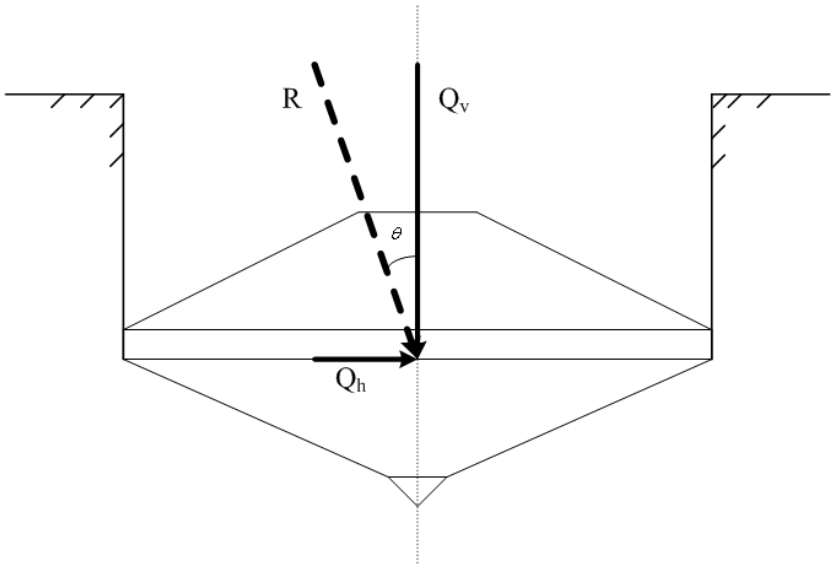

Figure 6.4 Spudcan footing with environmental vertical and horizontal force

The dashed arrow R in above figure is the resultant force and θ is the inclination. It is noted that the inclination factors should be greater than zero, i.e., the inclination angle θ should be less than friction angle ϕ. By substituting various values of $(\frac{F_h}{F_{vh}})^*$ from zero to one, F_h^* can be determined with different F_v^*. The corrected horizontal bearing capacity F_h can be determined by the following:

$$F_h = F_h^* + 0.5 \cdot \gamma' \cdot (k_p - k_a) \cdot [D + (D + H)] \cdot A_s \tag{6.12}$$

where k_p and k_a are the passive and active earth pressure coefficients, and A_s is the spudcan laterally projected embedded area. From Figure 6.5, vertical-horizontal bearing capacity interaction envelope, the environmental force (triangle point) is inside the interaction surface. Based on plasticity theory, the foundation against is secure this environmental loading. A load condition located outside of the interaction envelope is

not allowable. It may be suspected that the envelope of soil with lower friction angle is larger than that with higher friction angle. Indeed, it is difficult to believe that stronger soil offer less bearing capacity. However, the penetration depth D and the lateral projected area A_s are smaller for higher friction angle soil and the horizontal bearing capacity is mainly affected by these two terms from Equation 6.12. The spudcan tip depths for the cases shown in Figure 6.2, are 10.2 ft, 8ft, and 6.3ft for the cases $\phi = 15^o, 20^o$, and 25^o respectively. This result indicates that a shallower spudcan penetration depth significantly reduces the size of the smaller the normalized bearing capacity envelope (Figure 6.6) will be (API RP2A 1989), irrespective of friction angle.

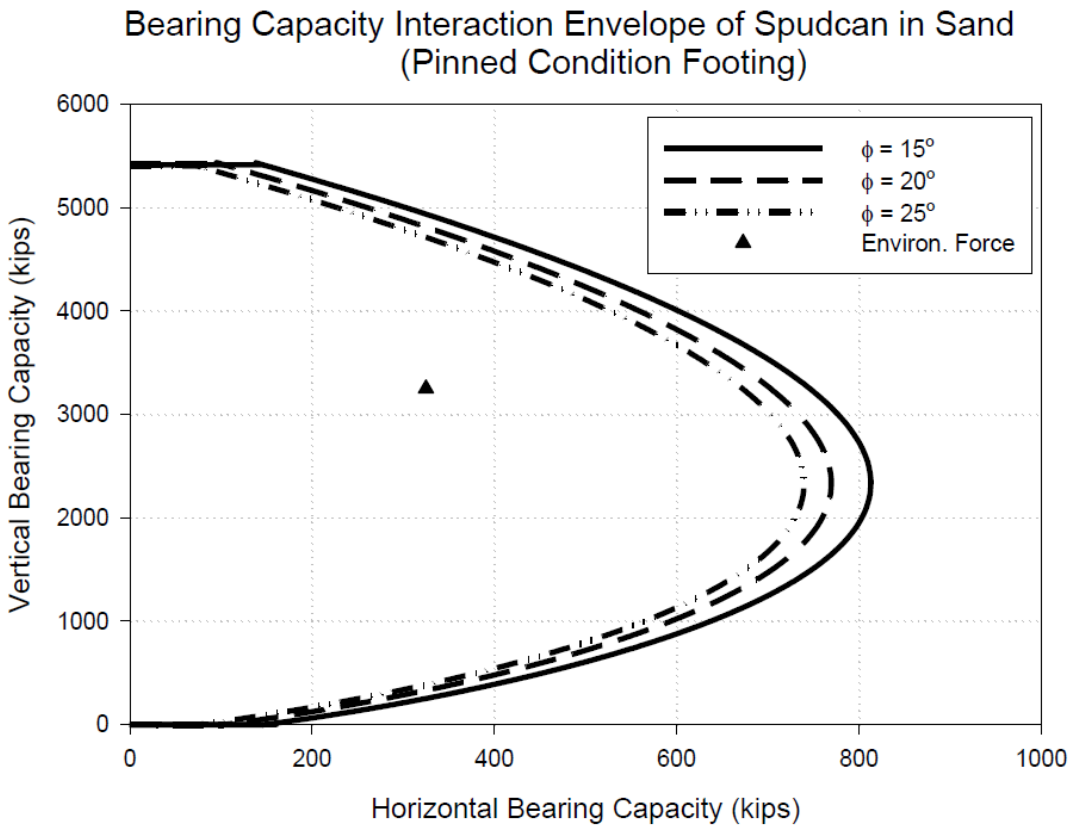

Figure 6.5 Vertical-horizontal loading interaction envelope of spudcan in sand

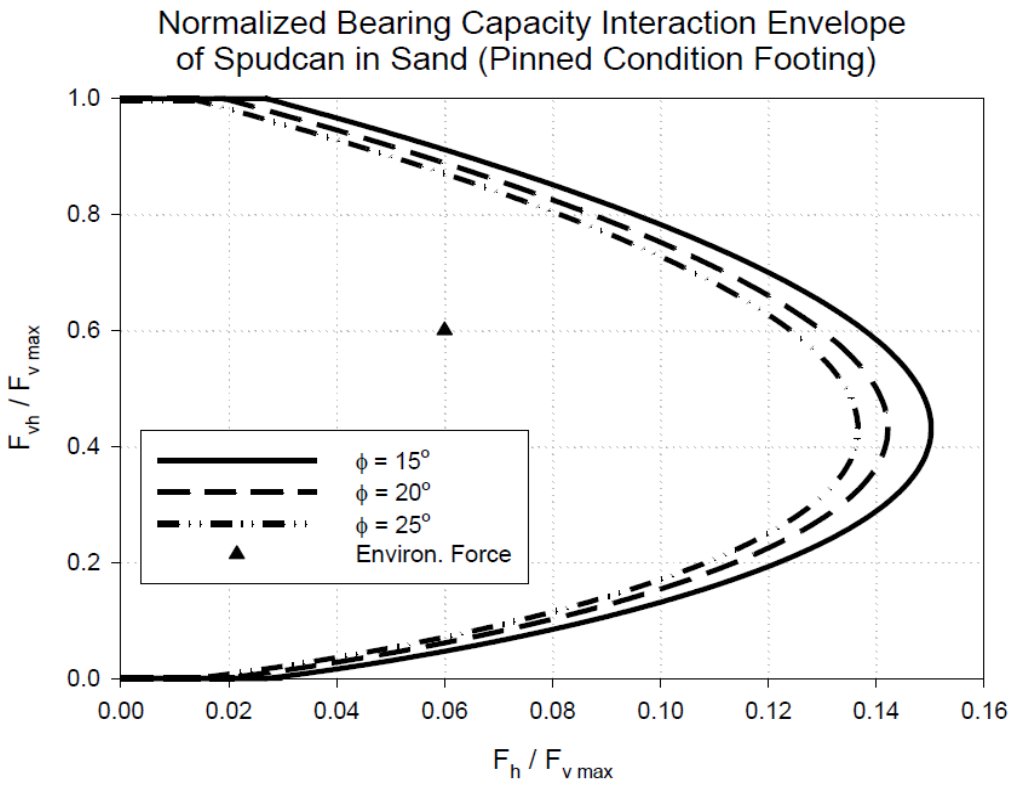

Figure 6.6 Normalized vertical-horizontal loading interaction envelope of spudcan in sand

6.3.2 Vertical-Horizontal Bearing Capacity Interaction Envelope for Footings in Clay

The equation of ultimate bearing capacity of a shallow foundation subjected to inclined loading in clay is follows:

$$F_{vh} = (C_u \cdot N_c \cdot S_c \cdot d_c \cdot i_c + p_0' \cdot N_q \cdot S_q \cdot d_q \cdot i_q) A \tag{6.13}$$

where N_q, S_q, and d_q equal to one while the friction angle $\phi = 0$. The inclination factors i_c and i_q are defined by Equations 6.14 and 6.15:

$$i_c = 1 - \frac{1.5 F_h^*}{N_c \cdot A \cdot C_u} \tag{6.14}$$

$$i_q = [1 - \frac{F_h^*}{F_{vh}}]^{1.5} \tag{6.15}$$

By substituting various F_{vh} values from zero to maximum vertical bearing capacity (one third of preloading target), the F_h^* can be determined by solving a cubic equation presented as Equation 6.16:

$$a_1(F_h^*)^3 + a_2(F_h^*)^2 + a_3(F_h^*) + a_4 = 0 \tag{6.16}$$

where $a_1 = (P_0' \cdot A)^2$

$$a_2 = 2.25 \cdot S_c^2 \cdot d_c^2 \cdot F_{vh}^3 - 3 \cdot F_{vh} \cdot (P_0' \cdot A)^2$$

$$a_3 = 3 \cdot S_c \cdot d_c \cdot \alpha \cdot F_{vh}^2 + 3 \cdot F_{vh}^2 \cdot (P_0' \cdot A)^2$$

$$a_4 = [\alpha^2 - (P_0' \cdot A)^2] \cdot F_{vh}^3$$

$$\alpha = F_{vh} - A \cdot N_c \cdot C_u \cdot S_c \cdot d_c$$

Due to the restriction that inclination factors must be positive, the values of F_h^* calculated from the cubic equation may not be the solutions of the interaction envelope. In other words, the constraints $F_h^* \le F_{vh}$ and $F_h^* \le \frac{2}{3} N_c \cdot A \cdot C_u$ must be satisfied. The corrected horizontal bearing capacity F_h can be determined by the Equation 6.17:

$$F_h = F_h^* + (C_{u0} + C_{u1}) \cdot A_s \tag{6.17}$$

where C_{u0} and C_{u1} are the undrained shear strength at maximum bearing area and spudcan tip. It may be estimated conservatively from Equation 6.18 that if the

environmental vertical force Q_v is less than half of vertical foundation bearing capacity F_v, the following equation applies:

$$F_h = C_{u0} \cdot A + (C_{u0} + C_{u1}) \cdot A_s \tag{6.18}$$

Figure 6.7 is the result of bearing capacity interaction envelope for the lower-bound strength clay (Table 6.1). It is obvious that all solutions of cubic equation are satisfied with the limitation of inclination factor i_c ($F_h^* \le \frac{2}{3} N_c \cdot A \cdot C_u$); however, only upper portion of them conform to the restriction of i_q ($F_h^* \le F_{vh}$).

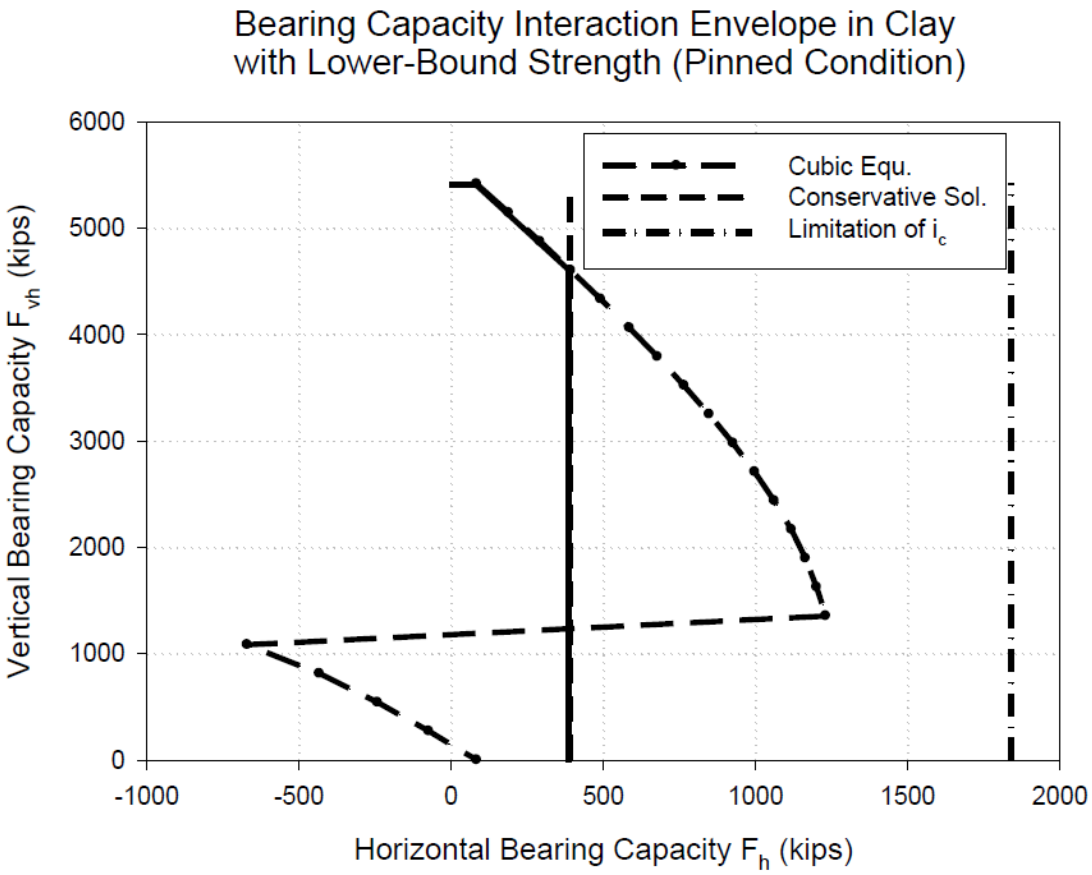

Figure 6.7 Three vertical-horizontal loading interaction criterion of spudcan in clay

The conservative solution (Equation 6.18) is also shown in the Figure 6.7 and the values from it are significantly smaller than those from the cubic equation. The bold solid line in the figure presents the vertical-horizontal bearing capacity interaction envelope when the conservative solution and the limitation of inclination factors are considered.

Figures 6.8 and 6.9 show the original and normalized vertical-horizontal bearing capacity interaction envelope in clay. The spudcan tip depths of two different shear strengths, upper-bound and lower-bound, are 19.2 ft and 29.4 ft. In contrast with the normalized interaction envelope in sand (Figure 6.6), the envelope of deeper penetrating depth in clay is smaller than that of shallower penetrating depth in Figure 6.9.

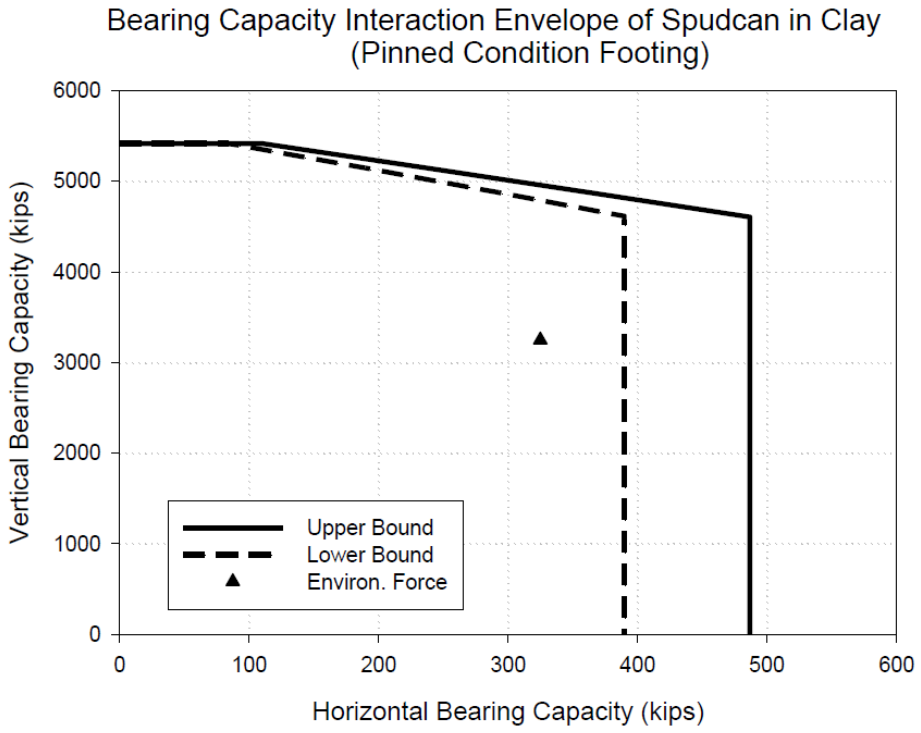

Figure 6.8 Vertical-horizontal loading interaction envelope of spudcan in clay

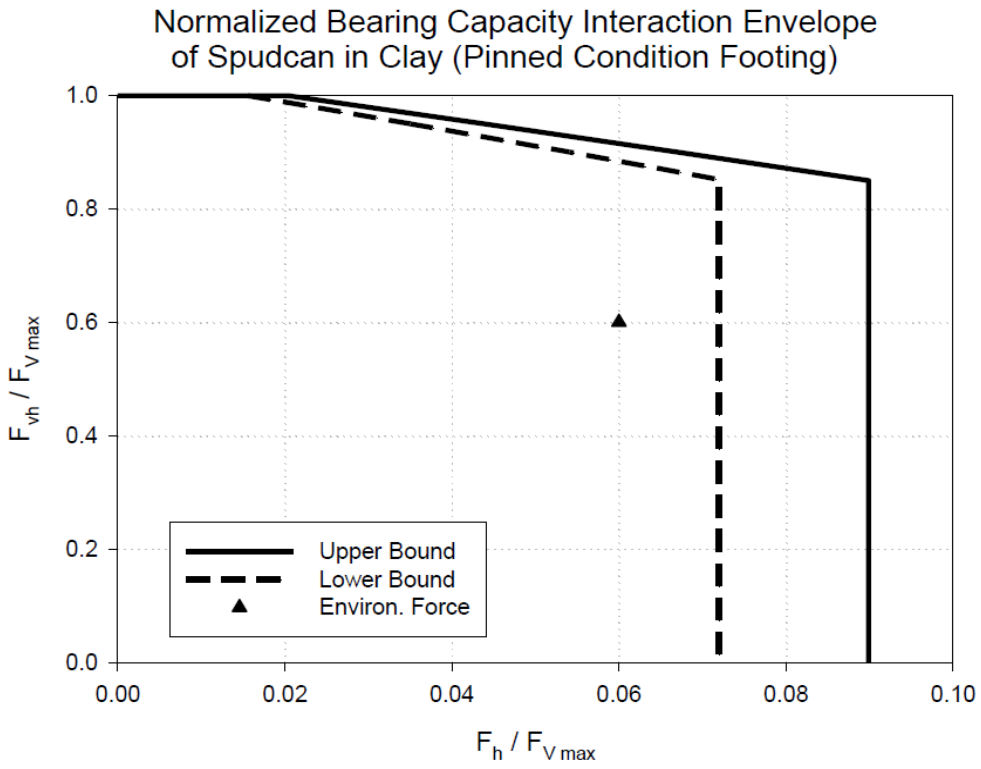

Figure 6.9 Normalized vertical-horizontal loading interaction envelope of spudcan in clay

6.4 Bearing Capacity Assessment—with Vertical, Horizontal, and Rotational Soil Spring

As discussed earlier, the effect of soil rotational fixity is not included in the checking procedure, but it contributes to the stability of spudcan foundation. The interactions of vertical, horizontal, and rotational loadings are modeled based on the plasticity theory (Van Langen 1993, Martin et al. 2001). Similar to the assumption of pinned condition footing, the situation of when the external force is located outside of the yielding surface is not acceptable. The issue of how to present the safety of the foundation may be

important while the external force is inside of yielding surface; hence, the concept of the factor of safety will be introduced in this assessment.

6.4.1 Ultimate Vertical-Horizontal-Rotational Bearing Capacity Assessment in Sand Using SNAME Yield Function

The yield function for shallowly embedded spudcan footings recommended by SNAME is shown as follows:

$$f = (\frac{Q_m}{M_0})^2 + (\frac{Q_h}{H_0})^2 - 16(\frac{Q_v}{V_0})^2(1-\frac{Q_v}{V_0})\left|1-\frac{Q_v}{V_0}\right| \tag{6.19}$$

where V_0 is the vertical bearing capacity due to preloading and H_0 and M_0 are defined as follows:

$$H_0 = 0.12V_0 \tag{6.20}$$

$$M_0 = 0.075B \cdot V_0 \tag{6.21}$$

Figures 6.10 and Figure 6.11 show the yielding surface and the contour of the sand with friction angle $\phi = 15^o$ and the intersection of three black lines is the position of the environmental forces. It can be observed that the location of the external forces is inside but very close to the yielding surface. Figure 6.12 through Figure 6.15 illustrate the yield surfaces and contours for the cases $\phi = 20^o$ and $\phi = 25^o$. Unlike the case $\phi = 15^o$, the environmental forces are located outside of the yield surface. It can be observed from three contour figures that the ranges of them are identical but the altitude of the surface of the friction angle $\phi = 15^o$ is higher than others, i.e., the vertical and horizontal maximum bearing capacities of three cases are the same but the lower friction angle sand

offers higher moment bearing capacity. This phenomenon can be explained by checking Equations 6.20 and 6.21. Since the preloading target is unique, V_0 and H_0 will not change with different friction angle; nevertheless, the maximum moment bearing capacity M_0 is affected by the effective spudcan contact diameter B and it will increase with the spudcan tip penetration depth while the spudcan is partially penetrated. Recalling Figure 6.2 and the analysis of the preloading assessment, the spudcan tip penetration depths are 10.2 ft, 8 ft, and 6.3 ft for the cases of $\phi = 15^o$, $\phi = 20^o$, and $\phi = 25^o$ respectively and all of them are less than the height from tip and max bearing area of spudcan $H = 10.3$ ft (partial penetration). A deeper tip penetration depth leads to a wider effective contact diameter B (45.4 ft, 32.9ft, and 23.3 ft). Therefore, the moment bearing capacity for a lower friction angle is larger than that for a higher friction angle when spudcan footing is partially penetrated in sand. It also can be inferred that the size of yielding surface at a certain preloading will not change with soil properties for fully a penetrated spudcan.

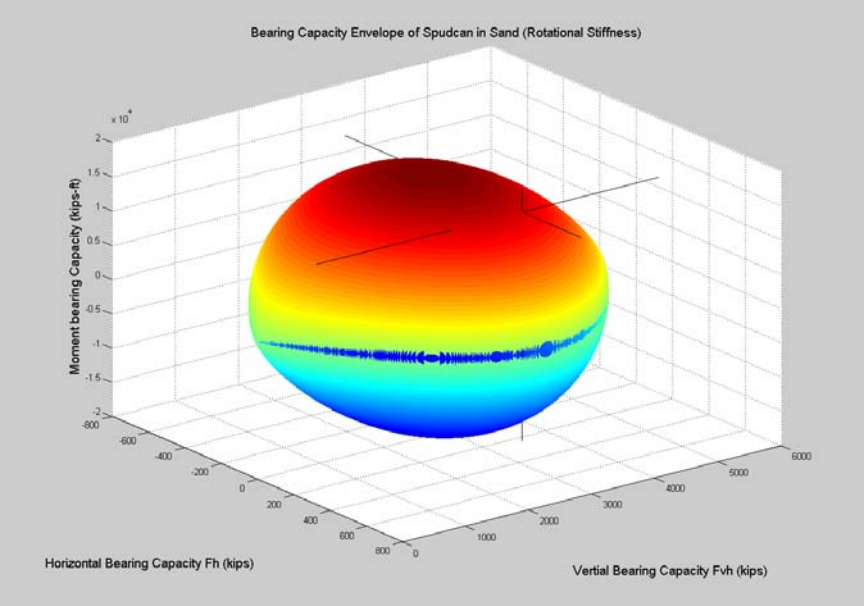

Figure 6.10 Vertical-horizontal-rotational loading interaction yield surface of spudcan in sand ($\phi = 15^o$)

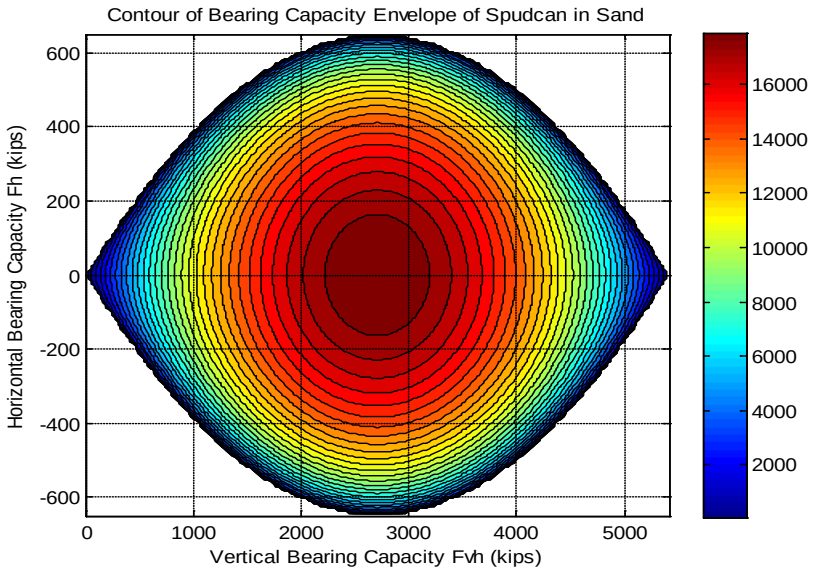

Figure 6.11 Contour of vertical-horizontal-rotational loading of spudcan in sand ($\phi = 15^o$)

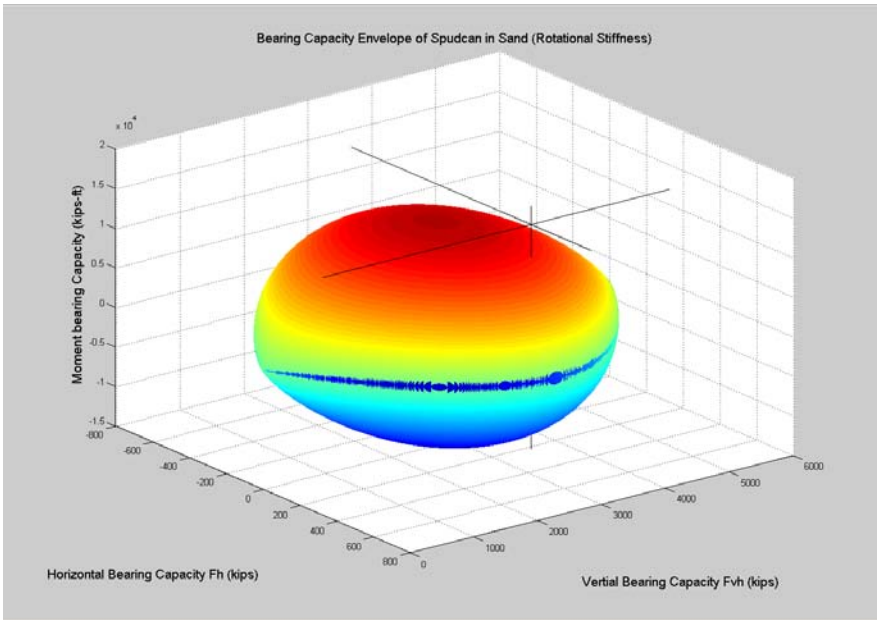

Figure 6.12 Vertical-horizontal-rotational loading interaction yield surface of spudcan in sand ($\phi = 20^o$)

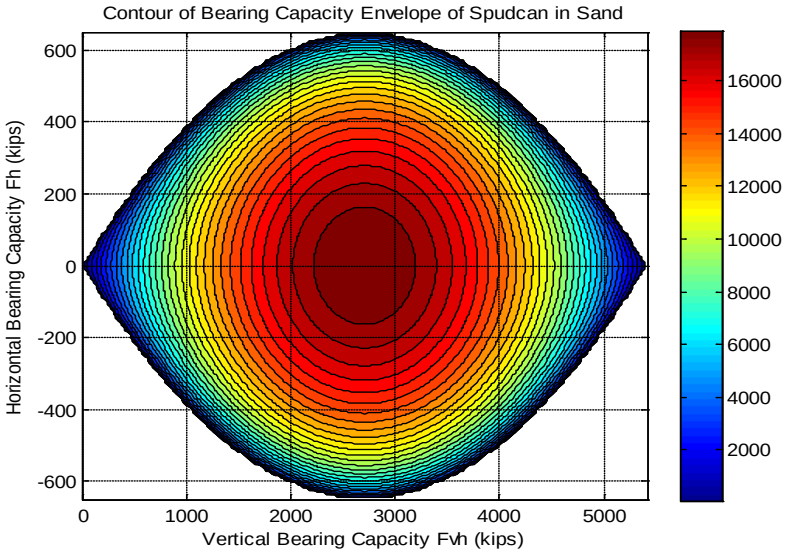

Figure 6.13 Contour of vertical-horizontal-rotational loading of spudcan in sand ($\phi = 20^o$)

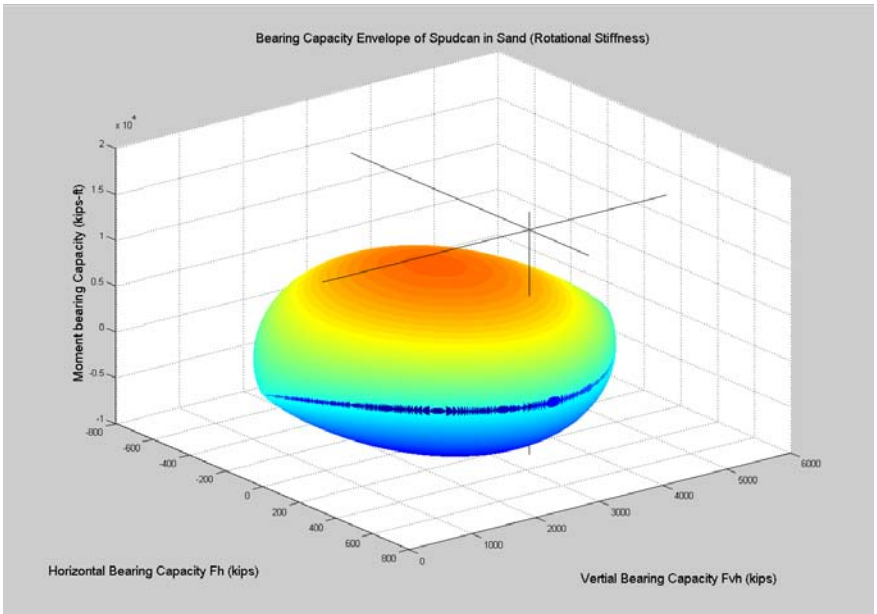

Figure 6.14 Vertical-horizontal-rotational loading interaction yield surface of spudcan in sand ($\phi = 25^o$)

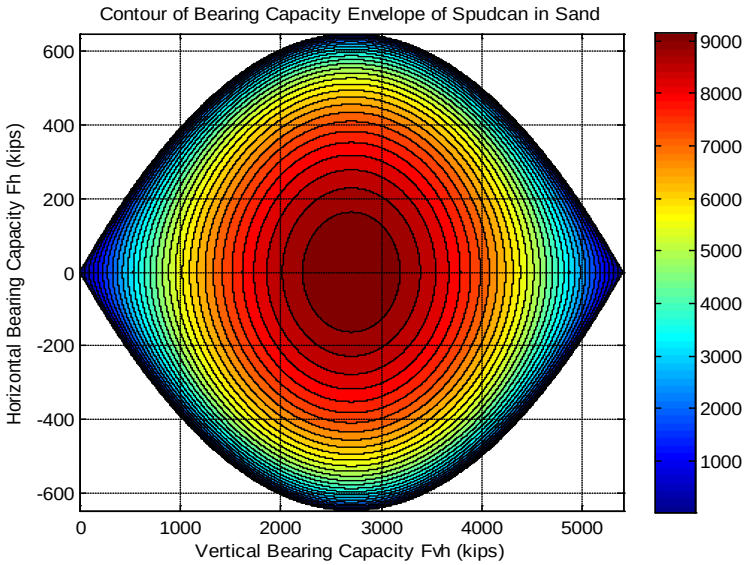

Figure 6.15 Contour of vertical-horizontal-rotational loading of spudcan in sand ($\phi = 25^o$)

6.4.2 Ultimate Vertical-Horizontal-Rotational Bearing Capacity Assessment in Clay Using SNAME Yield Function

The yield interaction function for a shallow embedded spudcan footing in clay is the same as that in sand (Equation 6.19), but H_0 and M_0 should be modified as follows:

$$H_0 = C_{u0} \cdot A + (C_{u0} + C_{u1}) \cdot A_s \tag{6.22}$$

$$M_0 = 0.1B \cdot V_0 \tag{6.23}$$

The formula of determining the maximum horizontal bearing capacity is identical with Equation 6.18, which conservatively estimates the horizontal capacity for a pinned condition. Figure 6.16 through 6.19 illustrate the yield surfaces and the contours corresponding to the lower-bound and upper-bound strength clay. Compared to Figure 6.19, the horizontal capacity of lower-bound strength clay in Figure 6.17 is relative smaller. This phenomenon coincides with the results of analysis in pinned condition footing (Figures 6.8 and 6.9). The advantage of analysis that considers soil moment resistance is that even though the environmental forces are located inside the vertical-horizontal interaction envelope in pinned condition footing model, it is not guaranteed those will be below the 3-D yield surface. In other words, the external moment loading may exceed the moment bearing capacity. The result of analysis of lower-bound strength clay is the example of this case. It should be noted that the moment bearing capacity will not change with different soil strengths while the spudcan is fully penetrated in clay. In addition, it seems clay soil can offer larger moment bearing capacity than sandy soil does for the same preloading target by comparing Equations 6.21 and 6.23.

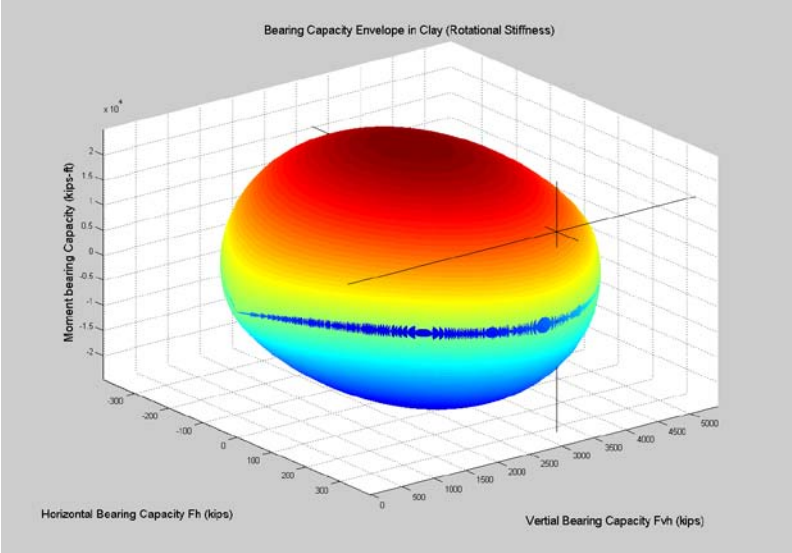

Figure 6.16 Vertical-horizontal-rotational loading interaction yield surface of spudcan in lower-bound clay (SNAME yield function)

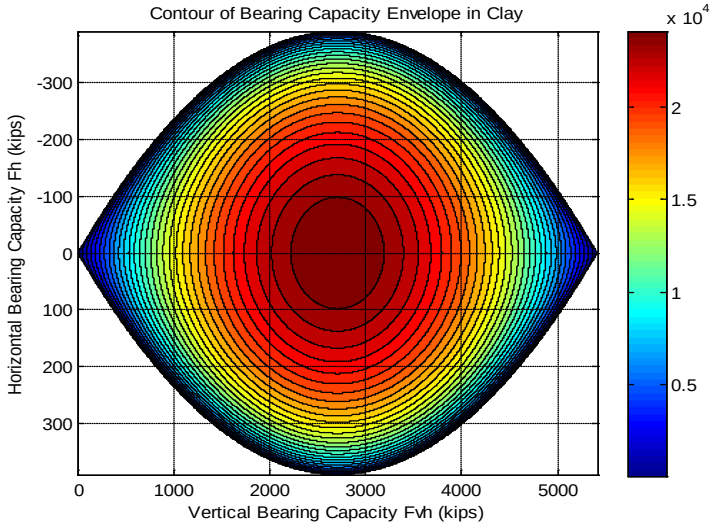

Figure 6.17 Contour of vertical-horizontal-rotational loading of spudcan in lower-bound clay (SNAME yield function)

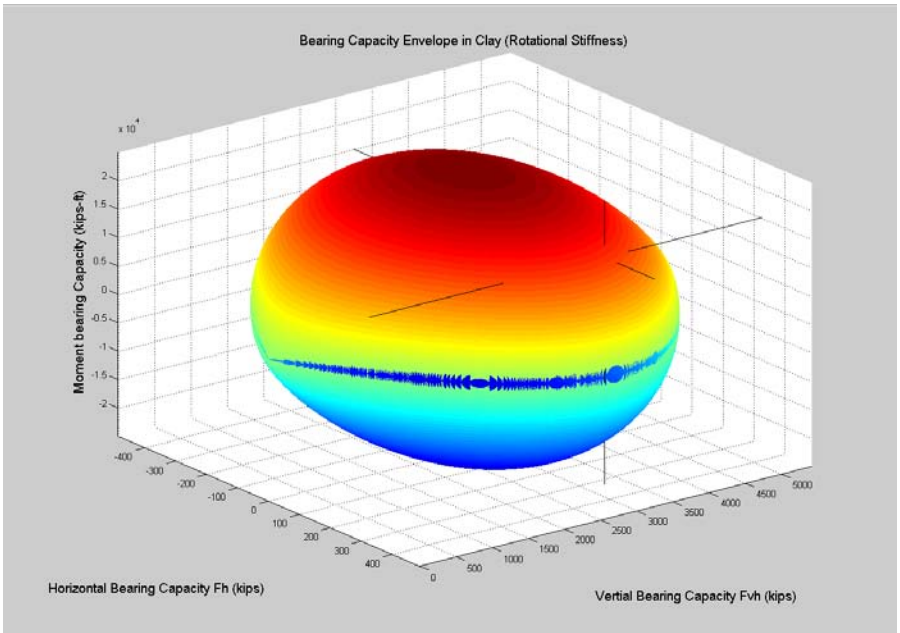

Figure 6.18 Vertical-horizontal-rotational loading interaction yield surface of spudcan in upper-bound clay (SNAME yield function)

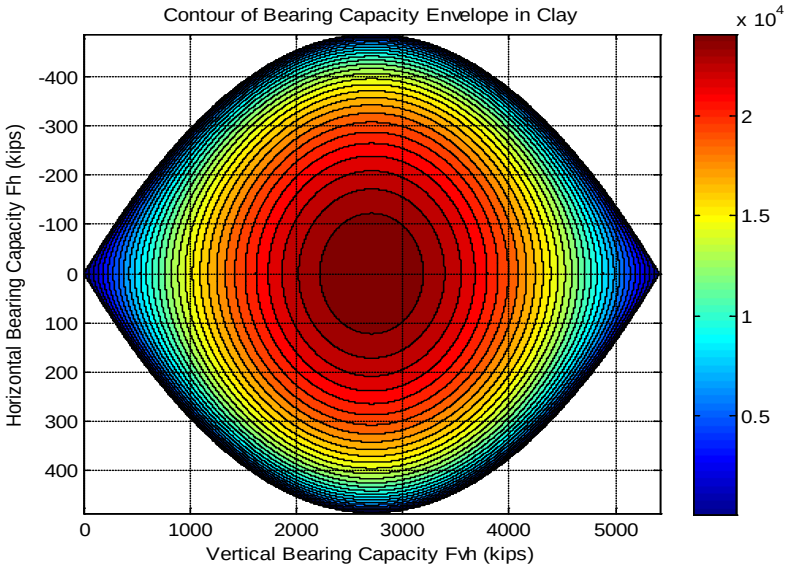

Figure 6.19 Contour of vertical-horizontal-rotational loading of spudcan in upper-bound clay (SNAME yield function)

6.4.3 Ultimate Vertical-Horizontal-Rotational Bearing Capacity Assessment in Clay Using Martin & Houlsby's Yield Function

The yield interaction function of shallowly embedded spudcan footing in clay is shown as Equation 6.24 (Martin & Houlsby, 2001):

$$f = (\frac{Q_m}{M_0})^2 + (\frac{Q_h}{H_0})^2 - 2\overline{e}(\frac{Q_m}{M_0})(\frac{Q_h}{H_0}) - \overline{\beta}^2(\frac{Q_v}{V_0})^{2\beta_1}(1-\frac{Q_v}{V_0})^{2\beta_2} \tag{6.24}$$

where V_0 is the vertical bearing capacity due to preloading and H_0, M_0, $\overline{e}$, and $\overline{\beta}$ are defined as follows:

$$H_0 = h_0 \cdot V_0 \tag{6.25}$$

$$M_0 = m_0 \cdot B \cdot V_0 \tag{6.26}$$

$$\overline{e} = e_1 + e_2 \cdot (\frac{Q_v}{V_0})(\frac{Q_v}{V_0} - 1) \tag{6.27}$$

$$\overline{\beta} = \frac{(\beta_1 + \beta_2)^{\beta_1+\beta_2}}{\beta_1^{\beta_1}\beta_2^{\beta_2}} \tag{6.28}$$

The six parameter values are $m_0 = 0.083$, $h_0 = 0.127$, $e_1 = 0.518$, $e_2 = 1.180$, $\beta_1 = 0.764$, and $\beta_2 = 0.882$. As discussed earlier, the horizontal and moment bearing capacity will not vary with different soil strengths for a fully penetrated spudcan since they are only affected by the magnitude of preloading. Figure 6.20 and Figure 6.21 show the yield surface and the contour of both upper-bound and lower-bound strength clays. The environmental forces (Figure 6.20) are located within the plastic yield surface. The axis of the yield surface is tilted in this case. From Figure 6.19, it can be observed that the maximum moment bearing capacity of SNAME yielding surface occurs at $Q_v = 0.5V_0$

and $Q_h = 0$; however, it takes place at $Q_v = 0.5V_0$ and $Q_h > 0$ (about 150 kips in this case) for the yielding surface suggested by Martin and Houlsby (Figure 6.21). This result may be beneficial, because most of spudcans may subject non-zero horizontal environmental loading. Comparing Figures 6.17, 6.19, and 6.21, the maximum horizontal bearing capacity from Martin & Houlsby's model (688 kips) is larger than those (487 kips for upper-bound and 390 kips for lower-bound) from SNAME model. Nevertheless, SNAME model can offer larger maximum moment bearing capacity (2492 kips-ft) than that estimated from Martin & Houlsby's model (2068 kips-ft).

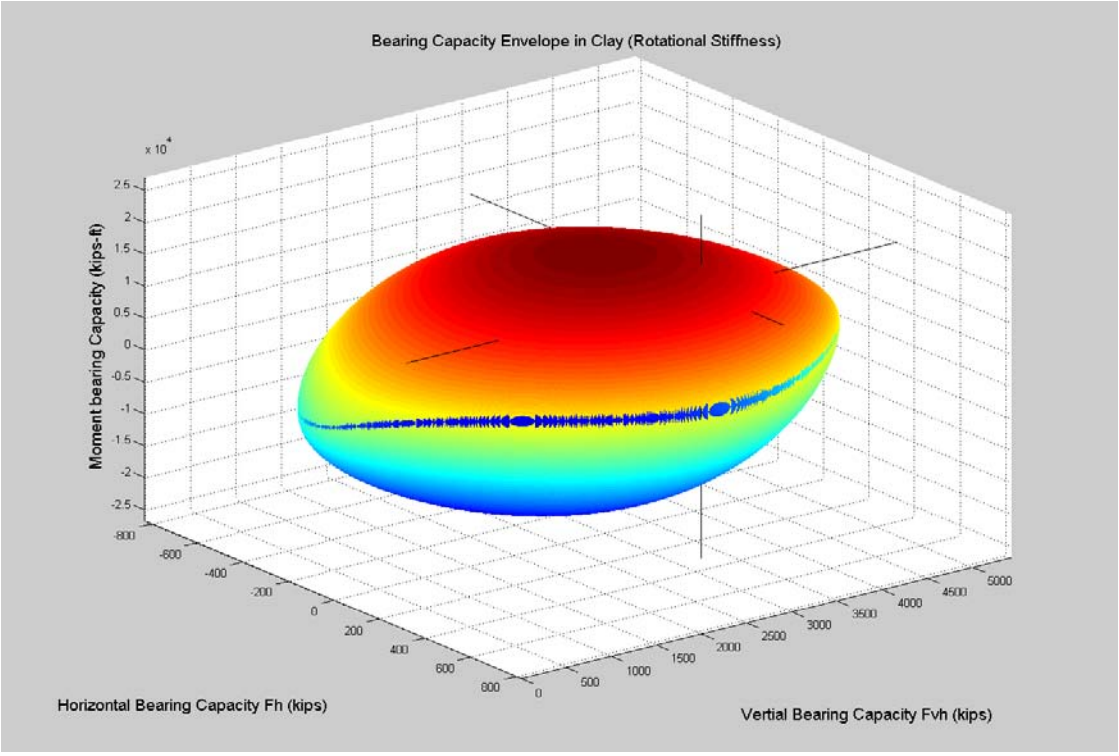

Figure 6.20 Vertical-horizontal-rotational loading interaction yield surface of spudcan in clay (Martin & Houlsby yield function)

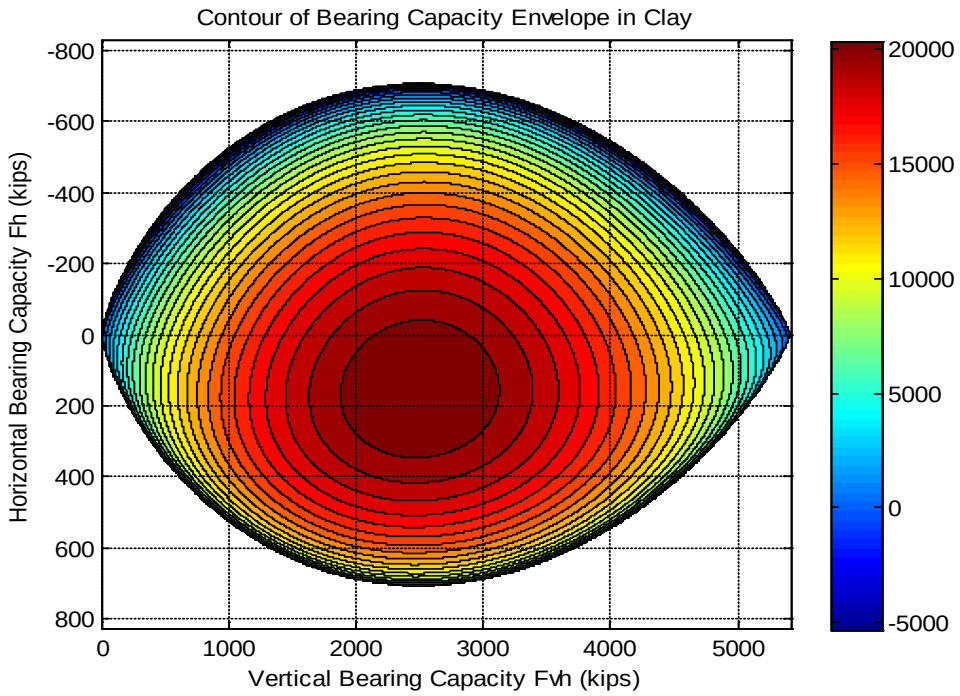

Figure 6.21 Contour of vertical-horizontal-rotational loading of spudcan in clay (Martin & Houlsby yield function)

6.4.4 Stability Assessment of Spudcans

The basic concept of stability is that the foundation is stable and safe while the environmental forces are inside the plastic yielding surface. However, how to illustrate the degree of safety of a stable spudcan footing will be the next issue of concern to engineers. In this paper, there are three steps used to evaluate the stability of a spudcan footing:

1. Illustration—checking the relation of configuration or position between the plastic yielding surface and the environmental force point.

2. Value of yield function—checking the value of yield function that environmental forces are already substituted. The smaller the value is (negative value for a stable footing), the more stable the footing will be.
3. Factor of safety—checking the factor of safety F_s of the footing. The larger the value of F_s is, the more stable the footing will be.

The first two steps may easy to understand and execute; however, the factor of safety under combined vertical-horizontal-rotational may not be simply determined by means of maximum bearing capacities divided by external forces. An overall factor of safety for the spudcan is required rather than estimating individual ones for vertical, horizontal, and moment forces. Figure 6.22 illustrates the transformation of environmental forces. The symbols α and e_c are the inclined angle and eccentricity of the resultant force F, and they could be estimated by the following equations:

$$V = F \cdot \cos\alpha = F \cdot C_1 \tag{6.29}$$

$$H = F \cdot \sin\alpha = F \cdot C_2 \tag{6.30}$$

$$M = F \cdot \cos\alpha \cdot e_c = F \cdot B \cdot \frac{e_c}{B} \cdot \cos\alpha = F \cdot B \cdot C_3 \tag{6.31}$$

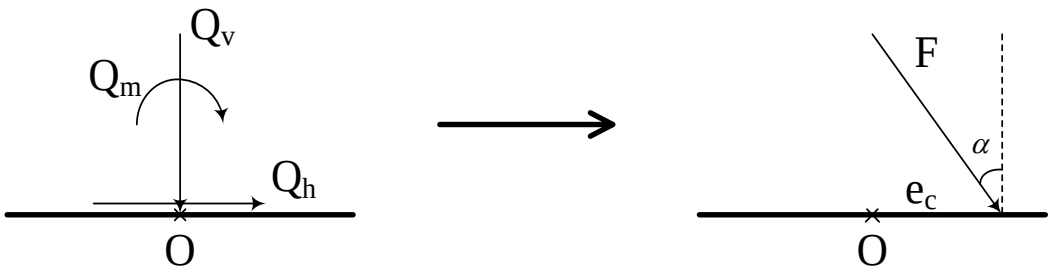

Figure 6.22 Transformation of environmental forces

The resultant force F will reach ultimate value F_{ult} when the force is exactly on the yielding surface, i.e., the value of the function is zero. Normalizing all terms by soil strength C_u and actual contact area A leads to the following expressions for dimensionless bearing capacity N_e and pure normal, tangential, and moment dimensionless capacities N_v, N_h, and N_m respectively:

$$N_e = F / C_u A \tag{6.32}$$

$$N_v = V / C_u A = N_e \cdot C_1 \tag{6.33}$$

$$N_h = H / C_u A = N_e \cdot C_2 \tag{6.34}$$

$$N_m = \frac{M}{C_u \cdot A \cdot B} = N_e \cdot C_3 \tag{6.35}$$

Now, considering the SNAME yield function (Equation 6.19) for clay, the maximum dimensionless capacities for pure normal, tangential, and moment are presented as follows:

$$N_{v0} = V_0 / C_u A \tag{6.36}$$

$$N_{h0} = H_0 / C_u A \tag{6.37}$$

$$N_{m0} = \frac{M_0}{C_u \cdot A \cdot B} \tag{6.38}$$

By virtue of Eq. 33-38, the yield function can be re-written as the following equation:

$$f = (\frac{C_3 \cdot N_e}{N_{m0}})^2 + (\frac{C_2 \cdot N_e}{N_{h0}})^2 - 16(\frac{C_1 \cdot N_e}{N_{v0}})^2 (1 - \frac{C_1 \cdot N_e}{N_{v0}}) \left| 1 - \frac{C_1 \cdot N_e}{N_{v0}} \right| \tag{6.39}$$

As mentioned earlier, the value of the function $f = 0$ when $F = F_{ult}$. Therefore, the dimensionless bearing factor N_e can be determined and the maximum resultant force F_{ult} could be estimated from Equation 6.32. The factor of safety may be defined as Equation 6.40:

$$F.S = \frac{F_{ult}}{F} \tag{6.40}$$

Table 6.3 shows the results of bearing capacity analysis for two environmental loading cases. The factor of safety is proportional to the absolute value of f and it approaches one while the value of the function is close to zero (Sand $\phi = 15^o$). In addition, it does not increase significantly from larger environmental loading to a smaller one when the point of external force is located inside of the yield surface (Sand: $\phi = 15^o$ and Clay: Upper-Bound). On the other hand, it almost becomes twice for the sand with friction angle $\phi = 25^o$ which the point is outside of the surface both in larger and smaller environmental loadings. This phenomenon means that it is difficult to obtain a high factor of safety even when the spudcan is subjected to low external forces. Comparing the results of two yield functions in clay, the SNAME model offers a more conservative solution than the other one does. As discussed earlier, the maximum moment bearing capacity of Martin & Houlsby model occurs at nonzero horizontal loading condition and this may lead to a situation that the evaluation is indicated to be not safe when using SNAME model but is stable in Martin & Houlsby model (F.S = 0.95 and 1.13 for

$Q_m = 15000$ kips-ft). It is recommended to compare the results of different yield functions when analyzing the footing in the soft clay.

Table 6.3 Results of bearing capacity analysis

$Q_v = 1250$ kips, $Q_h = 325$ kips $Q_m = 15000$ kips-ft		Position of pt.	f	F.S
Sand (SNAME)	$\phi = 15^o$	Inside	-0.0083	1.0003
	$\phi = 20^o$	Outside	0.5912	0.81
	$\phi = 25^o$	Outside	1.8536	0.51
Clay (SNAME)	Upper-Bound	Inside	-0.1137	1.04
	Lower-Bound	Outside	0.1358	0.95
Clay (Martin & Houlsby)		Inside	-0.2955	1.13
$Q_v = 1250$ kips, $Q_h = 325$ kips $Q_m = 8000$ kips-ft		Position of pt.	f	F.S
Sand (SNAME)	$\phi = 15^o$	Inside	-0.4824	1.2
	$\phi = 20^o$	Inside	-0.3121	1.12
	$\phi = 25^o$	Outside	0.0495	0.98
Clay (SNAME)	Upper-Bound	Inside	-0.3731	1.15
	Lower-Bound	Inside	-0.1236	1.04
Clay (Martin & Houlsby)		Inside	-0.5968	1.31

6.5 Displacement Assessment

The elastic displacement of unloading or reloading due to applied environmental forces can be calculated by dividing the increment of loading by the elastic stiffness. According to Kausel & Ushijima (1979), the vertical, horizontal, and rocking static stiffness of

embedded circular foundations on elastic stratum of finite depth are presented as follows:

$$K_v = \frac{4GR}{1-\nu}(1+1.28\frac{R}{H})\cdot(1+0.5\frac{E}{R})\cdot[1+(0.85-0.28\frac{E}{R})\cdot\frac{E/H}{1-E/H}] \quad (6.41)$$

$$K_h = \frac{8GR}{2-\nu}(1+0.5\frac{R}{H})\cdot(1+\frac{2}{3}\frac{E}{R})\cdot(1+\frac{5}{4}\frac{E}{H}) \quad (6.42)$$

$$K_r = \frac{8GR^3}{3(1-\nu)}(1+\frac{1}{6}\frac{R}{H})\cdot(1+2\frac{E}{R})\cdot(1+0.7\frac{E}{H}) \quad (6.43)$$

Where ν is Poisson's ratio, R is foundation radius, H is layer thickness, and E is embedment depth. If the spudcan is in an elastic half-space, with bedrock at a great depth, a layer thickness $H \to \infty$ can be assumed. The assessment of shear modulus G is an issue because it is the primary parameter which affects the stiffness. According to Wroth et al. (1979) and Andersen (1992), the shear modulus for clay may be taken as $I_r = \frac{G}{C_u}$. Typical I_r values for small strain may range from 200 to 400 for over-consolidation ratio less than 4 and 800 to 100 for N.C clay. In sandy soil, the empirical formulae suggested by Dean et al. (1992) are shown as follows:

$$G_v = 36,600 + 24.9\cdot(\frac{V_0}{A}) \quad (6.44)$$

$$G_h = 1,100 + 5.6\cdot(\frac{V_0}{A}) \quad (6.45)$$

$$G_r = 4,100 + 11.5\cdot(\frac{V_0}{A}) \quad (6.46)$$

The units of the equations are in kPa (kN/m^2). Table 6.4 presents the results of displacement assessment. In the analysis of footing in clay, the effect of shear modulus degradation is considered (Figure 6.23, 0.5% strain assumed). The vertical displacement of unloading can be simply calculated by the following equation:

$$\delta_v = \frac{\Delta Q_v}{K_v} \tag{6.47}$$

Table 6.4 Results of displacement assessment

$Q_v = 1250$ kips, $Q_h = 325$ kips $Q_m = 15000$ kips-ft		F.S	Unloading Displacement (ft)	Reloading Displacement (ft)	
				Elastic	Plastic
Sand (SNAME)	$\phi = 15^o$	1.0003	-0.03	0.01	0
	$\phi = 20^o$	0.81	-0.04	0.04	0.32
	$\phi = 25^o$	0.51	-0.05	0.05	0.63
Clay (SNAME)	Upper-Bound	1.04	-0.33	0.12	0
	Lower-Bound	0.95	-0.39	0.39	1.29

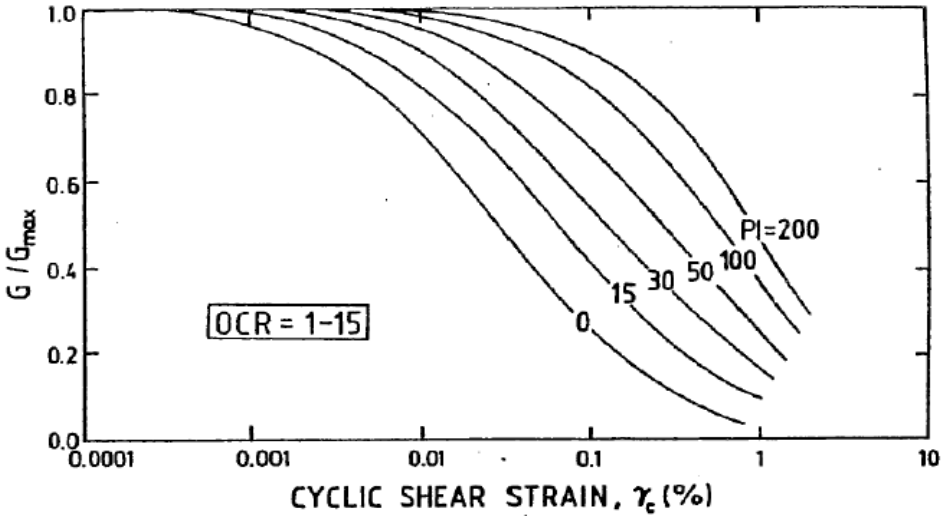

Figure 6.23 Shear modulus degradation in clay

In the analysis, the Poisson ratio ν is 0.3 for sand and plastic index PI = 20 and I_r = 600 for clay.

The vertical displacement will exceed the elastic range for reloading when the spudcan is subjected to larger environmental forces (F.S < 1). Based on the plasticity theory, it is not acceptable that the external force is outside of the yielding surface since the spudcan is unstable in this situation. Not until the point of external force locates exactly on it does the yielding surface stop growing; therefore, additional settlement of spudcan can be expected. Figure 6.24 through 6.27 show the new positions and yielding surfaces of spudcan in $\phi = 25^o$ sand and lower-bound strength clay. It can be observed that the new yielding surface of sand (Figure 6.25) is much larger than that of under preloading (Figure 6.14). The additional settlement (plastic displacement) is 0.63 ft for sand and 1.29 ft for clay respectively. However, this situation is not allowable and it may lead to the failure of the jack-up.

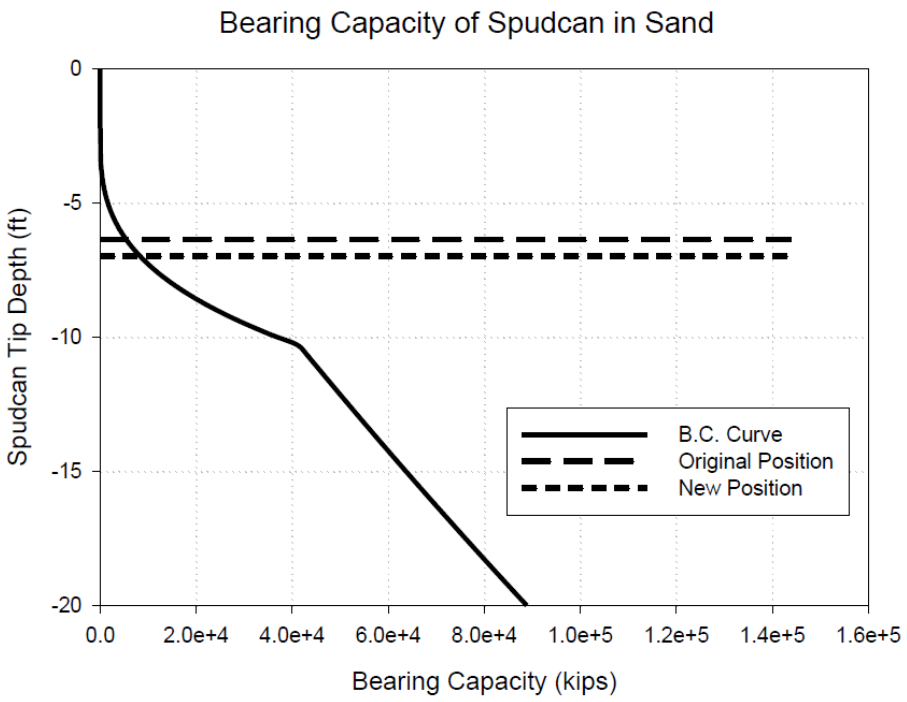

Figure 6.24 Additional settlements due to large environmental force in sand ($\phi = 25^o$)

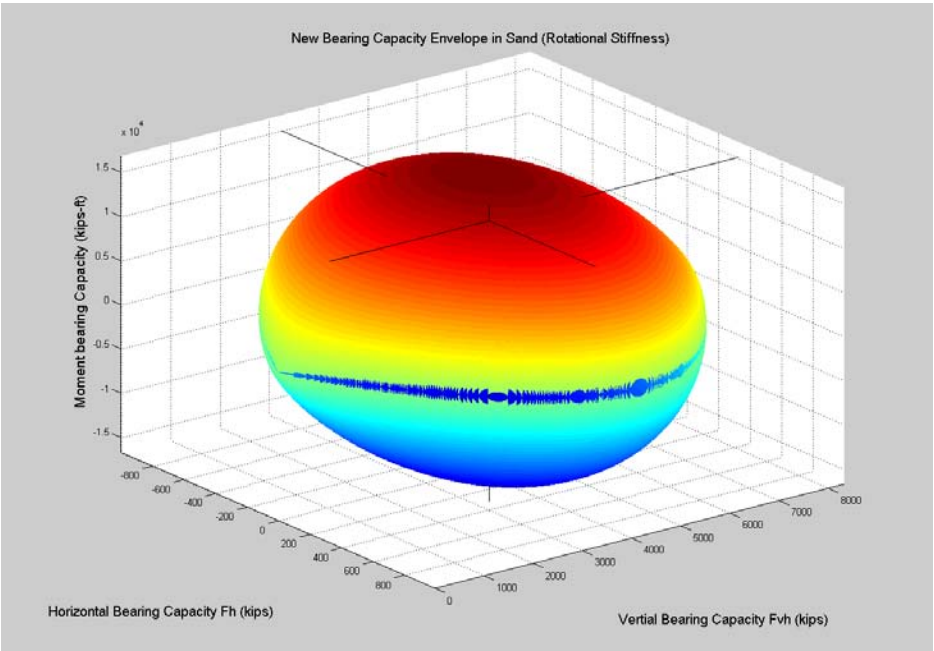

Figure 6.25 New yield surface due to large environmental force in sand ($\phi = 25^o$)

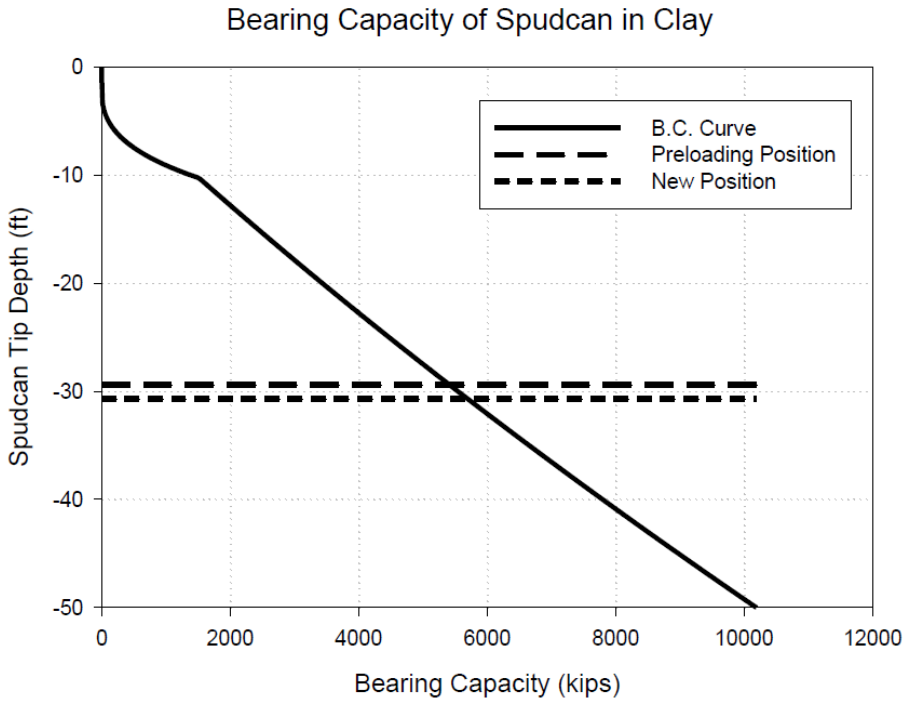

Figure 6.26 Additional settlements due to large environmental force in clay

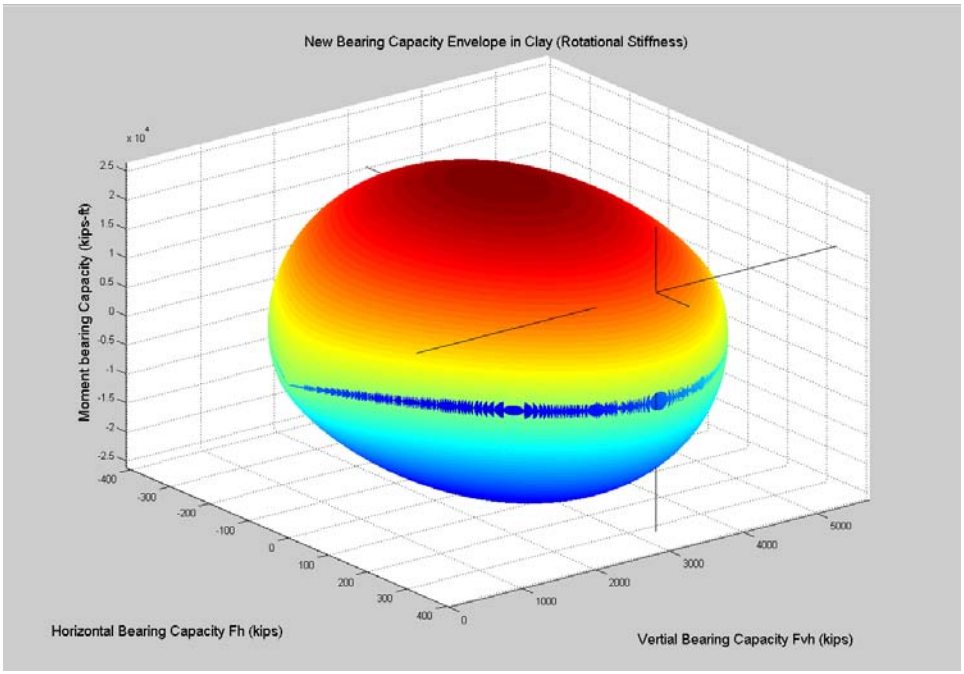

Figure 6.27 New yield surface due to large environmental force in clay

CHAPTER VII

SUMMARY AND CONCLUSIONS

7.1 Summary

This research utilized plasticity theory to investigate commonly used anchors and foundations for offshore structures, including drag embedment anchors and spudcan foundations. The main purpose of investigations of DEAs is to obtain an understanding of trajectory and holding capacity, and develop reliable simulation models to predict their behavior in the seabed, under in-plane and out-of-plane motions. Due to their cost-effectiveness and high holding capacity comparing with self weight, DEAs are widely used for the temporary anchorage of offshore platforms, but not usually permitted for permanent anchorage in deep waters because of the uncertainty in predicting load capacity, uncertainly that is largely due to the uncertainty in the trajectory. The DEA simulation analysis can provide realistic predictions of DEA trajectory and capacity for a variety of soil profile, anchor line and anchor characteristics.

For the analysis of spudcan foundation, the assessments of stability and settlement are the targets of the research. In the stability assessment, a three-stages assessing procedure is recommended: illustration of the configuration of yielding surface and environmental forces, the value of yielding function with external forces substituted, and the factor of safety of the spudcan. In addition, the results of the assessment may be ambiguous while the different yield functions are employed to analyze the spudcan in soft clay. It should be paid attention that the additional settlement (plastic displacement)

of the footing may occur if the jack-up unit is applied on titanic environmental forces and a punctilious design should avoid this situation.

7.2 Conclusions

(A) Drag Embeddment Anchors under In-Plane Loadings:

1. During drag embedment the anchor rapidly reaches an equilibrium state in which the rate of anchor rotation equals the rate of change of the anchor line angle at the shackle, $\dot{\theta}_s = \dot{\theta}_a$ (Figure 4.16). As the equilibrium state is approached, the normalized load capacity of the anchor at the shackle $\hat{T}_a = N_e A_f / b^2$ approaches a constant value (Figure 4.15).
2. The equilibrium condition approaches a condition of pure translation parallel to the anchor fluke ($\psi = 0$). The actual rate of rotation of the anchor in the equilibrium state is positive, but numerically small. Consequently, the governing anchor bearing factor at equilibrium – and therefore throughout most of the anchor trajectory - corresponds to a condition of pure translation parallel to the fluke, $(N_e)_{eq} = N_e$ ($\psi = 0$).
3. A higher bearing factor N_e (and consequently $\hat{T}_a$) leads to a reduced rate of anchor rotation (Equation 4.44) and, hence, greater penetration during drag embedment. From the standpoint of anchor geometry, optimizing the anchor design is a matter of maximizing capacity while maintaining a collapse mechanism consistent with drag embedment. Greater fluke-shank angles θ_{fs} and smaller shank length L_s/L_f tend to increase capacity N_e as well as embedment depth (Figure 4.17). However, the range over which these geometric variables can be varied is constrained by the requirement

to maintain a drag embedment mode of penetration; i.e., translation primarily parallel to the fluke (e.g., Figures 4.6-4.10).

4. Interaction effects for combined loading on a plate are extremely important from the standpoint of both load capacity (Figure 4.4) and kinematics (Figure 4.5). Therefore, careful evaluation of interaction parameters is required for reliable prediction of $(N_e)_{eq}$.

(B) Drag Embedment Anchors under Out-of-Plane Loadings:

1. This study presents an analysis of an anchor which, after an initial installation stage occurring in the vertical plane of intended loading, is subjected to an out-of-plane load. Except at very shallow depths, the soil shearing resistance is large relative to the weight of the anchor chain, in which case the chain will lie in a plane, even under conditions of out-of-plane loading. The orientation of the chain at the pad-eye and mudline determine the orientation of the oblique plane. With appropriate rotation of the coordinate system, it is possible to formulate tension-angle and trajectory prediction equations that are very similar to those previously developed for anchor chains contained within a vertical plane.
2. Using the modified equations, a calculation sequence has been developed for predicting drag anchor performance for the following scenario: (1) initial anchor installation within the intended vertical plane of loading to an arbitrary installation depth, (2) the occurrence of out-of-plane loading applied at the mudline due to partial failure of the mooring system accompanied by the re-configuration of the

anchor chain, and (3) continued loading with resumption of the embedment process within an oblique plane.

3. For the example analysis considered, continued embedment occurred after imposition of out-of-plane loading; however, the additional embedment beyond the initial installation depth was relatively modest. While the analyses did not indicate a loss of the original installation load capacity due to a mooring system failure - at least for the scenario considered by the parametric study - they did predict a substantial reduction in the ultimate, or reserve, load capacity of the anchor.

(C) Stability Assessment of Spudcan Foundation:

1. The settlement due to preloading in clay is much more significant than that in sand; a spudcan in a high undrained shear strength clay may penetrate twice amount of it on low friction angle sand (Figure 6.2 and 6.3). In soft clay, the penetration depths may be too large to be tolerated and they have been recorded as much as 55 meters in Mississippi delta (Mirza et al., 1989).
2. In a pinned condition footing analysis, the lower friction angle sand offers larger horizontal bearing capacity than higher friction angle sand does under the same preloading condition (Figure 6.5 and 6.6) due to the reduced penetration depth in the dense sand. Both F_h^* and penetration depth D, from Equation 6.12, are inverse proportional to the friction angle ϕ. On the other hand, the horizontal bearing capacity in clay at lower vertical force level is controlled by the Equation 6.18, which estimates sliding capacity conservatively. Since the lateral projected area A_s does not change under conditions of full penetration, the values of undrained shear

strength C_{u0} and C_{u1} are higher for stronger clay (Figure 6.8 and 6.9). The average maximum normalized sliding capacity of spudcan in sand is 0.14 and around 0.08 in clay and both of them are more conservative than the results done by Vesic (0.15) and DNV (0.13).

3. The size of the yield surface in sand recommended by SNAME does not vary with the soil strength unless the spudcan is partially penetrated which the maximum sliding capacity keeps a constant value but the maximum moment bearing capacity reduces with friction angle increasing (Figure 6.10-6.15). In clay, it changes with undrained shear strength both in partially and fully penetrated cases. The horizontal bearing capacity increases with soil strength but the moment capacity does not change for fully a penetrated spudcan (Figure 6.16-6.19).
4. In contrast to the yield function suggested by SNAME in clay, the sliding and moment capacity estimated from Martin and Houlsby's model do not change with soil strength for a full penetrated spudcan. In addition, it seems the SNAME model offers a more conservative assessment than the Martin & Houlsby analysis (Table 6.3). Different results from the stability evaluations may occur when the clay undrained shear strength is low. More laboratory or centrifuge tests may be helpful to resolve this issue.
5. The elastic displacement of spudcan can be determined using Equation 6.47; however, an estimate of the shear modulus is critical to a realistic displacement assessment. Due to the design criteria, the situation of additional settlements (plastic displacement) of spudcan occurs is not allowable because it means the point of

environmental force is located outside of yielding surface. A larger preloading target or wider footing diameter may help to avoid this problem.

REFERENCES

Andersen K.H. (1992). "Cyclic effect on bearing capacity and stiffness for a jack-up platform on clay." Norwegian Geotechnical Institute, Oslo report 913012-1, Rev 1.

Andersen, K. H., Murff, J. D., and Randolph, M. R. (2003). "Deepwater anchor design practice-vertically loaded drag anchors." Phase II Report to API/Deepstar, Norwegian Geotechnical Institute, Norway, Offshore Technology Research Center, USA and Centre for Offshore Foundation Systems, Australia.

Andersen, K. H., Murff, J. D., Randolph, M. R., Clukey, E. C., Erbrich, C.T, Jostad, H. P., Hansen, B., Aubeny, C., Sharma, P., Supachawarote, C. (2005). "Suction anchor for deepwater applications." *Proc. Int. Symp. On Frontiers in Offshore Geotechnics*, IS-FOG05, Balkema, Perth, Australia.

American Petroleum Institute (API) (1989). *Recommended practice for planning, designing, and constructing fixed offshore platform*, API Recommended Practice 2A (RP2A) 18 Ed., Washington, D.C.

Aubeny, C. P., and Chi, C. (2010a). "Mechanics of drag embedment anchor in a soft seabed." *Journal of Geotechnical and Geoenvironmental Engineering*, Vol. 136, No. 1, 57-68

Aubeny, C. P., and Chi, C. (2010b), "Trajectory prediction for drag embedment anchors under out of plane loading." *Proc. Int. Symp. On Frontiers in Offshore Geotechnics*, Balkema, Perth, Australia.

Aubeny, C. P., Murff, J. D., and Kim, B. M. (2008), "Prediction of anchor Trajectory during drag embedment in soft clay." *Int. J. Offshore Polar Eng*., 18(4), 314-319

Bowles, J.E., (1996). *Foundation Analysis and Design, 5th ed*., McGraw-Hill, New York.

Bransby, M. F. and O'Neill, M. P. (1999), "Drag anchor fluke-soil interaction in clay." International Symposium on Numerical Models in Geomechanics (NUMOG VII), Graz, Austria, 489-494.

Dahlberg, R. (1998) "Design procedures for deepwater anchors in clay." *Proc. 30th Offshore Technology Conference*, OTC 8837: Houston.

Dean, E. T., James, R. G., and Schofield, A. N. (1992), "A new procedure for assessing fixity of spudcans on sand." Andrew N Schofield and Associates Ltd., Cambridge, MA.

Dove, P., Treu, H., and Wilde, B. (1998), "Suction embedded plate anchor (SEPLA): a new anchoring solution for ultra-deep water mooring." *Proc. DOT Conf.*, New Orleans, Louisiana.

Elsabee, F., and Morray, J. P. (1977), "Dynamic behavior of embedded foundations." Research Rep. No. R77-33, Dept. of Civil Engineering, MIT, Cambridge, MA.

Gaudin, C., O'Loughlin, C.D., Randolph, M.F., and Lowmass, A.C. (2006). “Influence of the installation process on the performance of suction embedded plate anchors.” *Geotechnique*, 56(6): 381-391.

Kausel E and Ushijima R. (1979). "Vertical and torsional stiffness of cylindrical footing." Research report R79-6, MIT, Cambridge, MA.

Kim, B. M. (2005), “Upper Bound Analysis for Drag Anchors in Soft Clay.” Ph. D. Dissertation, Texas A&M University, College Station, Texas.

Lelievre B. and Tabatabaee J. (1979). “Holding capacity of marine anchors with planar fluke in sand.” *Proc. 1st Canadian Conf on Marine Geotech Engineering*, Calgary, 301-310.

Lelievre B. and Tabatabaee J. (1981). “The performance of marine anchors with planar fluke in sand.” *Canadian Geotech Journal*, Vol. 18, 520-534.

LeTourneau Inc. “LeTourneau super 116 class platform.” Brochure of LeTourneau Inc.

Martin C.M. and Houlsby G.T. (2000). "Combined loading of spudcan foundations on clay: Laboratory test." *Geotechnique*, 50(4), 325-338.

Martin C.M. and Houlsby G.T. (2001). "Combined loading of spudcan foundations on clay: Numerical modeling." *Geotechnique*, 51(8), 687-698.

Martin, C.M., and Randolph, M.F. (2001). “Applications of the lower and upper bound theoremsof plasticity to collapse of circular foundations”. *Proc. 10th Int. Conf. Int. Association of Computer Methods and Advances in Geomechnics*, Tucson, Vol. 2, Balkema, Rotterdam, 1417-1428.

Meriam, J.L. (1975) *Statics*, 2nd Ed., John Wiley and Sons, New York.

Mirza U.A., Sweeney M., and Dean A.R. (1989). "Potential effect of jack-up spudcan penetration on jacket piles." *Proc. of Offshore Technology Conf*. OTC 5762, Houston

Murff, J. D. (2006). “Plastic limit analysis in geotechnical engineering class notes.” Department of Civil Engineering, Texas A&M University, College Station, Texas.

Murff, J. D., Randolph M. F., Elkhatib, S., Kolk, H. J., Ruinen, R. M., Strom, P. J., and Thorne, C. P. (2005). "Vertically loaded plate anchors for deepwater applications." *Proc. Int. Symp. on Frontiers in Offshore Geotechnics*, IS-FOG05, Balkema, Perth, Australia, 31-48.

NCEL (1987), *Drag embedment anchors for navy moorings*, Naval Civil Engineering Laboratory, Port Hueneme, California, Tech data Sheet 83-08R.

Neubecker, S. R., and Randolph, M. F. (1995). "Profile and frictional capacity of embedded anchor chain." *Journal of Geotechnical Engineering Division*, ASCE, 121, 11, 787-803.

Neubecker, S.R. and Randolph, M.F. (1996). "The performance of embedded anchor chains systems and consequences for anchor design." *Proc. 28th Offshore Technology Conference*, OTC 7712, Houston.

O'Neill, M.P., Bransby, M.F. and Randolph, M.F. (2003). "Drag anchor fluke-soil interaction in clays." *Canadian Geotechnical Journal*, 40, 78-94.

O'Neill, M.P., Randolph, M.F., and House, A. R. (1999). "The behavior of drag anchors in layered soils." *International of Offshore and Polar Engineering*, Vol. 9, No. 1, March 1999.

Randolph, M.F., and Houlsby, G.T. (1984). "The limiting pressure on a circular pile loaded laterally in cohesive soil." *Geotechnique*, 34(4), 613-623.

Rowe, R.K., and Davis, E.H. (1982) "The behaviour of anchor plates in clay," *Geotechnique*, 32, 1, 9-23.

Ruinen R., and Degenkamp G. (1999). “Advances in the development and operational experience with Stevmanta VLAs in deep water environments.” *4th IBC Conf. Mooring & Anchors*, Aberdeen, Scotland.

Ruinen, R. (2000). “The use of drag embedment anchors and vertical loaded anchors (VLAs) for deepwater moorings.” *Continuous Advances in Mooring & Anchorings*, Aberdeen, 1-19.

Schlumberger website. http://www.glossary.oilfield.slb.com/ Display.cfm? Term= semisubmersible

Seadrill website. http://www.seadrill.com/modules/module_6011/drilling_unit_list. asp? typeId=7&mid=162

Society of Naval Architects and Marine Engineers, (2002) "Technical & Research Bulletin 5-5A. Guidelines for Site Specific Assessment of Mobile Jack-up Units." Society of Naval Architects and Marine Engineers (SNAME).

Stewart, W.P. (1992) "Drag embedment anchor performance prediction in soft soils." *Proc. 24th Offshore Technology Conference*, OTC 6970, Houston, Texas.

Stewart, W.P. (2007) "Mat-supported jack-up foundation on soft clay—overturning storm stability." Eleventh International Conference, London.

Tention Technology International website. http://www.tensiontech.com/services /mooring.html

Thorne, C. P. (1998). “Penetration and load capacity of marine drag anchors in soft clay.” *Journal of Geotechnical and Geoenvironmental Engineering*, ASCE, 124(10), 945-953.

Van Langen H. and Hopspers B., (1993), "Theoretical model for determining rotational behavior of spudcan." Offshore Technology Conference OTC 7302, Houston, Texas.

Vesic A.S., (1975), "Bearing capacity of shallow foundation." Foundation Engineering Handbook, Van Nostrand.

Vivatrat, V. Valent, P.J. and Ponterio, A.A. (1982) "The influence of chain friction on anchor pile design," *Proceedings of the 14th annual Offshore Technology Conference*, OTC 4178, Houston, Texas.

Vryhof Anchors (2005) Vryhof Anchor Manual, Krimpen ad Yssel, Netherlands.

Vryhof Anchors (2010) Vryhof Anchor Manual, Krimpen ad Yssel, Netherlands.

Wroth, C.P., Randolph, M.F., Houlsby, G.T., and Fahey, M. (1979), "A review of the engineering properties of soils with particular reference to the shear modulus." Cambridge University Department. Report No 1523/84/SM049/84.

Yang, M., Murff, J.D. and Aubeny, C.P. (2010) "Undrained capacity of plate anchors under general loading," accepted for publication *Journal of Geotechnical and Geoenvironmental Engineering*, ASCE.

Yang, M., Murff, J.D., and Aubeny, C.P. (2008). “Out of plane loading of plate anchors, analytical modeling, Phase II Report.” Offshore Technology Research Center (OTRC), Texas A&M University, College Station, Texas.

VITA

Chao-Ming Chi received his Bachelor of Science degree in civil engineering from Feng Chia University, Taiwan in 1999. During his four year Bachelor career, he obtained The Best Grade in school for the course “General Physics”, The Best Grade in department of Civil Engineering for the course “Structural Theory”, and The Best Grade in class. He received his Master of Science degree in civil engineering from National Cheng Kung University in Taiwan 2001. During serving for the Taiwan Army, he passed the qualify exam to be a professional geotechnical engineer in 2002. Chao-Ming pursued his Doctor of Philosophy degree in Texas A&M University and served as Research Assistant under the supervision of Dr. Charles Aubeny. He obtained the Department Head Fellowship in 2009 and graduated with his Ph.D. in August 2010.

Chao-Ming Chi may be reached at 3136 TAMU, College Station, TX 77840-3136. His e-mail is edisonji0625@yahoo.com.tw